Stony Brook University

In situ Ambient Pressure Studies of Dynamic Surface Transformations on Cu-based Model

Catalysts

A Dissertation Presented

by

Fang Xu

to

The Graduate School

in Partial Fulfillment of the

Requirements

for the Degree of

Doctor of Philosophy

in

Chemistry

Stony Brook University

May 2016

Stony Brook University

The Graduate School

Fang Xu

We, the dissertation committee for the above candidate for the

Doctor of Philosophy degree, hereby recommend

acceptance of this dissertation.

Michael G. White – Dissertation Advisor
Professor, Department of Chemistry

David M. Hanson – Chairperson of Defense
Research Distinguished Service Professor, Department of Chemistry

Dario J. Stacchiola – Third Member
Scientist, Department of Chemistry, Brookhaven National Laboratory

J. Anibal Boscoboinik – Outside Member
Associate Materials Scientist, Center for Functional Nanomaterials, Brookhaven National
Laboratory

This dissertation is accepted by the Graduate School

Charles Taber
Dean of the Graduate School

Abstract of the Dissertation

In situ Ambient Pressure Studies of Dynamic Surface Transformations on Cu-based Model

Catalysts

by

Fang Xu

Doctor of Philosophy

in

Chemistry

Stony Brook University

2016

Copper-based heterogeneous catalysts are widely used in many industrial applications across the fields of fuels and energy. In order to probe the catalyst structure under reaction conditions, state-of-the-art ambient pressure techniques have been implemented. This dissertation is focused on room temperature in situ ambient pressure (AP) (10 mTorr to 2 Torr) studies on Cu-based model catalysts including Cu(111), Cu_2O/Cu(111), potassium modified Cu_2O/Cu(111) and CeO_2/Cu_2O/Cu(111). It investigates their surface dynamic transformations using scanning tunneling microscopy (STM), infrared reflection adsorption spectroscopy (IRRAS), and X-ray photoelectron spectroscopy (XPS).
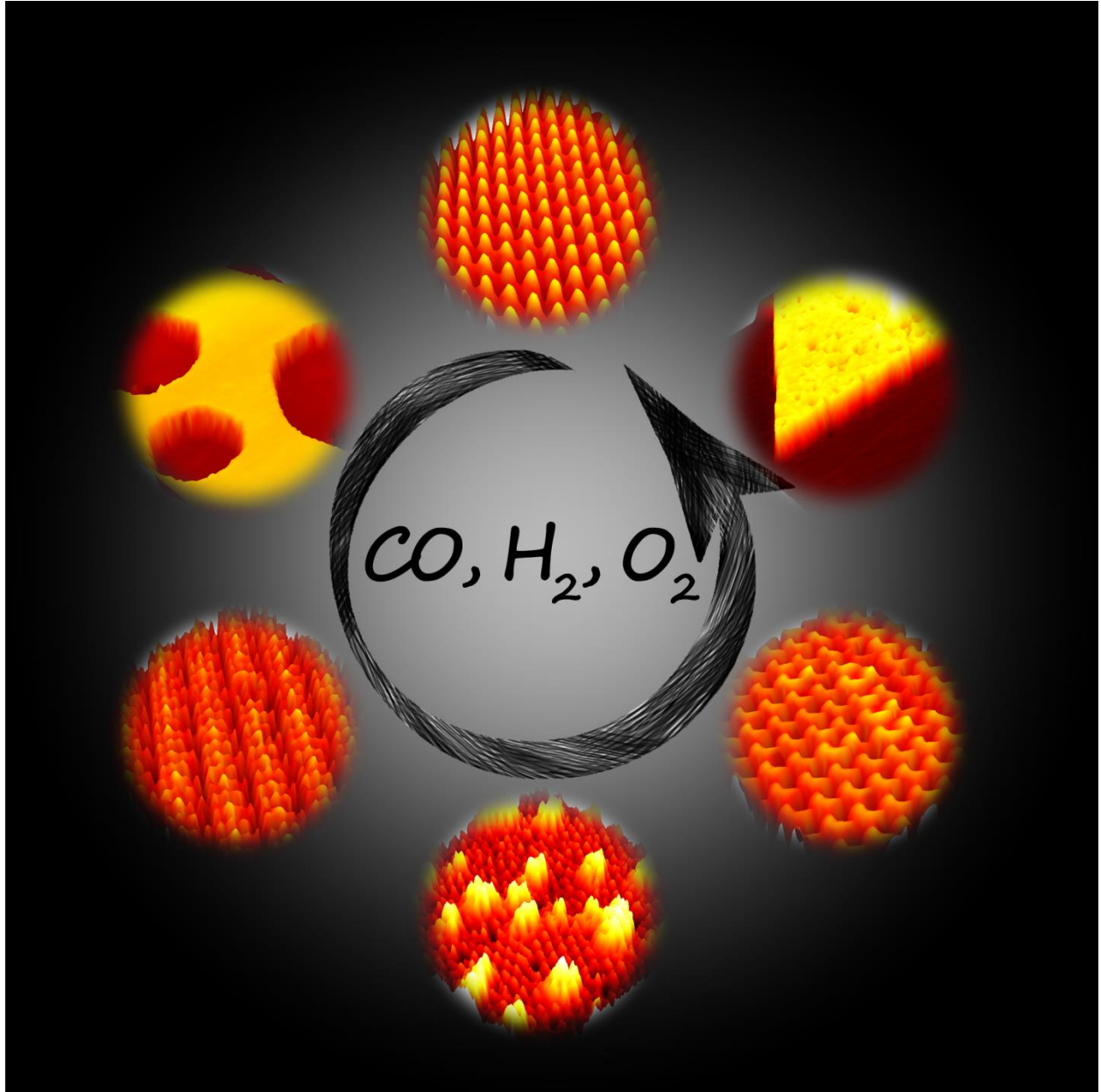
Under ambient pressures, Cu(111) surface is roughened by CO, or O_2. Atomic H can heal nano-pits formed on the surface of Cu(111). Both CO and H_2 reduce Cu_2O/Cu(111), but the reduction occurs ~100 times slower in the latter case. As reduction proceeds, phases of

$Cu_2O/Cu(111)$, the intermediate Cu_2O-hex/5-7 structure, and Cu segregate, and the Cu metallic front forms by mass transfer. When reduced by CO, the potassium modified $Cu_2O/Cu(111)$ catalyst system has a rate orders of magnitude higher than the unmodified surface, due to the formation of active sites at the location of the potassium species. However, this modification does not promote the reduction by H_2.

Low coverages of CeO_2 supported on $Cu_2O/Cu(111)$ were prepared, and it is shown that Ce^{4+} is reduced to Ce^{3+} prior to Cu_2O reduction by 1.5 Torr H_2. The hydrogenation of ceria results in an expanded Ce-O-Cu interface, which facilitates methanol synthesis from CO_2.

CO oxidation by O_2 occurs on Cu(111) at 300 K. The top layer of Cu(111) is oxidized to Cu^+ and Cu^{2+} under a mixture of 30 mTorr CO and 15 mTorr O_2. Even under a similar total pressure with an 8:1 $CO:O_2$ ratio, copper oxidation cannot be avoided. Reactants are consumed through redox cycles, and the surface eventually reaches a dynamic equilibrium. The activity trend of the Cu species at the surface for producing CO_2 is $Cu > Cu^+ \gg Cu^{2+}$.

Frontispiece

Table of Contents

List of Figures/Tables

xiii

collected in a sequence of time within 20 min. The bottom spectrum was taken after 20 min of reaction. The total pressure change as a function of the reaction time is shown in the insert. B) $CO:O_2 = 99$ mTorr:1 mTorr. Two peaks increase in intensity as a function of time after exposure to $CO + O_2$. Spectra in B) were obtained after subtracting the CO gas phase adsorption peak. 104

List of Abbreviations

AES   Auger Electron Spectroscopy

AP   Ambient Pressure

CHA   Concentric Hemispherical Analyzer

DFT   Density Functional Theory

DOS   Density of States

ESCA   Electron Spectroscopy for Chemical Analysis

ETEM   Environmental Transmission Electron Microscope

fcc   Face-centered cubic

FTIR   Fourier-transform Infrared Spectroscopy

hcp   Hexagonal close packed

IR   Infrared

IRRAS   Infrared Reflection Absorption Spectroscopy

LEED   Low Energy Electron Diffraction

PROX   Preferential Oxidation

STM   Scanning Tunneling Microscopy

XAS   X-ray absorption spectroscopy

XPS   X-ray Photoelectron Spectroscopy

UHV   Ultra-high Vacuum

WGSR   Water gas Shift Reaction

Acknowledgments

I feel lucky and grateful to be a Ph.D. candidate at Stony Brook University and conduct my research full time at Brookhaven National Laboratory, where I was exposed to state of the art instruments, and top level scientists around the world. In the past four and a half years, I've learnt more than the previous sixteen years at school, not only in scientific knowledge, but also different cultures and personalities. Here, I would like to express my thankfulness to funding agencies, my colleagues and my families.

I would like to thank my research advisor, Prof. Michael White. Prof. White is a good mentor, who recognized the shining points in a student's potential and spared no effort to encourage him/her for further development. Whenever I needed him, he was there. Sometimes, I really felt like him as a father, especially in my case that I was a newcomer and did not know much about American culture. I had the feeling when I was invited to the annual Christmas party in his house. I had the feeling when I was confused on career choices and he thought on my side and gave practical suggestions. Thank you, Mike!

I would also thank other lab members and visiting scholars who helped me, supported me, collaborated with me or just showed their friendliness to me: Dr. Jose Rodrigues, Dr.Wei An, Dr. Robert M. Palomino, Dr. Wenqian Xu, Dr. Fan Yang, Dr. Thuy Duong Nguyen Phan, Dr. Xiaofang Yang, Dr. Huanru Huang, Prof. Jing Zhou, Prof. Zhijun Zuo, Dr. Yixiong Yang, Dr. Shyam Kattel, Dr. Nicholas Camillone, Dr. Miki Nakayama, Dr. John Lofaro, Dr. Dan Wilson, Dr. Sung-Young Hong, Matthew Kershis, Joe Magee, Danielle C O'Connor, Si Luo, Pan Xu, Zongyuan Liu, Shizhong Liu, Lizhou Nie, Meng Xue, Pamela Carrillo, Amanda Muraca, Filip Dvořák and Erik Peterson.

I would like to thank Prof. David Hanson and Dr. J. Anibal Boscoboinik who were willing to be in my defense committee.

Finally, and most importantly, I would like to thank my husband Fan, my twin sister, my parents, my roommate Anna and her two cats. There were times when experiment didn't work; there were times when I walked out of chemistry building exhaustedly at 4 am with only my car in the parking lot; there were times when my paper got accepted; there were times when I got the chance to present my work in conferences; there were times when I was awarded. I shared my happiness and stress with them, who showed their support and helped me back to a positive attitude. Without them, I may be a totally different person.

Thank you all!

Chapter 1 Introduction

1.1 General Introduction of Heterogeneous Catalysts

Heterogeneous catalysts are used for modifying the reaction rate and selectivity of chemical reactions without being consumed during the process. The word heterogeneous refers to difference in phases that catalysts and reactants belong to. The most common case is solid phase catalysts and gas phase reactants. The term catalysis was put forward by Berzelius in 1836.[1] Heterogeneous catalysts were firstly used in ethanol oxidation to make vinegar, fat hydrolysis to make soap, and ethanol dehydration to make diethyl ether. In 1895, Ostwald was awarded the Nobel Prize for his work in fundamental catalysis.

Nowadays, heterogeneous catalysis is widely used for commercial purposes, including two of the most successful and largest industrial scale processes: methanol formation (overall conversion over 99%[2]) and ammonia synthesis (overall conversion of 98%[3]). World production of ammonia in 2014 was about 145 million ton,[4] and global methanol production was about 60 thousand metric tons in 2012.[5] Heterogeneous catalysts are also used to refine petroleum, control emission from gasoline engines, reform organic compounds, and convey biological tasks by combining with enzymes.

Development of successful heterogeneous catalysts is a time and money consuming process. Generally speaking, a successful industrial catalyst needs to pass three stages of primary

screening, secondary screening and scaling up, which include steps of proposing, synthesizing, screening, characterization, testing mechanism/ kinetics/ stability, catalyst scaling up, pilot testing, reactor and process designing, and plant testing.[6] If the fundamental mechanisms are understood, effectively designing successful catalysts can be achieved.

1.2 Model Catalysts

Heterogeneous catalysts used in the industry are very complex powder materials. For example, powder alumina is coated on honeycomb walls as a substrate on three way catalysts. Nanoparticles of Pt, Rh, ceria, zirconia, and lanthana, and occasionally baria are coated on top of alumina as functional components.[7] The industrial catalyst for methanol synthesis is Cu/ZnO supported on Al_2O_3 or Cr_2O_3 with Cu and ZnO presented as nanoparticles.[8,9] The complexity adds difficulty in understanding the mechanisms of the catalytic reactions,[8] and there are debates over the prevalence of various reaction pathways and active sites. In order to gain more understandings of the fundamental catalytic reaction mechanisms at the atomic and molecular level, well-defined model catalysts, which are simplified yet still able to mimic properties of the powder catalysts, are introduced.[10-12] The substrate of model catalysts are artificially-cut single crystals only containing one exposed crystallographic face indicated by miller indices, such as Cu(111), Pt(111), and TiO_2(110). The surface can be modified with nanoparticles or pits to increase complexity. Surface sensitive techniques are then applied which probe the top layers of model catalysts where most heterogeneous reactions occur. Because of the well-defined structures, the surfaces can often be represented by theoretical models, which give more insight about the reactive sites, intermediates, reaction pathways, etc. Thus, studies on model systems are of great significance in terms of advancing our fundamental understanding of catalysts.

1.3 Catalysts of Metal and Supporting Oxides

Typical (conventional) heterogeneous catalysts are composed of dispersed metals at nanometer scale on metal oxide supports. Metals have long been used as active phases in heterogeneous catalysis, because of various functions such as facilitating dissociation,[13] formation of important steps,[14] improving selectivity.[15] Metal oxides, on the other hand, may also have a crucial effect on the activity and selectivity,[16] because of the oxygen storage ability, presence of defects (oxygen vacancies, crystalline boundaries), and their relatively high stability. The interface between the metal and the metal oxide support may also lead to unique active sites.[17]

There are two types of metal oxide substrates: the substrate that functions as a supportive template and contributes little in chemistry,[18,19] and the substrate that works synergically with the on-top metals. For instance, for the three way converter in automotive emission control, alumina is the support which stabilizes the on-top Pt, Rh nanoparticles, but is not involved in the reaction pathways.[7] On the other hand, for Cu/CeO_2, which is used for the water gas shift reaction (WGSR), the substrate CeO_2 not only disperses Cu particles, but also promotes the activity.[20] When two and more on-top metals work with each other, each of them may be responsible for a different reaction step, and the collaborations make the catalyst work. For instance, platinum and silica supported alumina catalyst is used for conversion of n-heptane to isoheptane. Platinum is active for hydrogenation, and silica-alumina is active for isomerization.[21] The overall bifunctional catalyst successfully takes advantages of both processes.

1.4 Inverse Catalysts

Bulk metal oxides are usually insulators or semi-conductors.[22] The poor electron conduction leads to surface charging problems during many surface sensitive measurements such as X-ray Photoelectron Spectroscopy (XPS) and scanning tunneling microscopy (STM). However, when metal oxides are deposited on top of metal substrates, the nanoparticles exhibit unique physical and chemical properties, such as a high density of defects at edges, corners and oxygen vacancies, enhanced stability[23] and mobility[24] of modified lattice structure from bulk, and shifted energy gaps,[25] from the bulk. The system of metal oxide nanoparticles on the conductive metal substrates removes the charging problem, and is ideal for studies of the surface metal oxide. The catalysts composed of metal oxide on top of metal substrates, i.e., the opposite of conventional catalysts, are called inverse catalysts (Figure 1.1A).

Additionally, the unique physical and electronic properties of inverse catalysts may have an advantage in activity.[26,27] An example is presented in Figure 1.1B. Cu(111) is the benchmark for water gas shift reaction (WGSR, equation 1.1).

$$CO + H_2O \rightarrow CO_2 + H_2 \tag{1.1}$$

The Cu(100) surface has a higher reaction rate than Cu(111) because it has more low coordination sites. The conventional catalyst nanoparticle based $Cu/CeO_2(111)$ has a higher activity than the previous two, because of the more defected sites and maybe the synergy effect. The inverse catalyst $CeO_{2-x}/Cu(111)$ has the highest activity of all the model catalysts in this combination of materials as a result of configuration of the catalyst and the appearance of an large amount of Ce^{3+} during the reaction, which is not the case for $Cu/CeO_2(111)$.
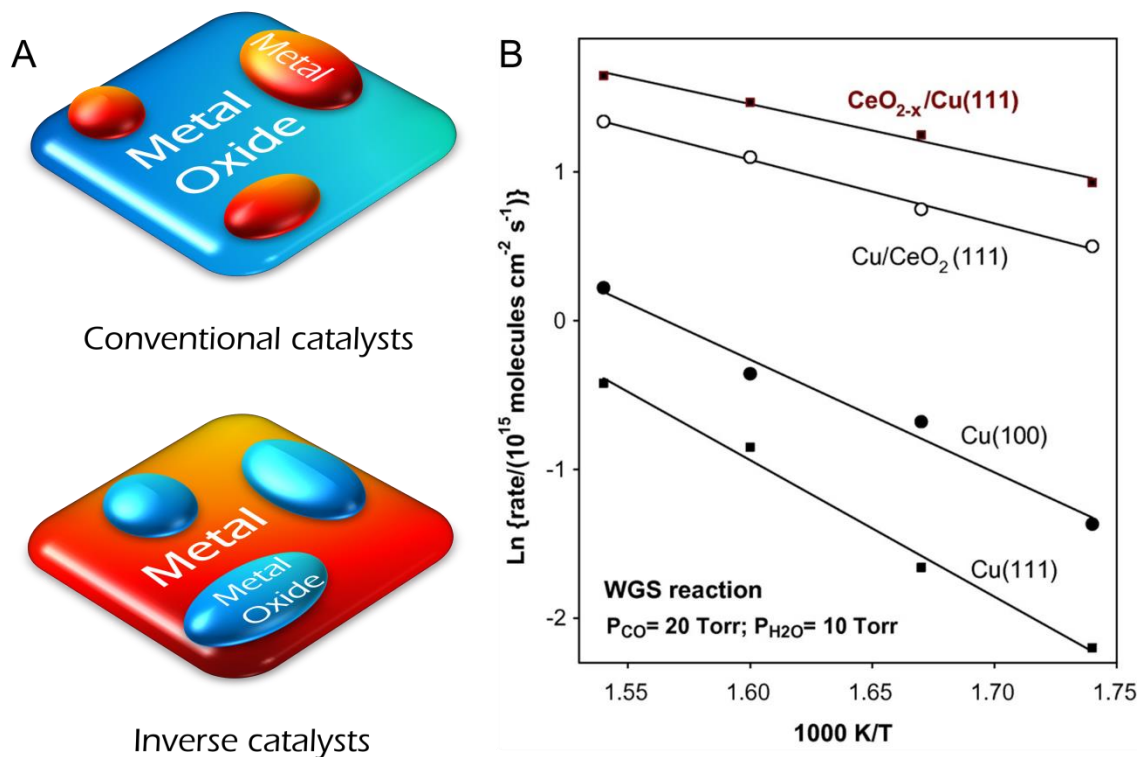
Figure 1.1 A) Conventional catalyst and inverse catalysts B) Water gas shift reaction rate on conventional and inverse catalysts. Graph is from Ref.[26]

1.5 High Pressure Induced Topographical Changes on Model Catalysts

It is widely known that a pressure gap exists between model heterogeneous catalysts systems ($< 10^{-5}$ Torr) and industrially applied powder heterogeneous catalysts systems (> 760 Torr). Under the latter conditions, the surfaces of catalysts are highly dynamic, and also, the active phase may not be the same as the one before or after reaction.[28] Thus, efforts have been made to develop in situ techniques, such as ambient pressure (AP)- X-ray photoelectron spectroscopy (XPS),[29] AP-X-ray absorption spectroscopy (XAS),[30] AP- infrared reflection absorption spectroscopy (IRRAS),[31] AP-STM,[32] and environmental transmission electron microscope (ETEM),[33] which can be used to probe the atomic structure, electronic structure and

surface intermediates under reaction. Based on these techniques, many new features under elevated pressures are revealed.
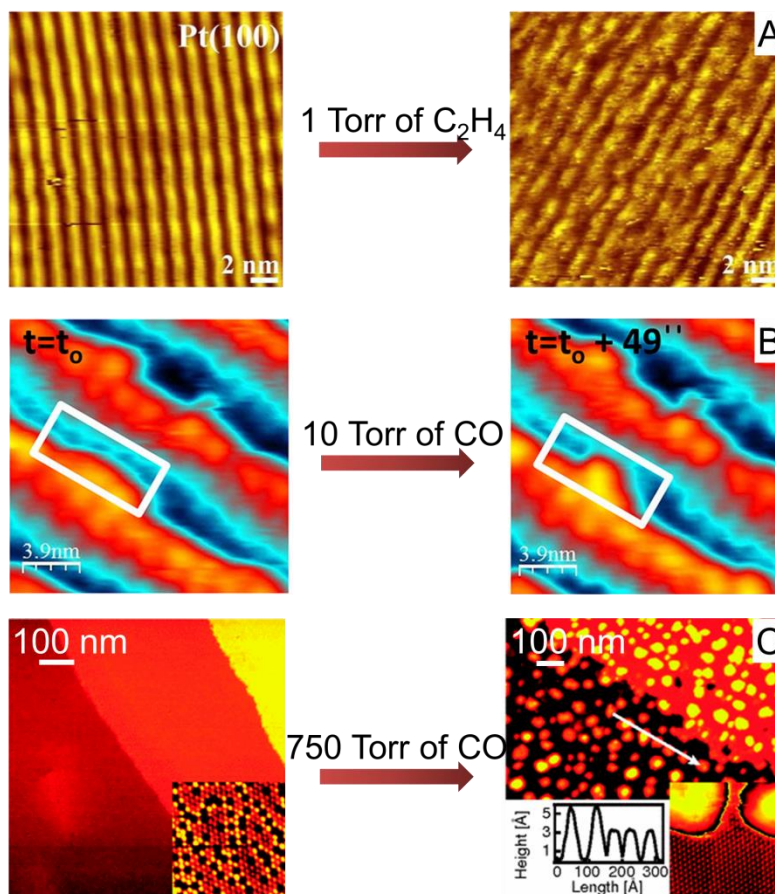
Figure 1.2 *Examples of surface reconstruction under ambient pressure gasses. A) Adapted from Ref,[34] with permission from American Chemical Society. B) Adapted from Ref,[35] with permission from American Chemical Society. C) Adapted from Ref,[36] with permission from the American Physical Society.*

In terms of powder catalysts, reaction conditions above atmospheric pressure, and temperatures close to 1000 K are not uncommon. Under these conditions, phase segregation of alloys,[37] elongation/ contraction of nanoparticles,[38] surface planes redistributions,[39] reversible particle movements[40] are reported. Reaching these conditions with model catalysts is difficult, especially when it comes to atomically resolved topographical studies. Most experimental conditions reported in the literature are performed at pressures under a few Torr and below 400

K. Compared to the conventional ultra-high vacuum (UHV) conditions, the in situ experiments are denoted as high pressure, which can be also named elevated pressure, ambient pressure, or near ambient pressure. Similar to powder catalysts, the presence of reactants under ambient pressure conditions induces structural and morphological changes of model catalysts. For example in Figure 1.5, Pt(100) reconstructs under 1 Torr C_2H_4 at 298 K;[34] mobility of Pt(111) step edges increases under 10 Torr CO at 300 K;[35] phase segregates when Au/Ni(111) is exposed to 750 Torr CO at 300 K.[41] This dissertation is focused on study model catalysts under in situ ambient pressure conditions at 300 K, in order to unravel unique properties, such as adsorbate and reaction induced changes in surface structure and composition.

1.6 Copper-based Model Catalysts

Cu-based heterogeneous catalysts are widely used in many crucial industrial and lab-based reactions of CO conversions and hydrogenations, such as low temperature stage water-gas shift reaction (equation 1.1),[10,42,43] preferential oxidation (PROX, equation 1.2 with CO less than 1.5% in the feed gas),[44-46] alcohol formation (equation 1.3, 1.4),[9] and the prototypical CO oxidation (equation 1.2).[47,48] These reactions are shown below:

$$2CO + O_2 \rightarrow 2CO_2 \tag{1.2}$$

$$xCO + 2xH_2 \rightarrow C_xH_{2x+1}OH + (x-1)H_2O \tag{1.3}$$

$$CO_2 + 3H_2 \rightarrow CH_3OH + H_2O \tag{1.4}$$
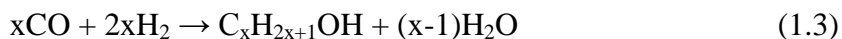
Cu-based powder catalysts have a variety of facets and oxidation states,[49] and their complexity has proven to be a challenge for atomic scale studies. Thus, as it is discussed in section 1.1, copper-based model catalysts are used to simplify local environment and to mimic

powder catalysts to a certain extend. The most common Cu single crystals are Cu(110) and Cu(111). The Cu(111) surface will be discussed in section 1.6.1 in detail, since it is used in this dissertation.

1.6.1 Cu(111)

Bulk copper adopts face-centered cubic (fcc) structure. In a fcc structure, an element occupies every vertex and face center in the cubic shaped unit cell. The Cu single crystal can be cut into many planes. The structure of Cu(111) is shown in figure 1.2. Of all of the planes among copper, Cu(111) is the most thermostable, which means Cu(111) is the most common plane in copper powders. Thus, in this dissertation, my model catalysts are based on Cu(111).
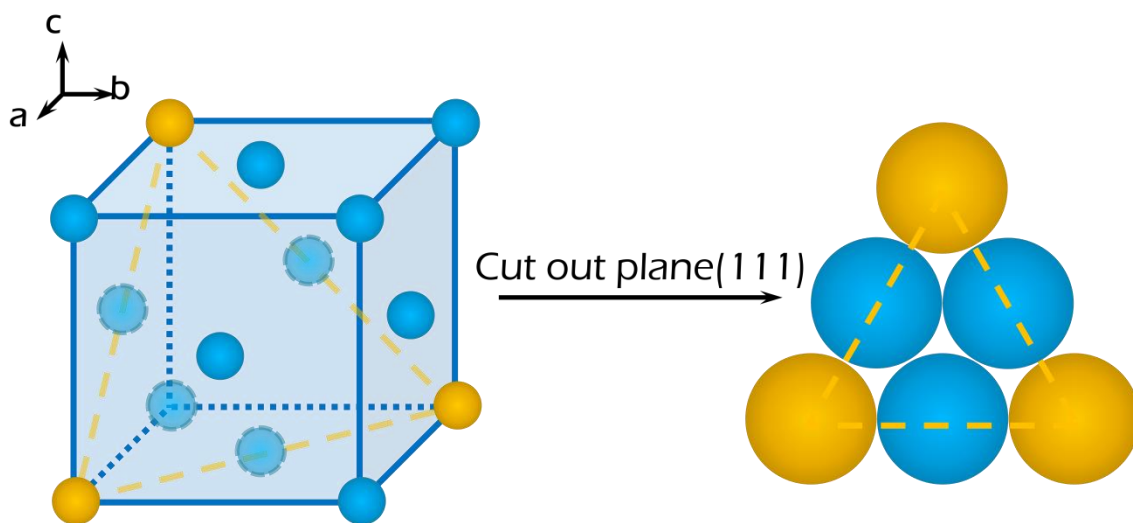
Figure 1.3 *Fcc structure and plane (111).*

1.6.2 Cu$_2$O/Cu(111) – '44', '29' and hex/5-7

Under atmospheric pressure of oxygen, copper can be easily oxidized. The Cu$_2$O is the most stable phase under UHV conditions.[50] A stable Cu$_2$O-like monolayer on the Cu(111) surface can be obtained by exposing Cu(111) to elevated temperature in an oxygen background.

Unlike bulk $Cu_2O(111)$ which is composed of perfect hexagonal ring structures, the $Cu_2O/Cu(111)$ monolayer thin films have distorted ring structures which present long range row structures. Two types of $Cu_2O/Cu(111)$ surfaces, Cu_2O-'44' and Cu_2O-'29', have been atomically defined since 1991.[51,52] As shown in Figure 1.3, the notation '44' and '29' refer to the super unit cell of the row structure which is 44 and 29 times larger than the primitive Cu(111) unit cell. According to spectroscopic data, both structures have a total oxygen coverage of 0.52 ML,[51] which leads to the conclusion that only some of the ring centers are covered by chemisorbed oxygens. To the best of my knowledge, no density functional theory (DFT) model has been able to perfectly represent the $Cu_2O/Cu(111)$ surface. The best models are a $Cu_2O(111)$ like monolayer on Cu(111).[53] The Cu_2O – '44' structure forms by annealing O/Cu(111) at 473 - 623 K,[52] or annealing Cu(111) under 5×10^{-7} Torr O_2 at 650 K.[54] Further annealing of the Cu_2O – '44' structure at 673 K leads to a structural change to Cu_2O – '29'.[52]
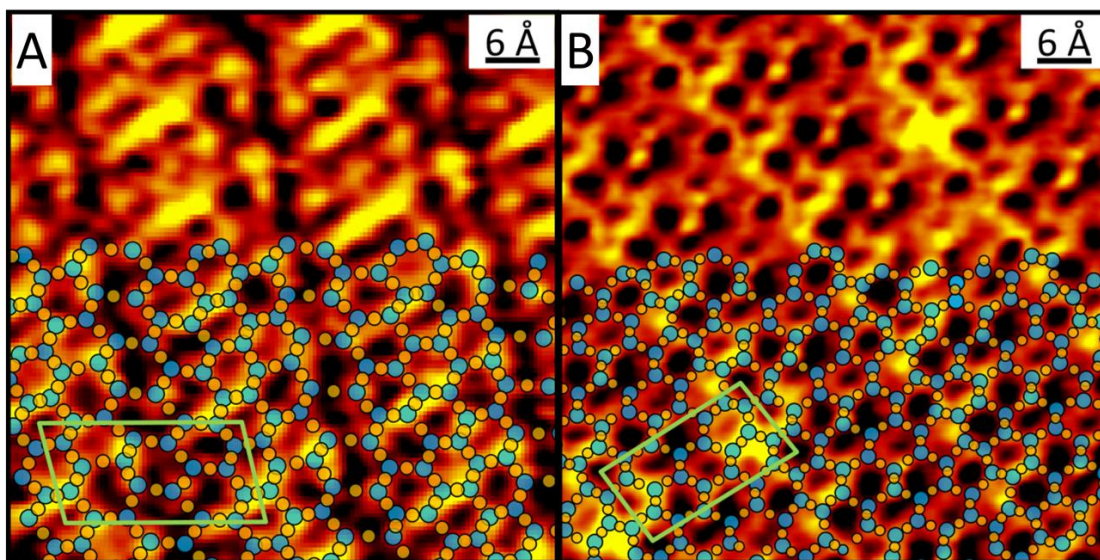
Figure 1.4 *STM images of atomically resolved $Cu_2O/Cu(111)$ at 300 K. (A) $Cu_2O/Cu(111)$ -'44' structure: 0.45 nA, 1.24 V. Unit cell of $(11.2 \pm 0.1Å) \times (21.9 \pm 0.1$ Å), 76.4 °is highlighted; (B) $Cu_2O/Cu(111)$ -'29' structure: 0.49 nA; 1.10 V. Unit cell of $(9.2 \pm 0.1Å) \times (18.0 \pm 0.1$ Å), 84.9 ° is highlighted. Blue ball: lattice O; Yellow ball: Cu. Chemisorbed oxygen atoms in the ring center are not drawn. Adapted from Ref.[55] Copyright belongs to WILEY-VCH Verlag GmbH & Co. KGaA, Weinheim.*

9

The Cu$_2$O/Cu(111) surface can be reduced by gases such as CO, H$_2$, and NO. During the reduction process, a mixture of hexagonal rings and five membered by seven membered ring structures, or Cu$_2$O-hex/5-7 are detected, Figure 1.4 A. The inserts of Figure 1.4A show that the seven membered rings can be imaged as depressions or protrusions under different scanning conditions. According to DFT modeling, the Cu$_2$O-'5-7' structure is formed by rotating a shared O-Cu-O bond between two neighboring six membered Cu$_2$O rings, Figure 1.4B-C.
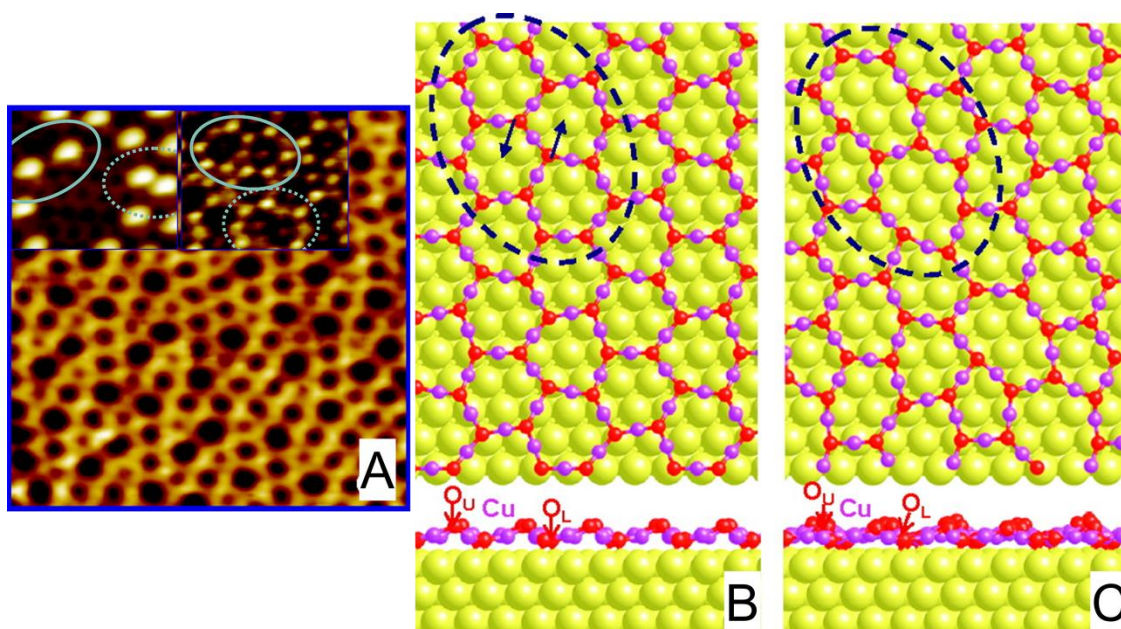
Figure 1.5 *(A): An STM image of a surface covered by Cu$_2$O six membered rings and Cu$_2$O–'5-7' rings (Cu$_2$O-hex/5-7). Two inserts show that ring center of the seven membered rings can be imaged as protrusions or depressions. (B) – (C): DFT models showing the formation of Cu$_2$O – '5-7' from hexagonal Cu$_2$O(111)-like film. Images are adapted from Ref,* [54,56] *with permission from American Chemical Society.*

1.7 Summary

Powder heterogeneous catalysts have been developed to meet large scale catalytic goals. However, understanding the catalytic mechanisms of powder heterogeneous catalysts is a challenging task due to the complexity of the powder surfaces and harsh reaction conditions.

Thus, model catalysts based on single crystals are used to mimic powder catalytic surfaces. With the help of state-of-the-art ambient pressure techniques, surface dynamic transformations of the model catalysts under ambient pressures are studied to unravel reaction mechanisms.

This dissertation is focused on copper-based model catalysts under ambient pressure conditions of CO, O_2, H_2, and mixtures of CO/O_2. The model catalysts include Cu(111) (chapter 3 and chapter 6), Cu_2O/Cu(111) (chapter 4), potassium and/or ceria modified Cu_2O/Cu(111) (chapter 5). Systematic studies are presented on surface structural changes due to high pressure gasses, chemical identifications, and reaction mechanisms.

Chapter 2. Experimental Methods

2.1 Ultra-high Vacuum Systems

Ultra-high vacuum (UHV) refers to pressures below 10^{-9} Torr. The commonly maintained pressure inside a UHV chamber is in the range of 10^{-10} to 10^{-11} Torr, close to the pressure in outer space within the solar system, which is estimated to be 10^{-13} to 10^{-14} Torr.[57] UHV pressure can usually be maintained by using ion pumps or molecular turbo pumps with back-up pumping. However, each pump has its own working pressure range, which should not be exceeded during operation. A few examples are listed in Figure 2.1.

The collision rate of a non-dissociative gas (F) hitting a surface can be calculated by Hertz-Knudsen equation (equation 2.1):

$$F = \frac{p}{\sqrt{2\pi m k_b T}} \tag{2.1}$$

Here, p is gas pressure, m is the mass of the gas, k_b is the Boltzmann constant, T is the temperature. At 300 K, the collision rate of 1×10^{-6} Torr He is 1.4×10^{15} atom/(cm^2·s). A monolayer (ML) is determined by having one adsorbate on each surface atom. Assuming the density of atoms on the surface of a substrate is 10^{15} atom/cm^2, and each collision leads to an adsorption of He. With 1s of exposure under 10^{-6} Torr He, 1 ML of adsorbate is achieved. In surface science, the unit Langmuir (L), which is named after American physicist Irving Langmuir, corresponds to a gas exposure as $1L = 10^{-6}$ Torr·s. Thus, ultra-high vacuum is needed

for two reasons: 1) maintaining a clean surface within a decent amount of time for experiment, and 2) allowing electrons and photons have large enough free-paths for characteristic techniques, such as XPS, auger electron spectroscopy (AES) and low energy electron diffraction (LEED).
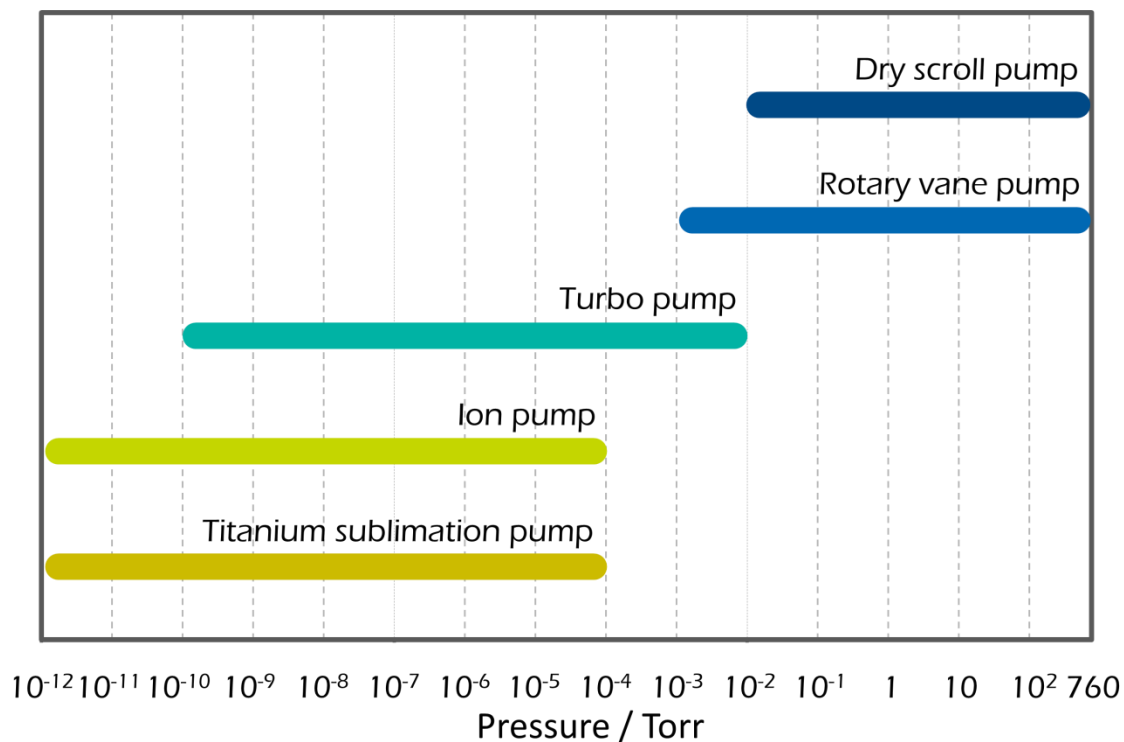
Figure 2.1 *Typical working pressures for vacuum pumps.*

The coverage of an adsorbate is highly depended on the pressure and temperature. As pressure increases and temperature decreases, more adsorbates adsorb on the surface, resulting in a higher coverage and a denser pattern. As discussed in Chapter 1.5, surface reconstructions can be induced. Additionally, although UHV conditions are useful for surface characterization, it is at higher pressures that catalytic reactions occur. Efforts have been made to combine UHV and higher pressure studies by checking the surface under UHV before and after higher pressure dosages. It is, however, not always useful, since materials under UHV may behave differently than under ambient pressures. For instance, CuO phases can be stabilized in air, but cannot be

stabilized under UHV. Thus, to study catalytic processes, in situ ambient pressure techniques are necessary. By combining the novel in situ techniques and well-studied UHV surfaces, we can achieve a further understanding of catalytic mechanisms.

2.2 Scanning Tunneling Microscopy

Scanning tunneling microscopy (STM) was invented by Gerd Binnig and Heinrich Rohrer in 1981.[58] The two scientists received the Nobel Prize in Physics in 1986 shortly after the STM was designed. Ever since its invention, STM has become one of the very few tools that can resolve surface structures at atomic level. Because STM is based on electron current between sample and tip, materials resolved by STM need to be conductive or semi-conductive,[59] such as metal oxide,[60] polymer,[61] inorganic/organic compound,[62,63] and DNA.[64]
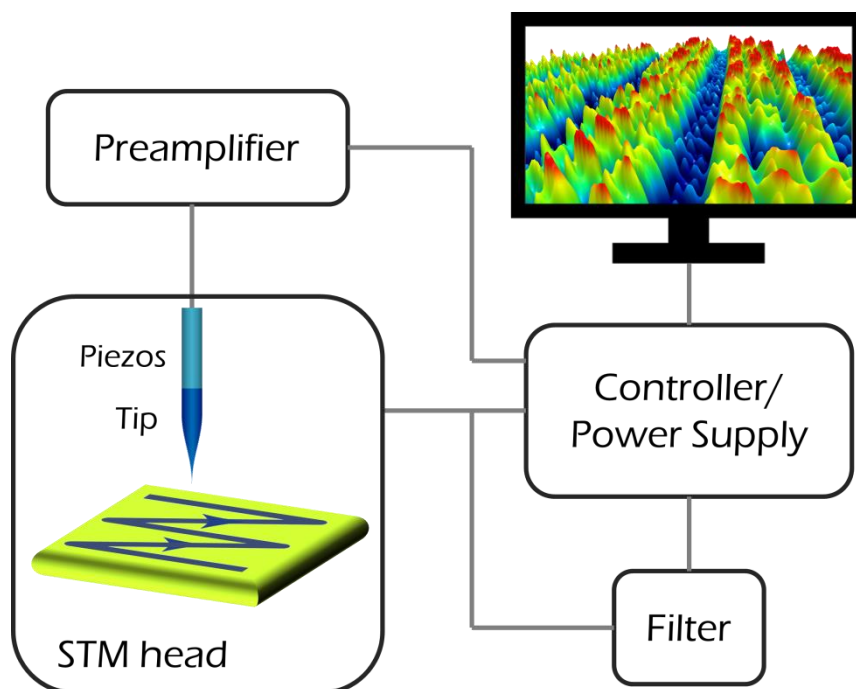
Figure 2.2 *Configuration of STM settings.*

A simple configuration of a scanning tunneling microscope is shown in Figure 2.2. Important components include a sample, a tip, usually $KOH_{(aq)}$ etched W tip or manually cut Pt-Ir tip, piezoelectric scanners to control tip movement, a feedback loop, and sophisticated software to interface with the hardware for scanning and to process the resulting imaging. An STM measurement can be presented as 3D image, 2D image with color corresponding to the apparent height, and differential 2D image with an emphasis on height changes. A few examples are presented in Figure 2.3.
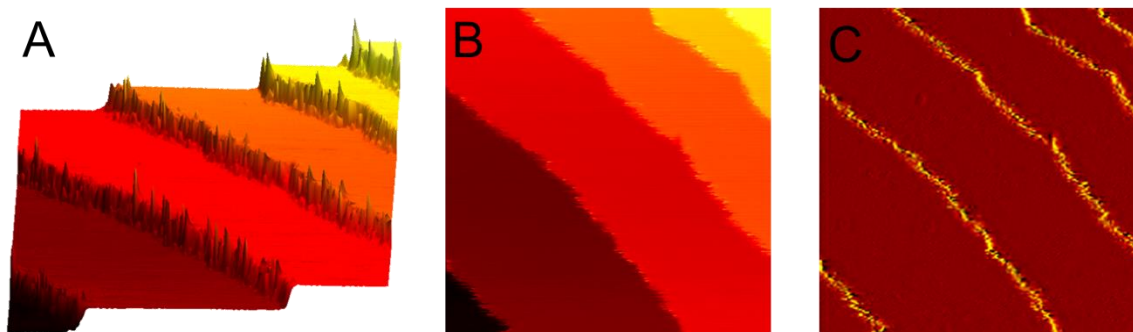
Figure 2.3 *STM images of Cu(111) at 295 K. A) 3D version; B) 2D version with color corresponding to the apparent height; C) differential 2D version with an emphasis on height changes. All of the images are 35×35 nm^2, I_t=0.47 nA, V_t=1.25 V.*

The quality of the STM images is greatly affected by the sharpness of tips. Generally speaking, the sharper the tip is, the better the structure is resolved. Sometimes, when the tip has a double end, which means two points are tunneling at the same time, features have shadows on the image. It can be easily detected by an experienced user. Other factors that can affect image quality include the stability of tips, scanning conditions, mechanical, acoustical and electrical noise level of the environment.

2.2.1 Theory of scanning tunneling microscopy

In bulk materials that have a large amount of atoms, the energy levels merge into electron bands with an energy distribution. The number of energy levels in each energy gap of ΔE, is called the density of states (DOS), Figure 2.4. The DOS can be further divided into filled states with electrons and empty states without electrons. At 0 K, the top energy level occupied by the electron is called Fermi level (E_F). The least energy required to excite an electron in to the vacuum is called the work function (ϕ). The DOS, Fermi level and work function are intrinsic properties of a material.
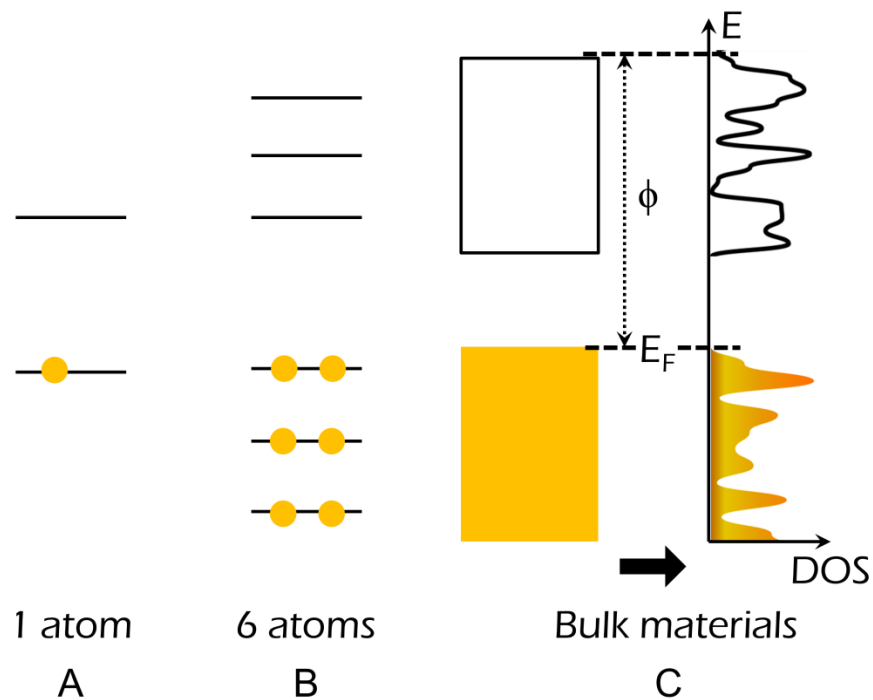
Figure 2.4 *Schematic of electron configurations in A) a single atom; B) 6 atoms; C) bulk materials.*

In terms of STM, when tip and sample are far away in vacuum and do not have any interaction, each maintains its own Fermi level and work function (Figure 2.5A). When tip and

sample contact each other (tip crashes into surface), and after reaching electrical equilibrium, they share the same Fermi level and there is no tunneling current but an electric field between the two (Figure 2.5B). Only when tip and sample are close enough but not in contact, usually within 1 nm, a small amount of current can tunnel from filled states to empty states when driven by a small voltage V (Figure 2.5C). Generally speaking, the tip is grounded, and the sample is biased on the scanning stage, i.e. with a positive voltage empty states of the sample are imaged; and with a negative voltage filled states of sample are imaged.
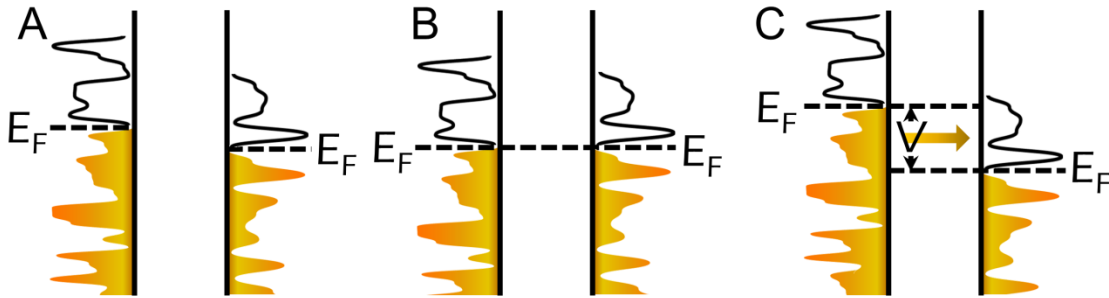
Figure 2.5 *Schematics of Fermi level changes under conditions of A) tip and sample far away; B) tip and sample contact; C) tip and sample within tunneling distance.*

The theoretical description is well known for tunneling effects.[65,66] The equation for tunneling current (I_t) is:

$$I_t = \frac{4\pi e^2}{\hbar} V_t \rho_s(E_F) \rho_t(E_F) |M_{mn}|^2 \qquad (2.2)$$

Here, V_t is the voltage applied between the sample and tip, e corresponds to the charge of an electron, $\hbar$ is the Planck constant, ρ_s and ρ_t correspond to the DOS of sample and tip respectively, E_F corresponds to Fermi level, and M_{mn} corresponds to the matrix element of the transition probability between two states with an expression of:

$$M_{mn} = -\frac{\hbar^2}{2m} \int (\psi_m^* \nabla \psi_n - \psi_m \nabla \psi_n^*) dS \qquad (2.3)$$

where ψ_m, ψ_n refer to the wave functions of the mth and nth state, and dS is a surface element. If we make assumptions that only s-like orbitals contribute to tunneling and the radius of the tip end is R, then the DOS of tip near Fermi level can be written as

$$\rho_t(E_F) \propto e^{-2\kappa(R+d)} \qquad (2.4)$$

where d is the distance between the tip and sample, and κ is the inverse decay length with an expression of

$$\kappa = \sqrt{\frac{m(\phi_t+\phi_s)}{\hbar^2} - E + \frac{eV_t}{2} + k_\parallel^2} \qquad (2.5)$$

Here, m is the mass of an electron, ϕ_t and ϕ_s are work functions of tip and sample, E is the energy of states related to Fermi level, and $k_{//}$ is the parallel momentum of the surface electronic state. After combining equations from (2.2) to (2.5), the equation for tunneling current can be written as:

$$I_t \propto \int_0^{eV} \rho_s(E) e^{-2\kappa d} dE \qquad (2.6)$$

In the low bias range, equation 2.6 can be further simplified as:

$$I_t \propto \frac{CV_t}{d} e^{-2\kappa d} \qquad (2.7)$$

where C is a constant.

Thus, the expression shows that: with a certain voltage and known sample and tip, the tunneling current is exponentially dependent on the distance between the two. Experimentally,

this leads to two scanning modes. 1) Constant current mode: where the feedback loop makes sure the tunneling current is maintained constant during scanning, i.e., the distance between tip and sample is adjusted constantly. The mapping of tip movements in z direction is interpreted as the topography of DOS. 2) Constant height mode: where the feedback loop is turned off so the height between tip and sample changes during scanning. The information of tunneling current change in x and y directions is interpreted as electronic density. This mode is not widely used, since scanning at rough surface with constant height may lead to tip crash. It's worth mentioning that STM does not measure the physical height directly, instead, it measures the apparent height reflected by DOS.

2.2.2 Ambient pressure scanning tunneling microscopy

The primary instrument used in my dissertation research was an ambient pressure STM (AP-STM, also known as high pressure STM, or STM reactor) allows the surface electronic topographical changes to be collected while surface is under elevated pressures. The AP-STM technique is on the cutting edge of STM development, and has been commercialized by SPECS and Leiden Probe Microscopy B.V. STM can be used from UHV all the way to atmospheric pressure and above. However, in terms of scanning at elevated pressures, two major concerns need to be minded.[32] 1) The size of the STM reactor needs to be small. If the reactor is large, the possibility of gas molecules adsorbing and eventually reacting with walls is high, so is the sensitivity of the experiment to the gas impurities. These unwanted gas-phase species can potentially adsorb on the surface and block reactive sites. Additionally, the idea of designing a small high pressure cell including the STM inside allows the preparation of samples in a pristine UHV environment and ensures other that the rest of the system remains under UHV conditions during AP experiments, and minimizing the impurities going into UHV chamber with high

19

pressure gases. 2) The piezo needs to be protected from reactive gasses for the purpose of a stable performance. In this dissertation, a commercial SPECS Aarhus 150 NAP STM is the primary instrument used.
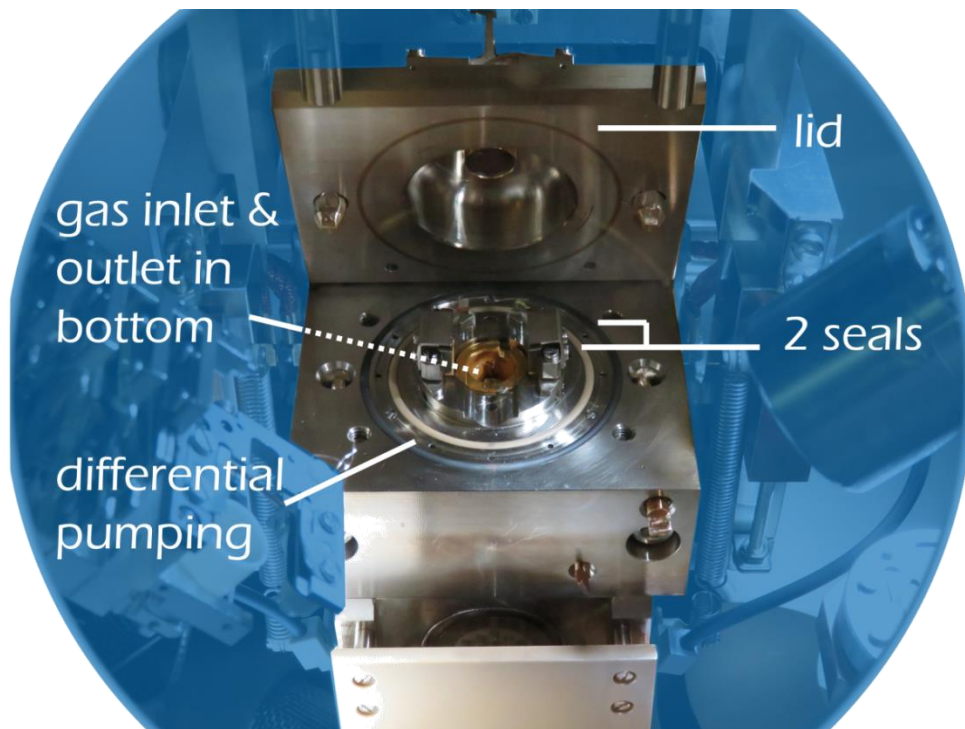
Figure 2.6 *The high pressure cell of SPECS Aarhus 150 NAP STM.*

The high pressure cell of the SPECS Aarhus 150 NAP STM has a lid that can be opened, loosely closed or sealed, Figure 2.6. The two O-ring seals and differential pumping ensure that the pressure in the rest of the STM chamber remains under UHV conditions, when the cell is filled with gases like CO, O_2 and CO_2 at pressures of $\leq$ 75 Torr. Even when H_2 is used, the pressure in the main chamber remains in the low 10^{-9} Torr. Prior to entering the cell, high purity gases are further purified with appropriate traps and maintained in a six-way cross monitored by a capacitance manometer (MKS, baratron gauge 626B). Reactant gases are trapped during high pressure experiments. In the particular configuration in our lab, high pressure gases share one capillary inlet and outlet, which is located in the bottom of the cell.

2.3 X-ray Photoelectron Spectroscopy

X-ray photoelectron spectroscopy, also known as electron spectroscopy for chemical analysis (ESCA), was developed based on the photoelectric effect (Albert Einstein, the Nobel Prize in Physics 1921). A commercial instrument became available around 1970.[67] The further development of high-resolution electron spectroscopy was then awarded Nobel Prize in Physics in 1981 to Kai M. Siegbahn. Nowadays, it is one of the most mature and powerful tools in surface science to identify elements, its oxidation states and the chemical identity of adsorbates.
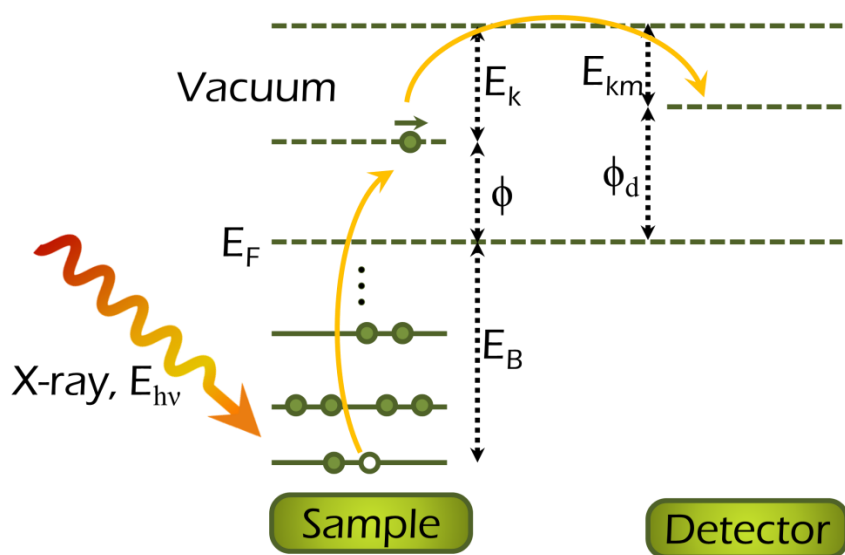
Figure 2.7 *Schematic of X-ray photoemission process.*

When an X-ray beam irradiates at an element, it will excite core shell electrons to vacuum, Figure 2.7. The energy conservation equation of the process is

$$hv = E_B + \phi + E_k \tag{2.8}$$

where hv is the energy of the X-ray, E_B is the binding energy of the core shell electron, ϕ is the work function of the material, E_k is the kinetic energy of the excited electron in vacuum. In XPS

set-ups, both the sample and detector are grounded and have the same Fermi level, shown in Figure 2.7. Thus the binding energy of the core shell electron and measured kinetic energy E_{km} is

$$E_B = h\nu - \phi - E_k = h\nu - E_{km} - \phi_d \qquad (2.9)$$

where ϕ_d is the work function of detector. The binding energy of core shell electrons can be obtained without knowing the work function of sample materials. The sampling depth can be calculated according to the Beer-Lambert law. Assuming the initial intensity of a photoelectron is I_0, and the intensity when it reaches surface at a normal angle and from a depth (d) below surface is I, then we have:

$$I = I_0 \cdot exp(-d/\lambda) \qquad (2.10)$$

where λ is the inelastic mean free path. The sampling depth is referred as the depth where 95% of electrons are scattered by reaching the sample surface. According to equation 2.10, sampling depth is 3λ. Based on the "universal curve" of electron inelastic mean free path,[68] sampling depth for AlKα radiation is 3~10 nm.
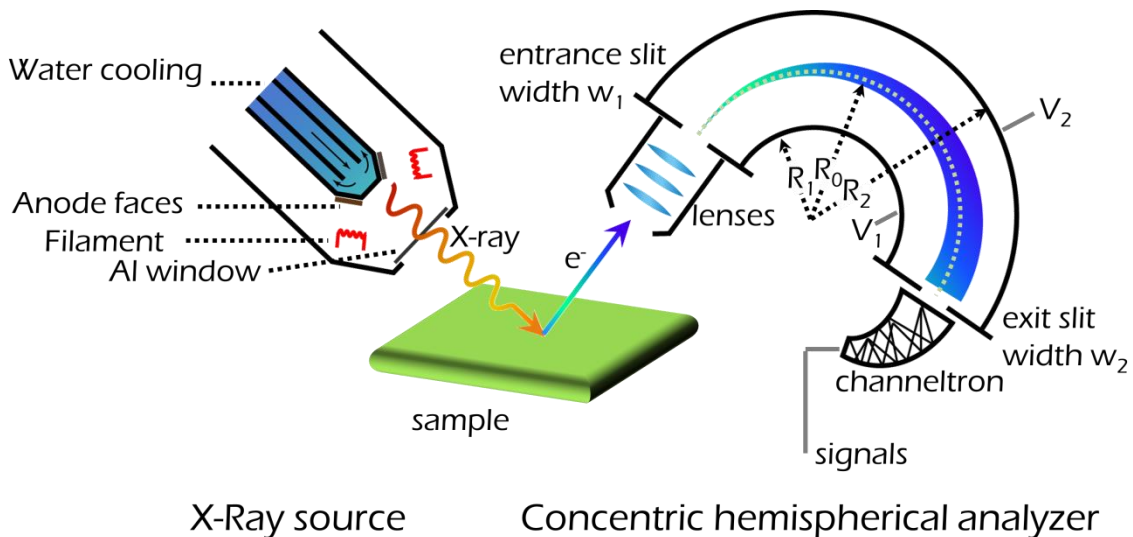
Figure 2.8 *Schematic of XPS configurations.*

The X-ray source and concentric hemispherical analyzer (CHA) are crucial parts of the XPS technique. The X-rays are generated from different anode materials that are excited by a high energy electron beam (typically 10-15 keV). In lab-based XPS, Mg and Al anodes are commonly used to generate X-rays at the Mg Kα line at 1253.6 eV (width of 0.7 eV) and the Al Kα line at 1486.6 eV (width of 0.85 eV), respectively. The kinetic energy distribution of the sample's core shell electrons ejected by the interaction with X-rays is collected and analyzed by a concentric hemispherical analyzer (within one inch away). Electrons travel through an electrostatic lens system to get focused and enter the entrance slit. Different voltages ($V_2 > V_1$, Figure 2.8) are applied on outer and inner hemispheres so that the potential of the median equipotential surface V_0 is

$$V_0 = \frac{V_1 R_1 + V_2 R_2}{2R_0} \tag{2.11}$$

Here, R_1 and R_2 are the radii of the inner and outer hemispheres and R_0 is the radius of median equipotential surface. Electrons with kinetic energy $E_0 = eV_0$ entering the first slit (width of w_1) can follow the hemispheric pathway and exit through second slit (width of w_2). Electrons with other kinetic energies cannot follow the right pathway to the exit. Thus, E_0 is called the pass energy. The selected electrons are then detected by a channeltron or electron multiplier and are further converted to signals via XPS software. The resolution of the detected kinetic energy ΔE is defined as follows

$$\Delta E = E_0 \frac{(w_1 + w_2)}{2R_0} = \frac{e(V_1 R_1 + V_2 R_2)(w_1 + w_2)}{4R_0^2} \tag{2.12}$$

In order to maintain a constant resolution across the whole spectrum, potentials applied on the hemispheres and slit widths should be maintained the same. In other words, the kinetic energies

of electrons emitted from surface are not analyzed by changing voltages on the hemispheres. Instead, the electrostatic lens system accelerates/decelerates the incoming photoelectrons to meet the pass energy defined by V_0. A typical XPS spectrum is plotted as intensity vs. binding energy, shown in Figure 2.9. The two peaks at 298.0 eV and 293.2 eV indicate that K^+ exists on the surface.
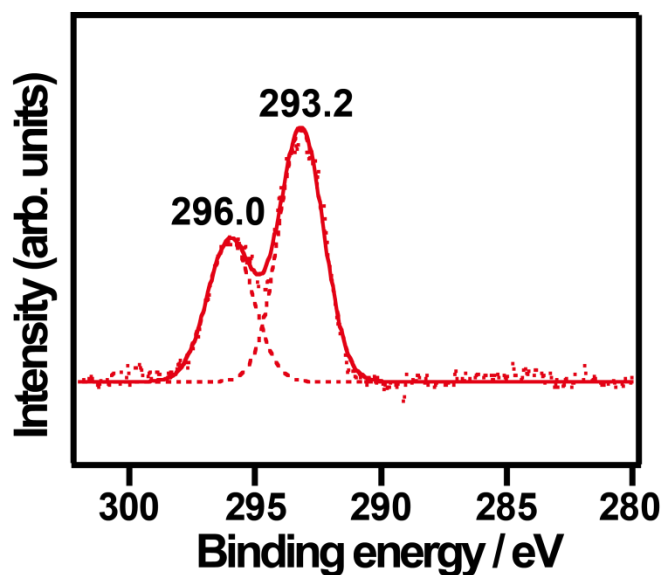
Figure 2.9 *A typical XPS spectrum shown electrons from potassium 2p orbitals.*

2.4 Infrared Reflection Absorption Spectroscopy

Infrared reflection absorption spectroscopy (IRRAS) uses reflected infrared (IR) beam to detect the vibrational spectrum of adsorbate molecules. The sample surface doesn't need to be transparent, but reflective. When a probe molecule is used, IRRAS is only sensitive to the top layer, which is more surface sensitive than XPS. Besides identifying functional groups of adsorbates, IRRAS is able to identify local environment with the help of a probe molecule, such as CO.

p-polarized light: IR active
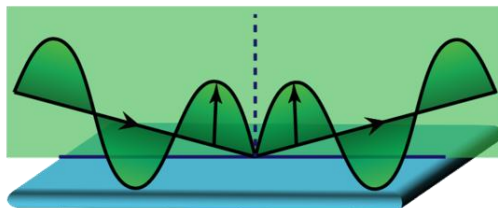
s-polarized light: IR inactive
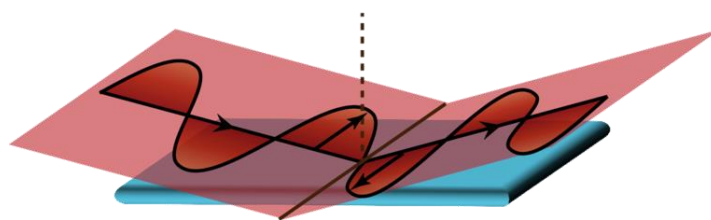
Figure 2.10 *Schematic of p- and s- polarized infrared beam reflection.*

An IR beam can be polarized to p and s type. P-polarized light is parallel to the plane of incidence, and s-polarized light is perpendicular to the plane of incidence, shown in Figure 2.10. According to Fresnel equations, if a light is traveling at an incident angle θ_i from a medium to another with refractive indexes of n_1 and n_2 respectively, the intensities of reflected s- and p-polarized light are calculated as follows

$$R_p = (\frac{n_2 cos\theta_i - n_1 cos\theta_t}{n_2 cos\theta_i + n_1 cos\theta_t})^2 \tag{2.13}$$

$$R_s = (\frac{n_1 cos\theta_i - n_2 cos\theta_t}{n_1 cos\theta_i + n_2 cos\theta_t})^2 \tag{2.14}$$

where R_p and R_s stand for intensities of reflected p-polarized light and s-polarized light respectively, θ_t is the refraction angle. In UHV systems, $n_1 = 1$. In order for a molecule to be IR active, the bond vibrations should be excited by the electric field of the infrared beam. At an

25

incident angle of 90°, both p- and s-polarized lights form standing waves, ending up with no electric field on the reflection point. When θ_i is less than 90°, the electric field of p-polarized light has a net contribution in the direction normal to the sample plane, and the electric field of s-polarized light barely has any contribution in any direction. Thus, only p-polarized light is IR active, and best for grazing angles. Additionally, in order to be IR active, the dipole moment of detected molecule should have a component perpendicular to the sample plane.

Similar to commonly used Fourier-transform infrared spectroscopy (FTIR), IRRAS applies the Michelson interferometer to generate interferogram, which is further converted to a spectrum via Fourier transformation. The spectrum obtained by IRRAS is called differential reflectance spectrum ($\Delta R/R$). For the metallic substrate, it is calculated as[69]

$$\Delta R/R = J_2(\varphi_0)\frac{R_p - R_s}{R_p + R_s} \tag{2.15}$$

Here, $J_2(\varphi_0)$ is a second order Bessel function, referring to the efficiency of photoelastic modulator with wavenumbers. This factor can be removed after removing background spectrum.

The vibrational spectra of adsorbed molecules are greatly affected by local environment in terms of peak positions, intensities and shapes. Thus, IRRAS can provide information of adsorption states, molecule binding geometries and bonding information. A typical IRRAS spectrum is shown in Figure 2.11. The spectrum was collected where 2×10^{-9} Torr of CO adsorbs on pitted Cu(111) at 100 K. The two peaks at 2100 cm^{-1} and 2071 cm^{-1} are from CO adsorption on Cu atoms with coordination numbers of 6 and 9, respectively.
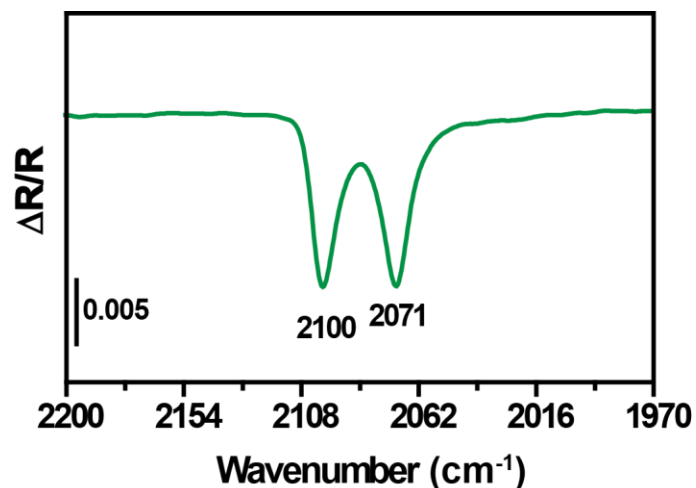
Figure 2.11 *IRRAS spectra of 2×10^{-9} Torr CO adsorption on pitted Cu(111) at 100 K.*

2.5 Summary

This chapter discussed basic theories about UHV, STM, XPS and IRRAS, which are important conditions and techniques used in this dissertation. Samples in later chapters are prepared and stored under UHV conditions before and after experiments. In chapter 3 to chapter 6, STM is used for topographic studies, XPS is used to identify surface species, and IRRAS is used to investigate coordination number and oxidation states of copper. By combining the three techniques, a comprehensive understanding is achieved of the Cu-based model catalysts under ambient pressure conditions.

Chapter 3. Cu(111) under Ambient Pressure Gases

Part of this chapter is adapted from *Phys. Chem. Chem. Phys.* **2015**, *17*, 3032.

3.1 Introduction
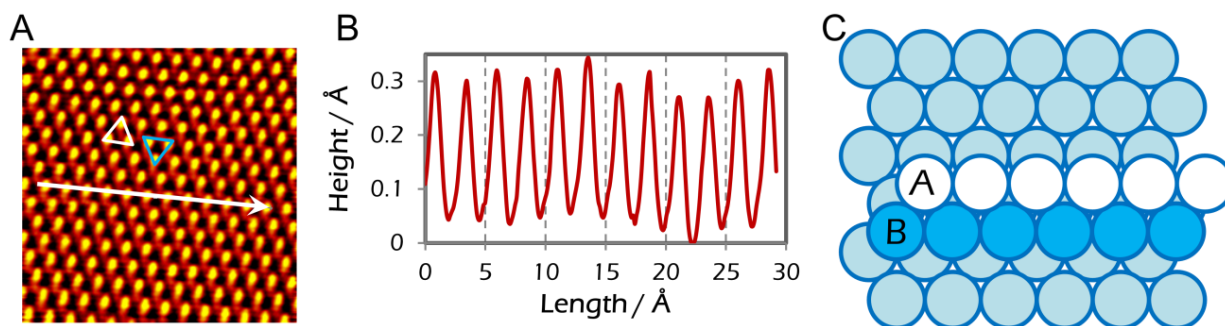
Figure 3.1 *A) An STM image of atomic scale Cu(111) at 300 K. Image size is 33×33 nm². I_t = 0.98 nA; V_t = 0.81V. The white triangle indicates an fcc hollow site and the blue triangle indicates a hcp hollow site. B) The linescan profile follows the white arrow in A). C) Type A and B step edges on (111) plane.*

As discussed in Chapter 1.2.1, Cu(111) is used as a substrate in this dissertation. An atomically resolved STM imaged and a linescan is shown in Figure 3.1. Each bright protrusion is a copper atom. Calculated from the lattice constant of copper,[70] the spacing of copper atoms within the Cu(111) plane is 2.56 Å, which gives a primitive unit cell area of 5.67 Å². The sites on Cu(111) include 1) a-top, the position on top of a copper atom; 2) bridging site, the position in between two copper atoms; 3) face-centered cubic (fcc) hollow site, the position with ABA

packing (white triangle in Figure 3.1); 4) hexagonal close packed (hcp) hollow site, the position with ABC packing (blue triangle in Figure 3.1). Preference on adsorptions sites varies by different molecules and conditions. If molecules adsorb on Cu(111) with a close-packed structure, step edges formed along fcc and hcp adsorption sites are (001) A and (111) B type step edges respectively,[71,72] Figure 3.1 C.

Copper atoms are very mobile on Cu(111) at 300 K. It has been reported that single copper atoms can change surface sites on Cu(111) at the temperature as low as 10 K, and copper dimers can diffuse locally at 7 K.[73] At 300 K, Cu atoms of close packed structure are very stable within terraces and do not diffuse in long range. However, Cu atoms near step edges diffuse rapidly. A sputtered Cu(111) surface only adopts the most thermo-stable hexagonal shaped pits, and step edges of Cu(111) change shape over time under UHV at 300 K, shown in Figure 3.2.
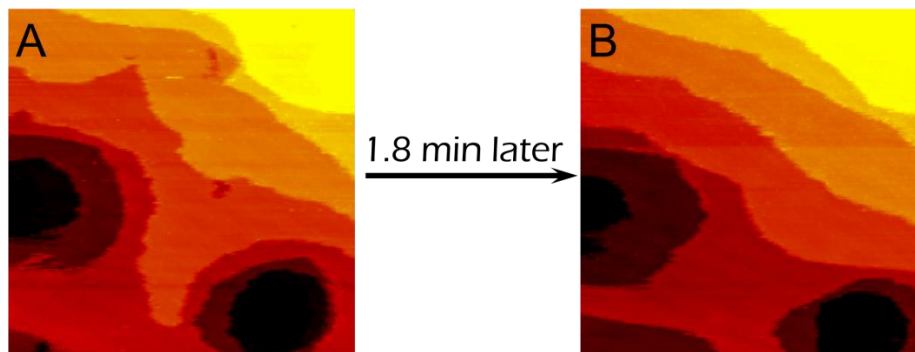
Figure 3.2 Highly mobile copper step edges at 300 K. A) An STM image of gently sputtered Cu(111). B) The same area imaged 1.8 min later. STM images are 65×65 nm². $I_t = 0.55$ nA; $V_t = 1.36V$.

Cu-based catalysts are used in a variety of catalytic reactions involving O_2, H_2, and/or CO, such as water gas shift reaction,[74] methanol synthesis,[75] preferential oxidation reaction,[44] etc. Extensive studies have been done on gas-surface interactions on Cu(111).[76-78] Add-layer structures, diffusion rates and gas induced Cu(111) topographic changes were discussed.

However, most studies have been done under high vacuum conditions and/or at low temperatures in order to chemisorb molecules on surfaces. The adsorption rate (r_a) for non-dissociative gas molecules on the surface can be calculated based on the following equation:[79]

$$r_a = FS = \frac{p}{N_0\sqrt{2\pi mkT}} \times S \tag{3.1}$$

where S is the sticking coefficient; F is the collision rate, which is calculated from the Hertz-Knudsen equation; N_0 is the number of adsorption centers per unit of surface area; m is the mass of the adsorbing molecule; k is the Boltzmann constant; T is the temperature; p is the gas phase pressure. According to equation (3.1), increasing the gas phase pressure or decreasing temperature can promote adsorption rate. New surface features may develop under ambient pressure (AP) gasses. Additionally, AP studies bridge the pressure gap between conventional UHV and industrial scale conditions. Thus, it is necessary and important to study gas-surface interactions under AP conditions, which is the focus of this chapter.

Conventionally, Cu(111) is smooth and most surface atoms have a coordination number of nine. However, defects and under-coordinated sites such as kinks and step edges are more catalytic active. The degree of defects/roughness of the (111) metal surface can be controlled by low-energy ion bombardment without changing crystallinity.[80] In this case, nano-pits with a few layers deep can be created. It is essential for the understanding of catalytic reactions to study the dynamic change and stability of the under-coordinated sites under ambient pressure gasses. Thus, AP studies of small gas molecules on pitted Cu(111) are discussed in this chapter and compared with smooth Cu(111) surfaces.

3.2 Experimental Methods

A commercialized SPECS™ Aarhus HT-NAP STM was used for high pressure and UHV surface topography studies with a tungsten tip and a background pressure of 5×10^{-10} mbar.[60] A commercial Fourier transform infrared spectrometer (Bruker, IFS 66v/S) in a homemade IRRAS equipped with a UHV chamber and a high pressure reactor was used for studies on local environment.[80] A K-type thermocouple was directly attached to the edge of Cu(111) sample for accurate temperature controlling. XPS data was obtained with a commercialized SPECS design at center of functional nanomaterials, Brookhaven National Laboratory.

A Cu(111) sample (Princeton Scientific Corp.) was cleaned by Ar^+ sputtering and 800 K UHV annealing cycles. If needed, nano-pits on Cu(111) were generated by gentle sputtering at near normal incidence (1.0 keV Ar^+, ~1 A/cm^2). High pure CO (GTS-WELCO, 99.999%), O_2 (GTS-WELCO, 99.9999%) and H_2 (GTS-WELCO, 99.9999%) gases were further purified in liquid nitrogen traps prior to being introduced to Cu(111). Atomic hydrogen was made by flowing molecular hydrogen through a leak valve to an atomic hydrogen source (Omicron "EFM H").

3.3 Results and Discussion

3.3.1 Ambient pressures of CO up to 30 Torr

CO is commonly used as a probe molecule in IRRAS, because of its intense IR signal and the sensitivity to local environments and adsorption sites. At UHV conditions, CO adsorbs weakly on a-top sites of Cu(111) with an IRRAS peak at 2071 cm^{-1},[81,82] and desorbs from Cu(111) above 175 K.[83] Since the adsorption process is enhanced by increasing CO pressures, a

series of AP-IRRAS experiments was conducted to investigate the minimum pressure required for CO to adsorb on Cu(111) at 300 K, Figure 3.3. At pressures below 48 mTorr, only gas phase CO is observed with a broad featured centered at 2143 cm^{-1}. At pressures above 64 mTorr, both a CO adsorption peak on Cu(111) at 2070 cm^{-1} and gas phase CO peak are observed, with the former growing faster than the latter as the pressure increases. At 1 Torr of CO, the IR peak intensity for adsorbed CO is higher than that for gas phase CO by a factor of two. It is worth mentioning that high pressure dependent CO adsorption on single crystals has also been reported on Au(111).[84] Upon annealing CO adsorbed Cu(111) to 325 K under 1 Torr of CO, a large fraction of CO desorbs as shown in Figure 3.3. Further annealing to 350 K leads to a complete desorption, leaving only CO gas phase peak in the IRRA spectrum. The results in Figure 3.3 show that CO absorbs on Cu(111) at pressure higher than 64 mTorr CO at 300 K and 1 Torr of CO desorbs completely at 350 K. Furthermore, the IR peak position at 2070 cm^{-1} indicates CO occupies a-top adsorption sites. CO adsorption on bridging and hollow sites in Cu(111) generates an IR peak at 1835 cm^{-1} and 1814 cm^{-1} respectively,[85] which are not observed.
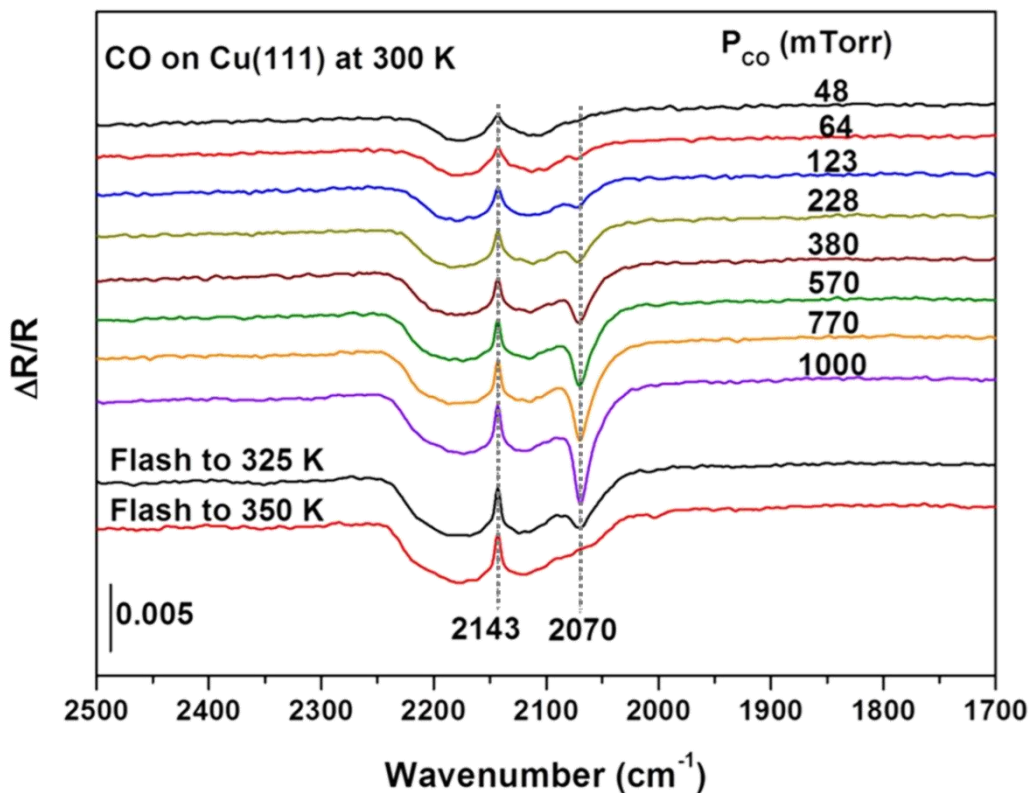
Figure 3.3 *AP-IRRA spectra obtained following the exposure of Cu(111) to CO as a function of CO pressure at 300 K. The peak for CO_{ad} (2070 cm^{-1}) grows in intensity as the CO pressure increases, and CO desorbs after flashing to 350 K, leaving a gas phase CO peak (2143 cm^{-1}).*

A series of AP-STM experiments was also conducted to investigate Cu(111) surface under high pressures of CO, Figure 3.4. Cu(111) barely changes under 10 mTorr CO, Figure 3.4A. When CO pressure is above 0.75 Torr, Cu(111) surface is greatly roughened, along with a dendritic growth from step edges and small islands on terraces appear, Figure 3.4B to 3.4F. As CO pressure increases, the percentage of dendritic growth decreases and that of small islands on terraces increase. The structural changes will be discussed one by one in the following section.

33
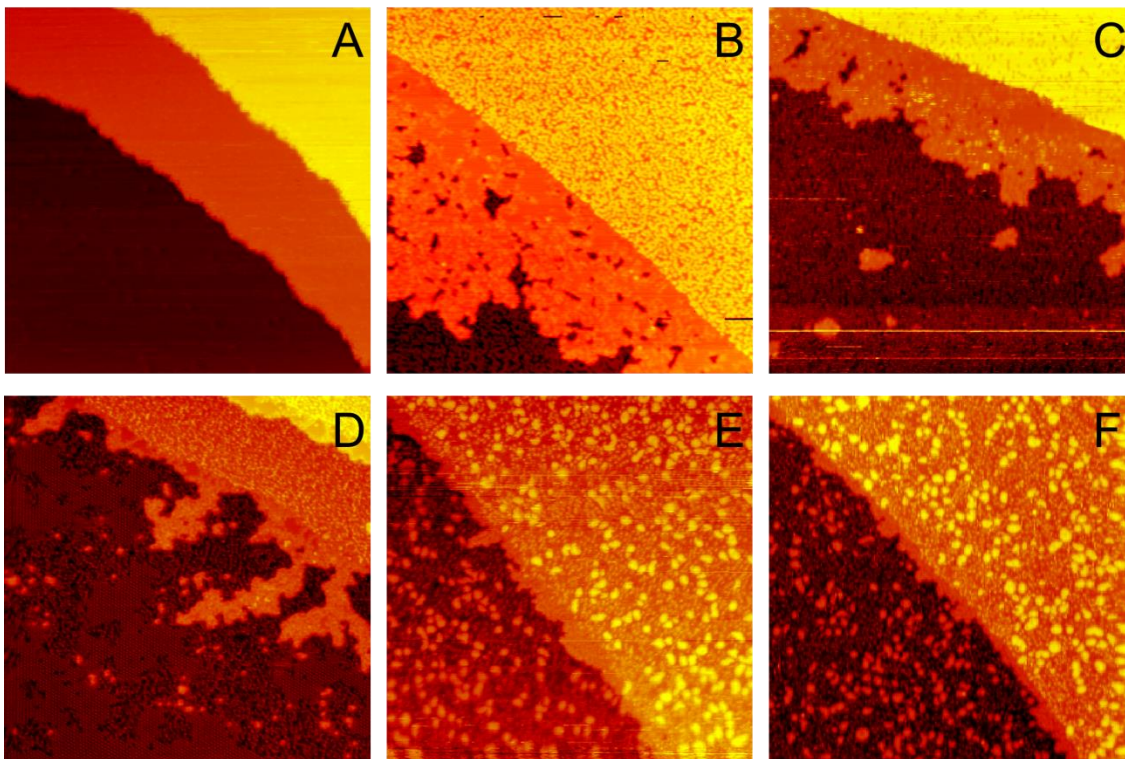
Figure 3.4 *In situ AP-STM images of Cu(111) exposed to A) 0.01 Torr CO for 2.3 h; B) 0.75 Torr CO for 2.4 h; C) 1 Torr CO for 1.5 h; D) 10 Torr CO for 2.0 h; E) 30 Torr CO for 1.8 h; F) 35 Torr CO for 2.0 h. All images are 70×70 nm^2, $I_t = 0.50 \sim 0.97$ nA; $V_t = 0.69 \sim 2.15$ V.*

The process of Cu(111) roughening under 700 mTorr CO is presented in Figure 3.5. From Figure 3.5A to 3.5D, after CO was introduced to Cu(111), more and more dark points appear making the surface rougher and rougher. CO molecules can be imaged as dark or bright depending on whether a CO molecule is at the tip apex.[77,86] Thus, it is possible that during high pressure experiments, the STM tip picks up a CO molecule and images CO_{ad} as bright dots. Figure 3.5E and 3.5F show the same Cu(111) surface before and after evacuating CO. It is obvious that a great number of dark features disappear, but some still remain on the surface. Thus, there are two types of surface species that are both imaged as dark. It's very likely that the dark features that can be pumped away are CO molecules, since CO adsorption on Cu(111) at 300 K happens only under high pressure.

34
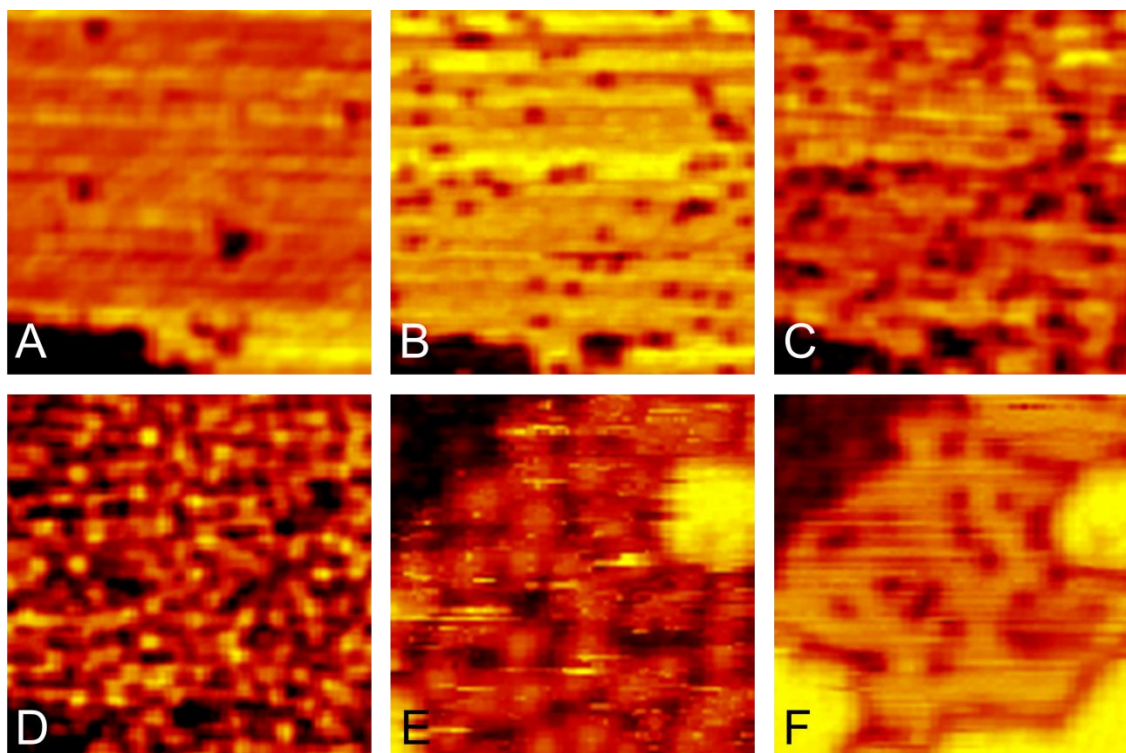
Figure 3.5 *In situ AP-STM images of Cu(111) roughness under CO. A) to D) are of the same area on Cu(111) under 700 mTorr CO. Exposure time from A) to D) are 3 min, 30 min, 45 min, 96 min, respectively. E) shows Cu(111) under 1.8 Torr CO. After 4 min evacuation, the surface is shown in F). Images from A) to E) are 10×10 nm^2; E) and F) are 6×6 nm^2. $I_t = 0.54\sim0.69$ nA; $V_t = 1.32\sim1.63$ V.*

Those dark points remaining on the surface even under vacuum have a size around 8 Å. Since CO does not stick on Cu(111) even over under-coordinated sites under UHV at 300 K,[59] these dark features cannot be physisorbed CO molecules. Considering the high mobility of Cu at 300 K, these disordered dark features are unlikely to be missing copper clusters. It may be chemisorbed CO/metal carbonyl species. Iron and nickel carbonyls are common impurities with CO. Although CO gas is purified through liquid nitrogen trap prior to entering the high pressure cell, it may not remove impurities completely under high pressures. Nickel carbonyl is reported to be stable on Cu(111) at 300 K.[87] Additionally, the size of the dark feature matches the size of reported single copper and iron carbonyls.[88] Since the CO exposure time in IRRAS experiment is

35

short when dark features may be below the detection limit, the fact no peak of carbonyl is observed in IRRAS does not rule out the formation of carbonyl.

A full process of dendritic growth was observed under 10 Torr CO, Figure 3.6. Figure 3.6A is a clean Cu(111) surface with three terraces. 5 min after being exposed to 10 Torr CO, a dendritic growth has clearly started from step edges in descending direction, and the two smaller terraces in the upper right corner have been roughened. The biggest terrace is covered with a hexagonal pattern which will be discussed later. The dendrite grows fast in the first 30 min, and then slows down afterwards as small islands appear and surface gets roughened. Based on size, the growth rate of dendrite is 4.46×10^{-17} m^2/min.
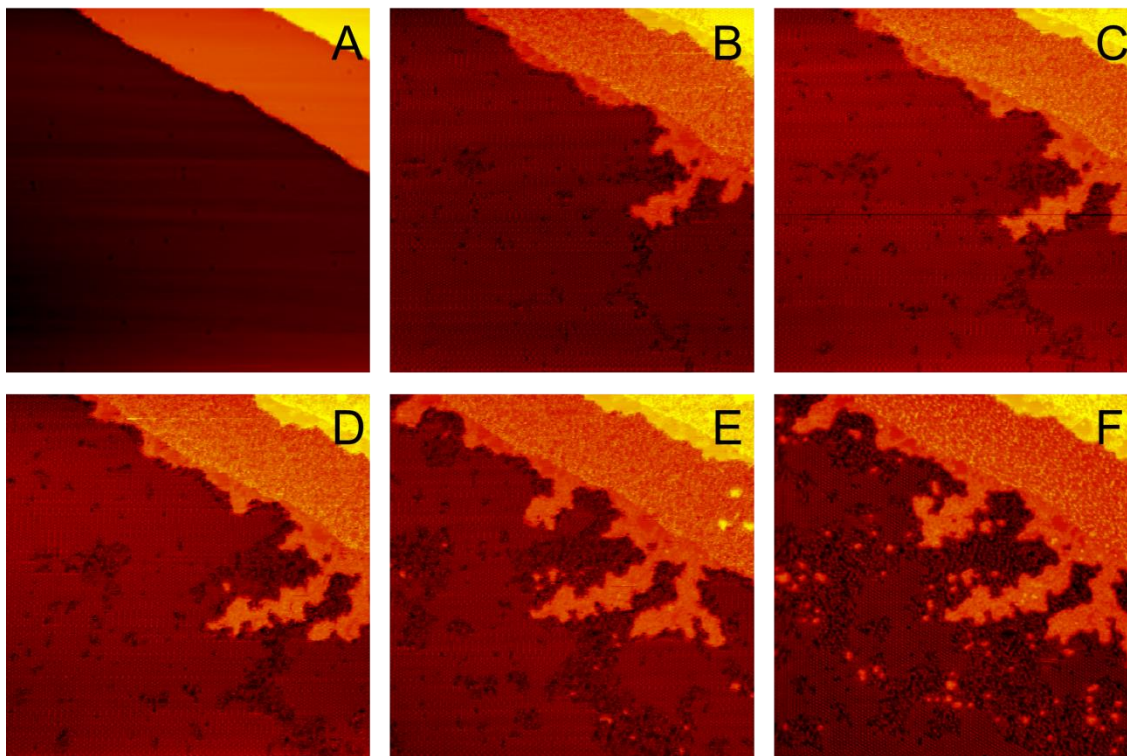
Figure 3.6 *In situ AP-STM images of the topographical change of Cu(111) induced by 10 Torr CO. (A) Clean Cu(111) before CO exposure; (B) to (F) are in situ images of Cu(111) under 10 Torr CO after (B) 5 min, (C) 8 min, (D) 11 min, (E) 29 min, (F) 118 min. All images are 70×70 nm^2, 45°rotated during scanning. I$_t$ = 0.62~0.64 nA, V$_t$ = 0.69~1.32 V.*

Hexagonal patterns on terraces and new growth are clearly shown in Figure 3.7. There are two close packed hexagonal structures on dendritic growth: one with a spacing of 5.2 Å following the <110> direction (Figure 3.7B, blue adsorbates in Figure 3.7E), and the other with a spacing of 4.5 Å 30° rotated from <110> direction (Figure 3.7C, green adsorbates in Figure 3.7E). Written in Wood's notation, pattern in Figure 3.7B is (2×2), and pattern in Figure 3.7C is (√3×√3)R30°. Both patterns have small domains. The (2×2) structure is not common in CO adsorbing on metal (111) planes. The only close situation is CO adsorption on Pd(111) with a pattern of (2×2)-3CO at a coverage near 0.75 ML.[89] However, in Figure 3.7B, CO coverage is only 0.25 ML. Additionally, when CO adsorbs on Cu(111) under UHV conditions, no ordered pattern forms until the local coverage reaches 1/3 ML. Interestingly, the (2×2) pattern only appears near original Cu step edges, which means it forms at early age of dendritic growth. On the other hand, (√3×√3)R30° pattern is commonly seen when CO adsorption on Cu(111)[77] and Pd(111)[89] at a coverage of 1/3 ML under UHV at low temperatures. However, both structures in Figure 3.7B and 3.7C are stable under UHV conditions. That leads to CO_{ad} as an impossible candidate and brings out the possible carbonyl candidates discussed in Figure 3.5F.

A hexagonal close packed feature, Figure 3.7A, covers Cu(111) surface as 10 Torr CO is introduced to the system, and disappears as CO is evacuated. A more cleared image is shown in Figure 3.7D. It is known that a single CO_{ad} on Cu(111) is imaged as a dark point with metallic STM tip, and a bright point with a CO-functionalized STM tip. However, close packed CO are imaged as protrusions under both tips.[77,90] Thus, the pattern in Figure 3.7D is very likely composed of adsorbed CO molecules. The CO adsorbates has a spacing of 6.5Å along 17° off <110> direction. Based on the measurement, a corresponding schematic is drawn as yellow balls in Figure 3.7E. Combining with the IRRAS data that CO adsorbs on a-top sites, the slightly

mismatch is due to image distortion, or local CO tilting.[91] Furthermore, since Cu(111) has mirror symmetry, theoretically, two different domains of CO_{ad} should exist. However, only one big domain is observed covering the whole terrace in the beginning of experiment. In other trials, two domains are both observed. During experiments, the big domain is etched to small parts, which may due to the suspicious carbonyl growth in Figure 3.5F.
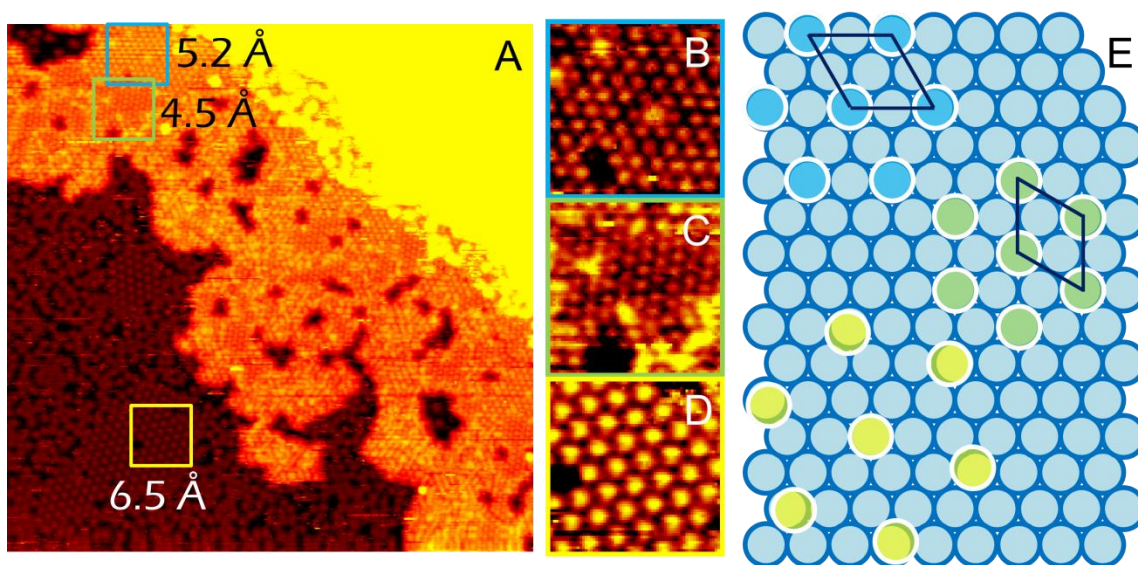
Figure 3.7 *In situ AP-STM images of Cu(111) exposed under 10 Torr CO for 46 min. I_t = 0.63 nA, V_t = 1.63 V. A) 35×35 nm^2. Three areas of 4×4 nm^2 covered by hexagonal patterns with a spacing of 5.2 Å, 4.5 Å, and 6.5 Å are highlighted in blue, green and yellow boxes respectively. B), C) D) are enlarged images of highlights in A) with the same box color. Three corresponding patterns on Cu(111) are drawn in E) based on STM measurements. Balls circled in blue are Cu atom, and balls circled in white are on top features. Blue, green yellows adsorbates correspond to patterns in B), C) and D). The unit cells are drawn in dark lines.*

Figure 3.8 shows STM captures of small island formation under high pressure CO. Figure 3.8A shows a small patch of CO_{ad} on Cu(111) under 10 Torr CO. Within 1 min, a small island suddenly forms on top of the patch during scanning, Figure 3.8B. The small island has the pattern of Figure 3.7B, and remains on the surface after evacuating CO. Remembering that pattern in Figure 3.7B forms during the early stage of dendritic growth, the small islands on terrace may be the same species as dendrite. The small islands can form on ordered areas, Figure

3.8C, or on disordered area but with smaller size and higher mobility, Figure 3.8D to 3.8F.

Figure 3.8D shows a Cu(111) surface after being exposed to 1.8 Torr CO for 24 min. The surface is roughened with no ordered patches. The area is continuous monitored with a rate of 5 min/image. White and blue circles highlight the place where islands form and disappear. Noting that the substrate remains unchanged before and after islands formation, it is very likely that the species of these islands come from gas phase. The small islands formation was also reported on Au/Ni(111) surface alloy. Those islands are interpreted as Au islands due to phase segregation induced by 1000 mbar CO at room temperature.[36] In our case, no obvious copper source is observed for islands and dendrite. Thus, we propose the island and dendritic growth are added on species from high pressures of CO.
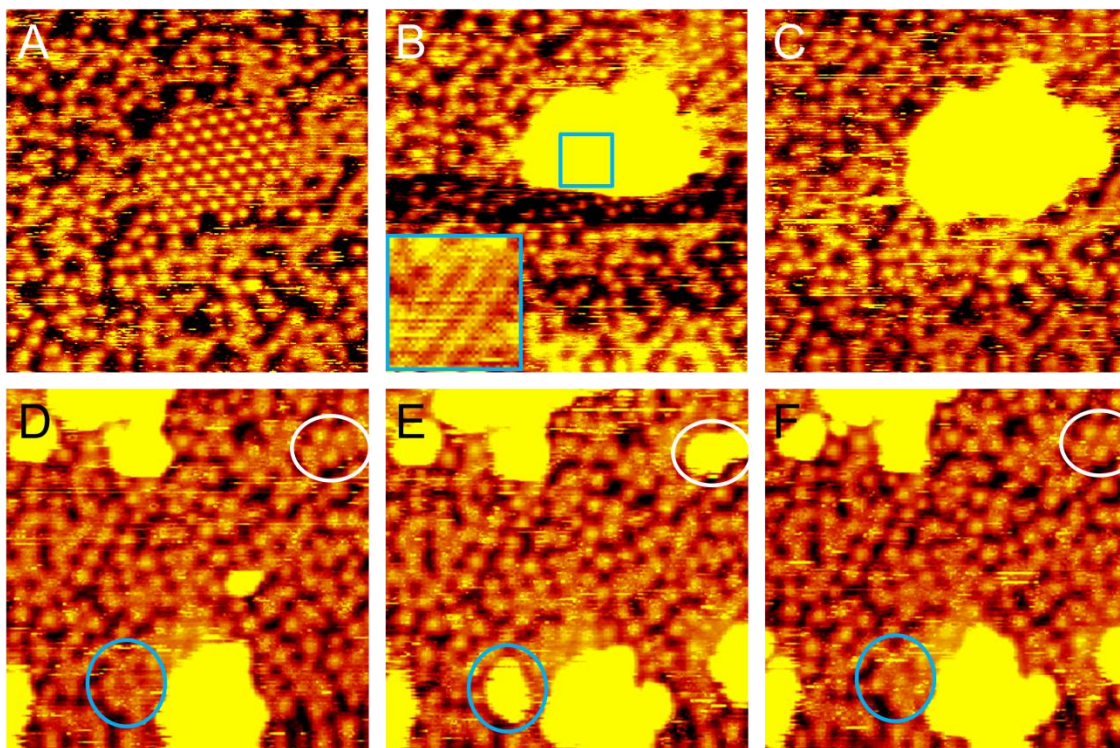
Figure 3.8 *In situ AP STM images of small islands formation during high pressure CO exposing to Cu(111). A) to C) are imaged at the same area under 10 Torr CO for 156 min, 157 min and 158 min. Details of the small island in C) is zoomed in in the insert. D) to F) are imaged at the same area under 1.8 Torr CO for 24 min, 29 min, and 33 min. White and blue circles mark the same place. All of the images are 14×14 nm^2, I_t = 0.31~0.62 nA; V_t = 1.28~1.51 V.*

The evacuation process is shown in Figure 3.9. Figure 3.9A is a Cu(111) surface after being exposed under 10 Torr CO for 3.1 h. The largest terrace is mainly covered by CO pattern in Figure 3.7D. Right after evacuation, the pattern becomes very blurry, Figure 3.9B. The resolution loss may due to the loss of CO on tip apex. Due to the low pumping efficiency, surface pressure gradually reaches 10^{-5} Torr scale after 20 min. Surface are continuously monitored from Figure 3.9C to 3.9I during the evacuating process. As CO patches on terraces gradually disappear, more islands form on terraces. Finally, surface is relative clean with only dendrite and islands. Contrast is exaggerated on purpose in the insert of Figure 3.9I, where a roughened Cu(111) is seen. Thus, the roughen of Cu(111) by high pressure CO at 300 K is irreversible.
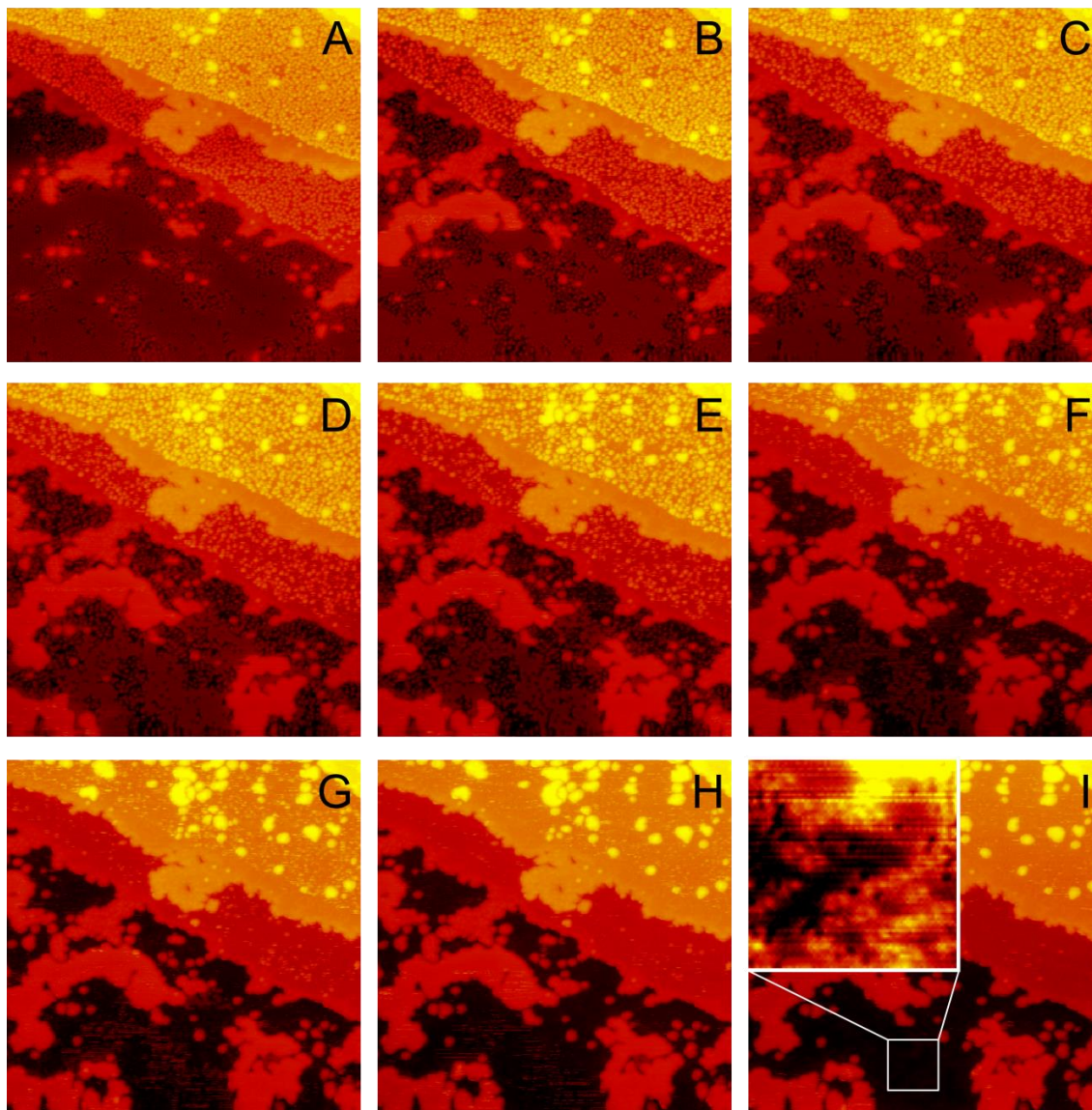
Figure 3.9 *In situ AP-STM images of the topographical change of 10 Torr CO modified Cu(111) after evacuating CO gas for A) 0 min, B) 1.8 min, C) 3.6 min, D) 5.35 min, E) 7.1 min, F) 8.9 min, G) 10.7 min, H) 12.5 min, and I) 14.3 min. All images are 70×70 nm^2, 45° rotated. I_t = 0.43~0.46 nA, V_t = 1.44 V. Details at 10 nm scale are shown in I).*

In order to chemically identify the new growth, an STM and XPS combined technique is used. The topographical changes observed within STM reactor can be then put under vacuum and detected by XPS. The results are shown in Figure 3.10. Spectra of Cu 2p, Ni 2p, C 1s were taken, and only Ni 2p presents an obvious change. The bottom spectrum in Figure 3.10A shows the no nickel related peak is in the Ni 2p spectrum of a clean Cu(111). The corresponding STM

is in Figure 3.10D where both step edges and surface are smooth. With liquid nitrogen cooling the entire CO source in order to remove carbonyl as best as we can, 100 mTorr CO was dosed on Cu(111) for 22 h. After CO was evacuated, the sample surface is imaged as in Figure 3.10C, where surface is covered with point defects and step edges are gently reconstructed. Note that no new growth is observed. The corresponding XPS result is in the middle of Figure 3.10A. Very weak peaks of nickel species at 852.9 eV and 870.2 eV appear. After the liquid nitrogen cooling is removed, the surface is further dosed with 74 mbar unpurified CO for 19 h, when the new growth from the step edges and on terraces is observed in Figure 3.10B. The corresponding Ni 2p spectrum, top in Figure 3.10A, shows an obvious increase of Ni related species. The lab-based X-ray source is not sensitive enough to resolve C 1s peak, which means that the possible small amount carbonyl species formed during the process is not detectable. Thus, by combining XPS and STM, the new growth, or one component of the new growth, is nickel carbonyl.
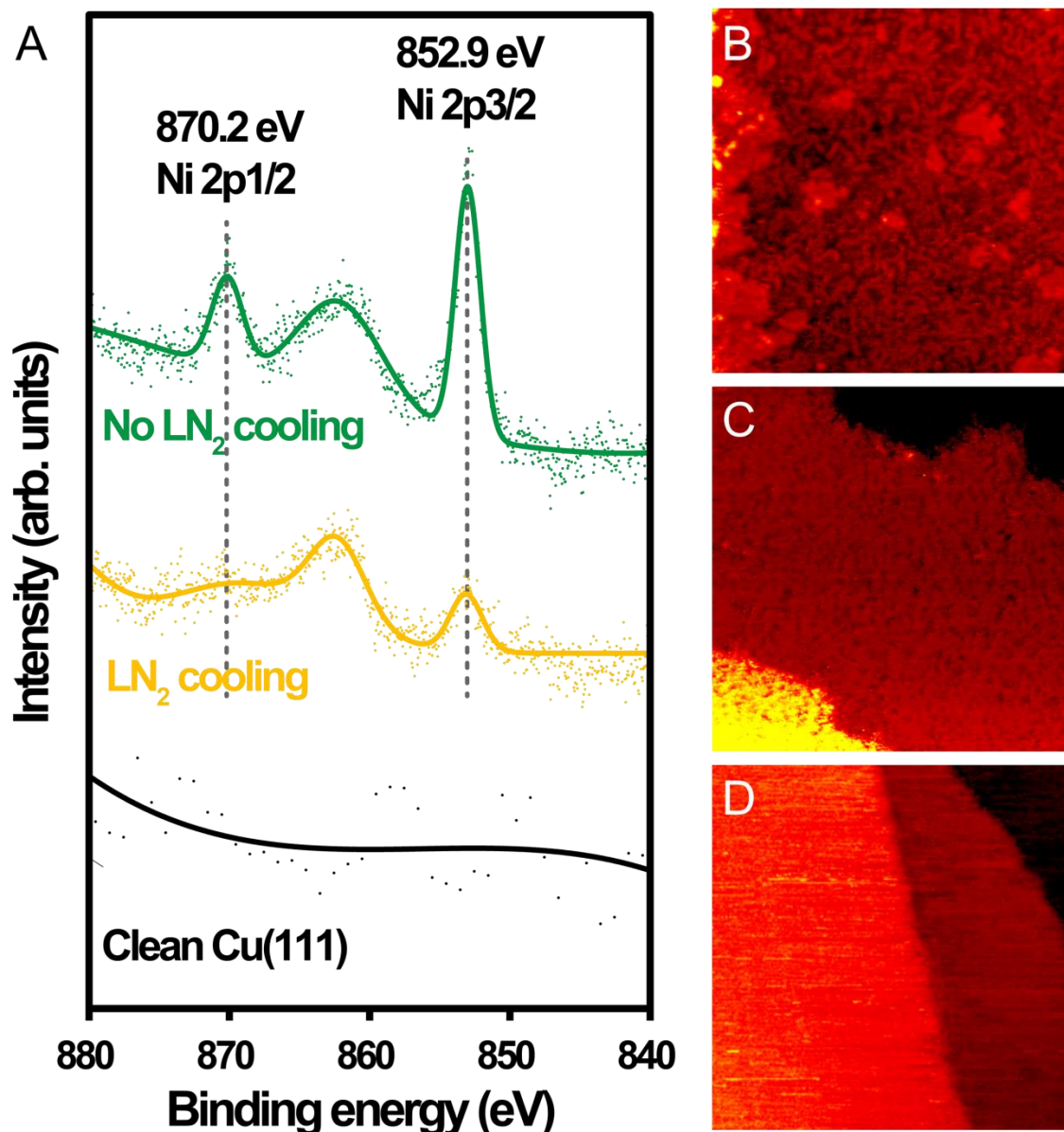
Figure 3.10 *Effect of nickel carbonyl impurity on Cu(111) during high pressure CO experiments. A) XPS spectra of clean Cu(111) surface (bottom) and the surface after being exposed by ambient pressures of CO filtered with liquid nitrogen trap to remove carbonyl impurities (middle) and without liquid nitrogen trap (top) at 300 K. The corresponding surfaces under UHV at 300 K are shown in D), C) and B) respectively. All images are 45×45 nm^2. I_t = 0.12~0.30 nA, V_t = 1.1~1.2 V.*

In short summary, the interaction between high pressure CO and Cu(111) at 300 K is complex. A complete interaction process is recorded by AP-STM with atomic resolution. CO adsorbs at a-top site on Cu(111) to form a hexagonal pattern with a spacing of 6.5 Å at high

pressures and desorbs upon evacuation. High pressure CO induces Cu(111) terraces to be roughened. The topographical changes on Cu(111) is irreversible after evacuation. Carbonyl impurities are easily attached with high pressure CO. By combining STM and XPS results, the dendritic growth from step edges and newly formed islands on terraces are assigned as carbonyl species. Hexagonal patterns of carbonyls with a spacing of 5.2 Å, 4.5 Å are observed.

3.3.2 Ambient pressures of O_2

At low pressures (less than 10^{-6} Torr) and 300 K, oxygen molecules adsorb on Cu(111) with a sticking coefficient of 10^{-3} and dissociate to two oxygen atoms with an apparent activation energy of 2~4 kcal/mol.[92] The dissociated oxygen atoms are chemisorbed on Cu(111) and are not very mobile. Figure 3.11A is a Cu(111) surface with a few defects circled in red. After the surface is exposed to 2×10^{-8} Torr O_2 at 300 K, chemisorbed oxygens appear as highlighted in blue circles, Figure 3.11B. The chemisorbed oxygens remain still within 1 min, Figure 3.11C. When Cu(111) is exposed to higher Langmuir (1 Langmuir = 1×10^{-6} Torr×s) of oxygen under similar conditions, a mixed copper oxides of Cu_2O-'5-7' and Cu_2O hexagonal rings appear on different locations: triangular shaped added oxide (CuO_{xA}) within the original Cu(111) surface and terrace oxide (CuO_{xT}) on top of the original Cu(111) surface, Figure 3.11D.[52] Thus, oxygen can move copper atoms during the dissociation and oxidation process. It's reasonable. Since Cu_2O-hex/5-7 ring structures have a lower copper density than that of Cu(111), one layer of Cu_2O-hex/5-7 cannot consume all of the surface copper within the same area. Because of different local density of states near Fermi level, terrace oxide, CuO_{xT}, is imaged to be lower than nearby Cu(111) which is on the same terrace, and added oxide, CuO_{xA}, is imaged to be about the same height with Cu(111) on a lower layer, Figure 3.11E.
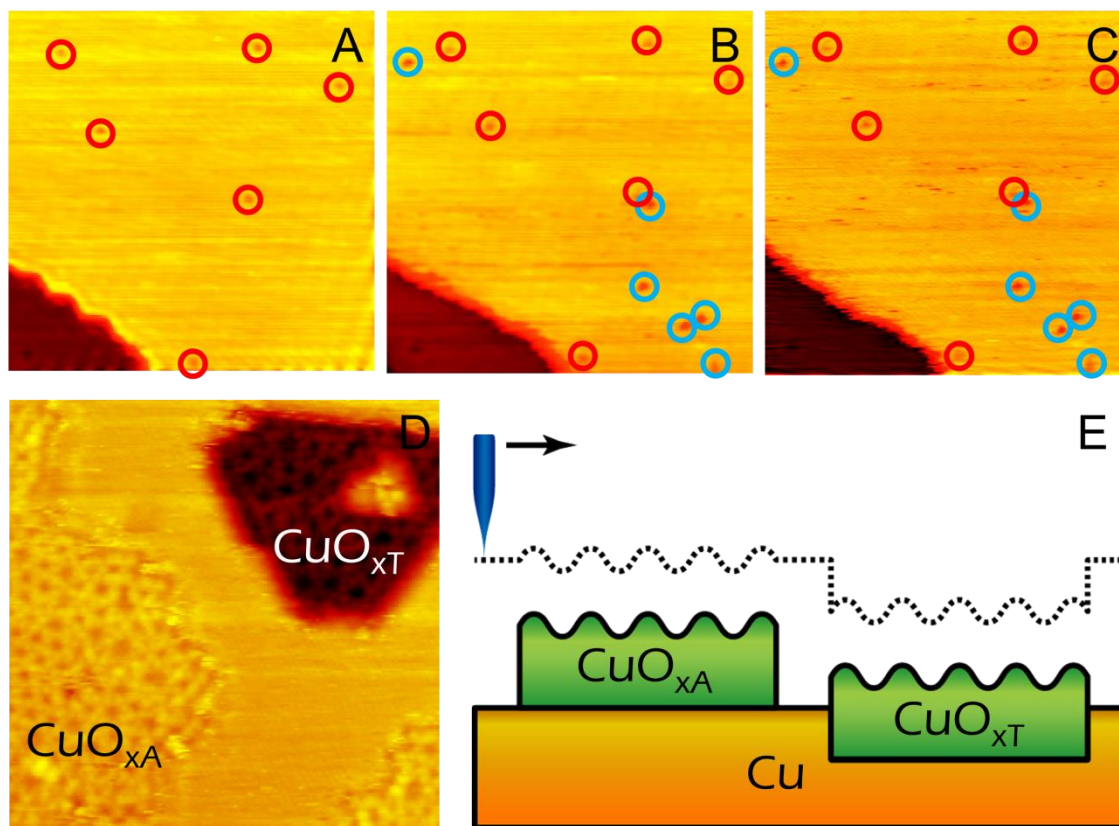
Figure 3.11 *10^{-8} Torr Oxygen adsorption on Cu(111) at 300 K. A) to C) are of the same area at a scale of 40×40 nm^2. $I_t = 0.44$ nA; $V_t = 1.20$ V. Red circles are land marks, and blue ones are dissociated oxygen atoms. The interval between B) and C) is 1 min. D) shows added oxide and terrace oxide after oxygen adsorption. Image is 12×12 nm^2. $I_t = 0.51$ nA; $V_t = 0.27$ V. E) is a schematic of STM line scan v.s. real space topography in D).*

Cu(111) is oxidized rapidly and dramatically at higher pressure of O_2 at 300 K, Figure 3.12. Figure 3.12A is an STM image of clean Cu(111) with two terraces. Once 10 mTorr is dosed on the surface at 300 K, the surface undergoes massive reconstruction, Figure 3.12B. The tungsten STM tip is a little unstable under O_2, which leads to blurry images. Surface is oxidized to a rigid structure within 3 min, and no large topographical change is observed afterwards, Figure 3.12D to 3.12F. The surface is greatly roughened to disordered structures, which rearrange to $Cu_2O/Cu(111)$ row structures upon further annealing.
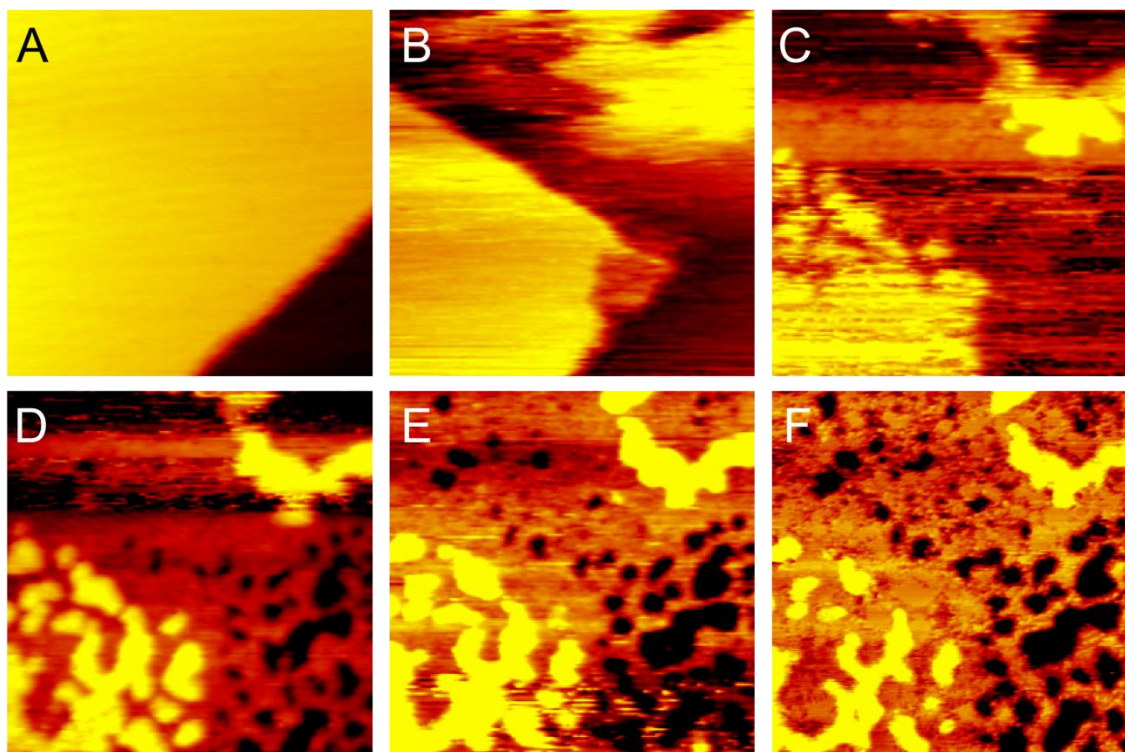
Figure 3.12 *In situ AP-STM images of Cu(111) under 10 mTorr O$_2$. From A) to F), the exposure time is 0 min, 0.9 min, 1.8 min, 2.6 min, 5.3 min, 8.8 min respectively. All images are 45×45 nm^2. I$_t$ = 0.41~0.47 nA; V$_t$ = 1.40 V.*

Thus, Cu(111) is very easy to be oxidized at 300 K, under both low and high pressures of O$_2$. As pressure increases, Cu(111) is oxidized to chemisorbed oxygen on Cu(111), ordered Cu$_2$O-hex/5-7 ring structure, and disordered copper oxide which can be annealed in UHV to make an ordered structure.

3.3.3 Adsorbate-driven morphological changes on Cu(111) nano-pits

A pitted-Cu(111) surface can be obtained after gentle sputtering of a smooth-Cu(111) surface at 300 K,. As sputter energy and current increase, Cu(111) gets rougher. After extended sputtering, the ion bombarded surfaces reach dynamic equilibrium with characteristic size, depth and density of nested pits.[4,6,7,93-96] For example, after sputtering clean Cu(111) by Ar$^+$ at 1.00 keV and 1.0 μA for 1 min, the Cu(111) surface is covered mainly with hexagonal nano-pits with

a diameter range from 8 to 38 nm, Figure 3.13A. Narrow (steep) steps of pits are generated, as shown in Figure 3.13B.
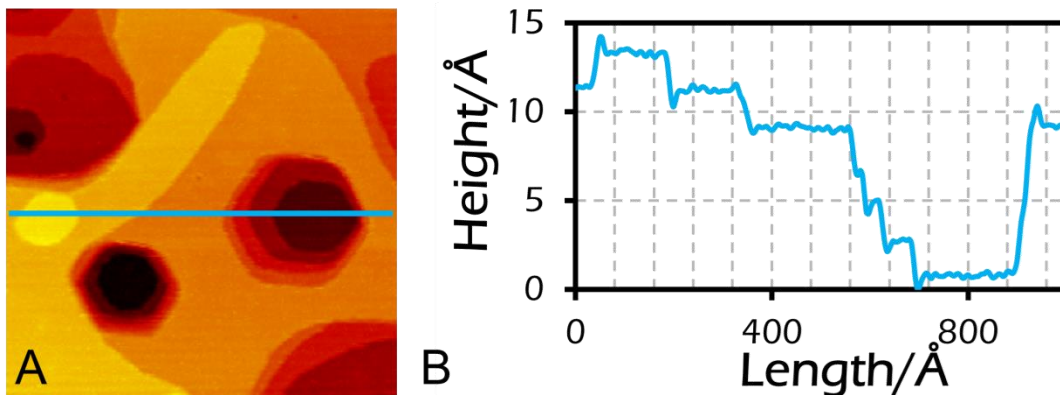
Figure 3.13 *Surface topography of pitted-Cu(111) under UHV conditions at 300K. (A) An STM image at 300 K. The blue line indicates a line scan. The image is 100×100 nm^2, $I_t = 0.67$ nA; $V_t = 1.63$ V. (B) A line scan corresponds to the blue line in (A).*

Similar morphology can be achieved on Au(111) by the same method. The pitted Au(111) can be smoothened by 0.75 Torr CO at 300 K because of the induced massive atomic movement.[97] Even at low CO pressures (10^{-9} Torr) below 180 K, weakly adsorbed CO caused irreversible morphological changes of the surface. The pitted Cu(111) surface is more stable than Au(111), since only mTorr scale CO can adsorb on pitted Cu(111).[59] A one layer deep shallow pitted Cu(111) is prepared by 30 s sputtering at ~360 K with 0.50 keV energy and 0.8 μA target current, Figure 3.14A. After 0.9 min exposure to 700 mTorr CO, in Figure 3.14B, the original hexagonal edges of the pits are rounded and decorated by CO as point depressions, similar to CO interacting with Au(111) nano pits. In addition, a triangular-shaped kink is also smoothened due to high pressure CO. The number of pits is maintained. Thus, ambient pressures of CO induce the small movement of under-coordinated copper atoms.
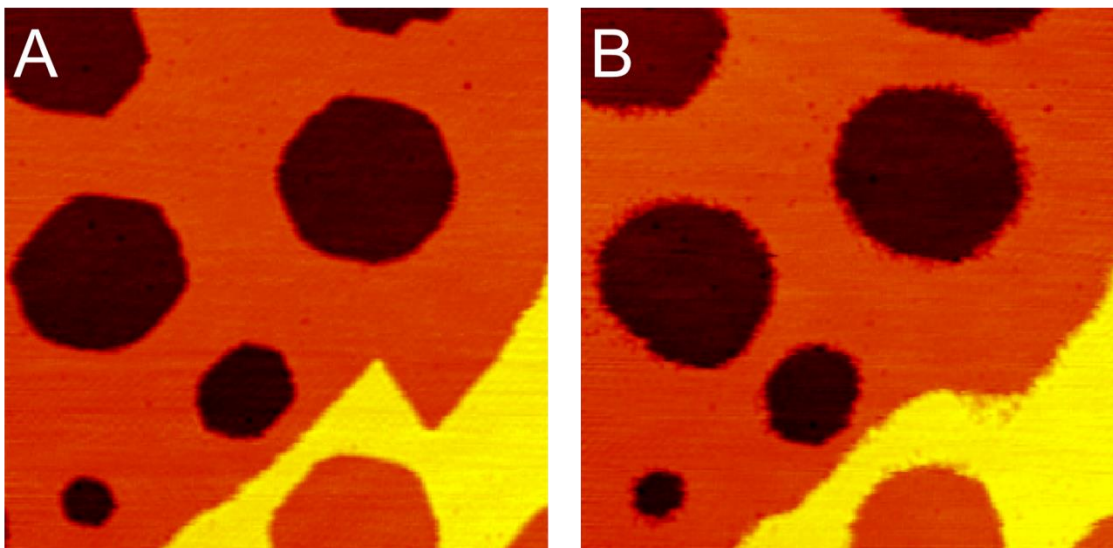
Figure 3.14 *In situ AP-STM images of pitted-Cu(111) at 300 K. (A) Pitted-Cu(111) surface with one layer deep shallow hexagonal pits, and (B) the same place as (A) but after 0.9 min exposure to 700 mTorr CO. Both images are 65×65 nm^2, I_t = 0.64~0.65 nA; V_t = 1.53 V.*

Both theory and experimental data indicate that molecular hydrogen dissociates on Cu(111) with a barrier of ~0.4 eV.[98-100] However, the dissociated hydrogens recombine and desorb from surface between 250 and 400 K.[98] At 300 K, atomic hydrogen on Cu(111) cannot be captured by an STM tip because of the extremely fast diffusion rate.[101,102] When a pitted Cu(111) is exposed to 1.5 Torr of H_2 at 300 K, no atomic hydrogen or obvious change of the structure is observed. In order to emphasize the role of atomic hydrogen, we decided to expose the nano-pitted Cu(111) directly to atomic hydrogen.

Figure 3.15 shows the process of healing the pitted-Cu(111) surface by atomic hydrogen. After gentle Ar$^+$ sputtering, a Cu(111) surface is shown with shallow hexagonal pits, Figure 3.15A. Most pits heal after 5 min exposure to 1×10^{-7} Torr atomic hydrogen at 300 K, Figure 9B. As previously discussed, atomic hydrogens are not imaged due to a high diffusion rate.[101] This trend continues with further exposure to atomic hydrogen until a smooth Cu(111) surface is achieved, Figure 3.15C to 3.15D. Although Cu(111) itself has mobility, similar to the self-

healing ability reported on Ag(111),[96] no massive healing of nano-pits is observed by scanning a similar pitted-Cu(111) surface under UHV at 300 K for ~4 hours. Thus, the healing effect observed in Figure 3.15 is mainly caused by atomic hydrogen.
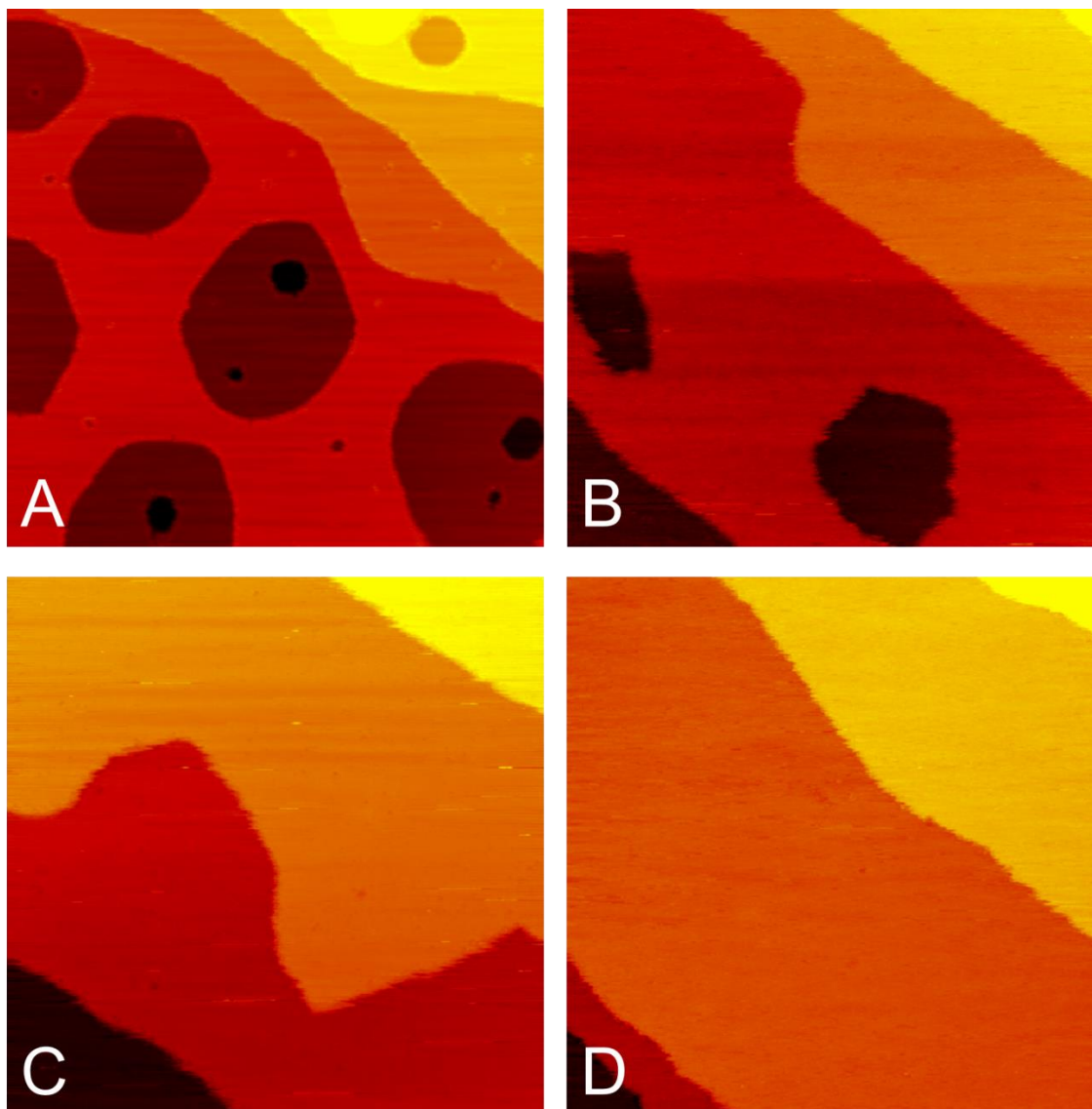
Figure 3.15 *Ex situ STM images of the pitted-Cu(111) surface under exposure of 1×10^{-7} Torr atomic hydrogen at 300 K. Exposure time from A) to D) is 0 min, 5 min, 10 min and 20 min, respectively. All of images are 100×100 nm^2, I_t = -0.53~0.53 nA; V_t = -0.83~1.36 V.*

Ambient pressure CO cannot heal Cu(111) pits at 300 K but atomic H can at a much lower pressure. The difference is because of different interaction mechanisms. CO binds weakly

at a-top positions, resulting in a slightly higher mobility of Cu atoms. Atomic H can diffuse into sub-surface and form copper hydride. During the recombination and desorption as H_2, Cu atoms are released and fully relax to long range smooth structure. It is supported by reference that absorption of atomic H on Cu(100) at low temperatures (below 200 K) leads to the formation of a metastable surface hydride, which induces the reconstruction to an approximated hexagonal cell.[103]

3.4 Summary

The interactions between Cu(111) surfaces and ambient pressures of a single type of gas (CO, O_2, H_2, and atomic H) at 300 K were systematically studied. The extend of topographical changes of Cu(111) due to ambient pressure gas exposure is: O_2> atomic H>CO> >H_2.

At 300 K, O_2 adsorbs on and oxidizes Cu(111), leading to a dramatic topographical change. CO cannot adsorb on Cu(111) until pressures in the mTorr range. High pressure of CO adsorbs at a-top positions and induces a shape change of one layer nano-pits on Cu(111). The adsorption process roughens Cu(111) surface, which cannot be completely released after desorption. Carbonyl is easily formed under high pressures of CO and is stabilized as islands on the surface under UHV at 300 K. Atomic H at low pressures (10^{-7} Torr) heals one layer deep nano-pits on Cu(111), because copper hydride is formed at sub-surface sites, and the copper atoms fully relax to a smooth Cu(111) surface during the H recombination and desorption process. Although molecular hydrogen can also dissociate on Cu(111), the dissociate hydrogen recombines and desorbs quickly without reacting with Cu and changing the pitted surface.

Chapter 4. In situ Imaging of $Cu_2O/Cu(111)$ under Reducing Conditions

4.1 Introduction

Carbon monoxide and hydrogen is ubiquitous in the chemical industry. H_2 is widely used as a reduction gas in the pretreatment process, where metal oxide is reduced or partially reduced. The pretreatment was reported to affect the catalytic activity and selectivity.[104,105] Both CO and H_2 helps metal/metal oxide catalysts to convert the NO_x in automotive exhaust gases.[106] Additionally, production and consumption of CO and H_2 are related to several important catalytic processes including those mentioned in section 1.2, where copper-based catalysts demonstrate good yields and much lower costs than comparable noble-metal catalysts.[107-113] There is consequently much interest in the fundamental understanding of the interaction between CO/H_2 and the surfaces of copper and copper oxide catalysts.

In this chapter, a monolayer Cu_2O film on Cu(111) serves as a model catalyst for the atomic/near atomic scale surface studies. $Cu_2O/Cu(111)$ has well known '44' and '29' row structures, which are composed of distorted six-membered Cu_2O rings.[51,52] It is reported under UHV and high temperature conditions, $Cu_2O/Cu(111)$ is reduced by CO and transforms to intermediate species of Cu_2O-hex/5-7 ring structures, before it is ultimately reduced to metallic

copper.[54,56] Only one or two phases exist at each stage of the reduction process.[54] Mars-van Krevelen mechanism has been proposed metal oxides reduction by CO: CO reacts with oxygen on surface and produces CO_2.[114,115]

Oxygen vacancies, which are inevitable defects on the as-prepared surface in UHV, have been known as most common active sites due to their ability to lower the energy barrier for dissociating H_2.[116] Other surface defects, such as under-coordinated step edges and impurities from the single crystal, may also serve as active sites. It is known that hydrogen uptake is really difficult on copper oxide at 300 K.[117,118] H_2 adsorption and dissociation on Cu_2O at pressures below ~10^{-5} Torr and at low temperatures is slow, leading to an induction period for the reaction.[119,120] Theory even predicts that H_2 is not able to react with $Cu_2O(111)$.[121] However, H_2 can adsorb and dissociate on $RuO_2(110)$ 273 K.[122] In addition to hydroxyl group formation, an *in situ* STM study of the reduction of a Rh(111) surface oxide by H_2 at room temperature revealed that H_2 only absorbs on reduced areas which then promote further reduction.[123] The rate determining step for the reduction of most metal oxide surfaces is thought to be the water formation,[124] which generally needs hydroxyl groups and dissociated hydrogen atoms. In order to observe reaction under reasonable conditions, atomic hydrogen, which is more active than molecular hydrogen, is widely used for surface chemistry studies. When 200 L of atomic hydrogen was dosed on the $Cu_2O(110)$ surface at room temperature, molecular hydrogen, hydroxyl groups, and copper hydride were all observed.[125] *Ex situ* studies have shown the ability of atomic hydrogen to form hydroxyl groups on other metal oxide model catalysts such as FeO/Pt(111).[126]

In this chapter, a complete discuss of the reduction of $Cu_2O/Cu(111)$ by ambient pressures of CO and H_2, is presented employing AP techniques of STM, XPS, and IRRAS. Reaction sites and intermediates are identified. Kinetic information is measured.

4.2 Experimental Methods

The Cu(111) single crystal (Princeton Scientific Corp.) was cleaned by consecutive sputter (20 min, Ar^+) annealing (10 min, 800 K) cycles. The Cu(111) was oxidized to form a monolayer thin film of $Cu_2O/Cu(111)$ by exposing to 5.0×10^{-7} Torr O_2 for 30 min at $550 - 650$ K. In situ ambient pressure STM studies were carried out in a commercial SPECS Aarhus 150 NAP STM chamber equipped with a high pressure cell containing the STM head. CO and H_2 were purified using a liquid nitrogen trap and trapped in a six way cross prior to introduction to the high pressure cell. The $Cu_2O/Cu(111)$ was reduced at 700 K in 5×10^{-5} Torr H_2 and then cooled down under UHV for the XPS measurements at a photon energy of 615 eV. A custom-made UHV chamber with a multi-channel hemispherical analyzer (VSW EA125) was used for XPS experiments at beamlines U12A, National Synchrotron Light Source, Brookhaven National Laboratory. Ambient pressure $Cu_2O/Cu(111)$ reduction by CO or H_2 at various temperatures was conducted in a high pressure chamber equipped with infrared reflection absorption spectroscopy (IRRAS). The measurement chamber could be isolated from a sample preparation chamber which is under UHV conditions. Spectra were collected at an incident angle of 85 °to the surface normal and referred to background spectra collected prior to reduction.[81]

4.3 Results and Discussion

4.3.1 Cu$_2$O/Cu(111) reduction by ambient pressures of CO

Cu$_2$O/Cu(111) reduction by ambient pressures of CO is confirmed by IRRAS. Under UHV conditions at 120 K, CO adsorption peak on Cu$_2$O/Cu(111) is at ~2097 cm^{-1},[127] and on smooth Cu(111) is at ~2070 cm^{-1}.[59,128] Both adsorptions are very weak and have a desorption temperature at ~180 K and ~160 K respectively.[127] Similar with pressure dependent CO adsorption on Cu(111) (chapter 3), ambient pressure can also promote CO adsorb on Cu$_2$O/Cu(111). Figure 4.1 shows Cu$_2$O/Cu(111) exposure to CO pressure continuously from 1.7 mTorr to 266.0 mTorr. Under ambient pressure conditions, a gas phase CO peak is observed around 2143 cm^{-1}. Additionally, starting from 4.8 mTorr CO adsorption peak on Cu$_2$O(111)/Cu(111)[127] grows at 2094 cm^{-1} as pressure increases to 10 mTorr. A series of IR spectra (from top to bottom) was collected within 10 min. The reduction gradually progresses as the disappearance of well-ordered Cu$_2$O/Cu(111) structure (CO adsorption peak at 2094 cm^{-1}) and appearance of less oxidized Cu$_2$O-hex/5-7 structure (CO adsorption peak at ~2105 cm^{-1}).[127] Both features are very weak under 10 mTorr CO. The even weaker adsorption of CO on Cu(111) is invisible at 10 mTorr. After increasing CO pressure to 80.0 and 266.0 mTorr, CO adsorption peaks on Cu$_2$O-hex/5-7 structure and Cu(111) are clearly observed. AP-IRRAS experiments confirm that CO adsorbs on and reduces Cu$_2$O/Cu(111) at 300 K and pressures above 10 mTorr.
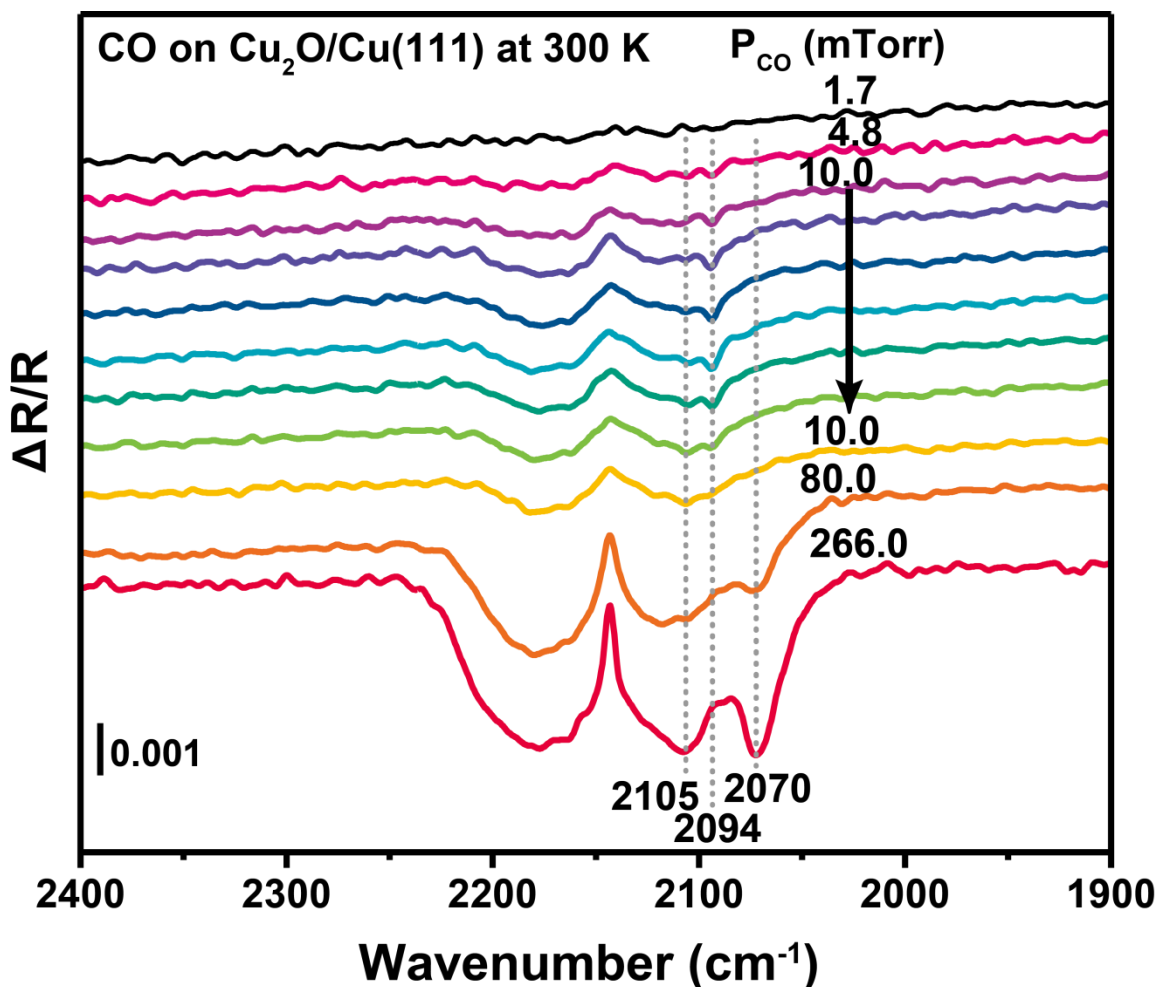
Figure 4.1 *Spectra obtained by IRRAS of Cu₂O/Cu(111) reduction by CO at the specified pressures. A series of IR spectra (indicated by a black arrow) were collected at 10 mTorr CO with a total exposure time of 10 min, showing the reduction of the Cu₂O(111)/Cu(111).*

Cu₂O/Cu(111) reduction by 10 mTorr CO was further investigated by AP-STM at 300 K. According to Chapter 3, no reconstruction of Cu(111) is induced by CO under the same condition. The reduction from the Cu₂O/Cu(111) row structure to the Cu₂O-hex/5-7 ring structure to metallic Cu is seen in the consecutive STM images in Figure 4.2. An as-prepared Cu₂O/Cu(111) surface with three terraces is shown in Figure 4.2A. Within 4 min of reduction, metallic Cu starts to grow from step edge, Figure 4.2B. Because of the electronic effect discussed in chapter 3.3.2, the initial growth of metallic Cu is along descending direction from step edges.

An intermediate band of Cu_2O-hex/5-7 exists between Cu_2O and Cu, showing a metal/oxide phase separation. As the surface is further reduced from Figure 4.2C to 4.2E, Cu grows in both descending and ascending directions along with a loss of Cu_2O/Cu(111) rows. The lowest terrace is gradually overgrown by the growth of Cu from middle terrace, showing mass transfer of Cu front. It is reported that CO facilitates sintering of atoms to small metallic particles on metal or oxide substrates by mass transport.[80,129-131] We thus propose that the released Cu atoms from Cu_2O reduction are highly mobile under 10 mTorr CO at 300 K. These Cu atoms can rapidly diffuse and join nearby Cu region, resulting in Cu growth.
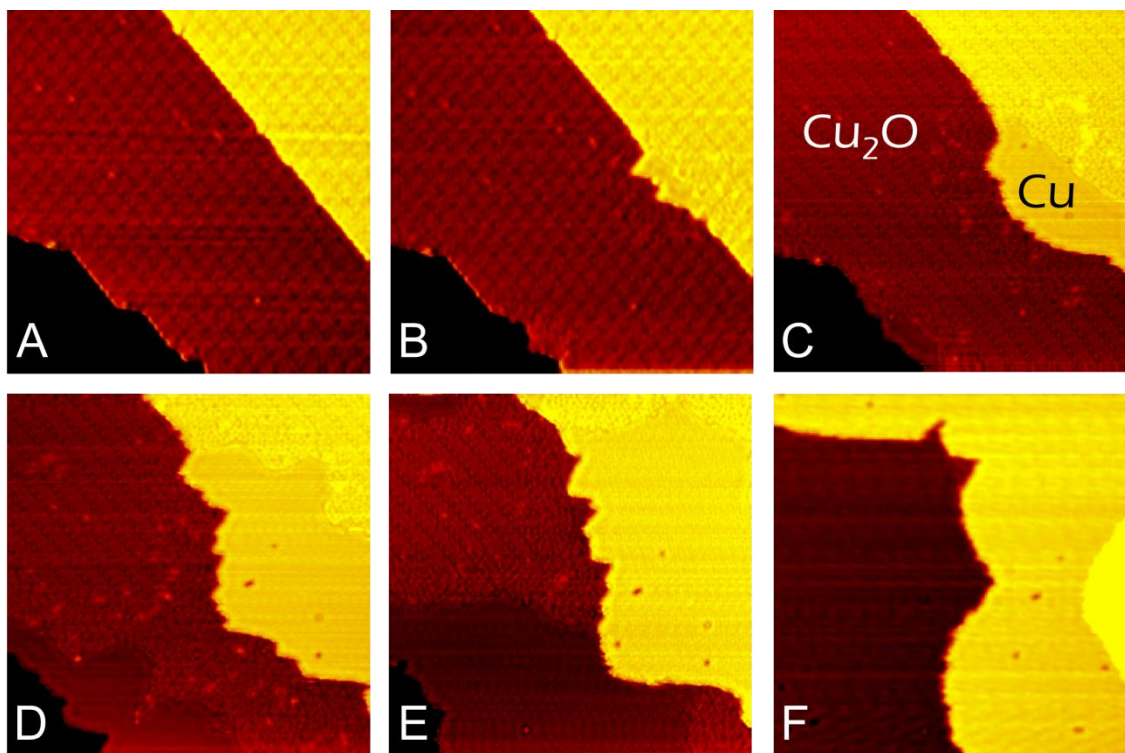
Figure 4.2 *In situ AP-STM images of Cu_2O/Cu(111) reduction by 10 mTorr CO at 300 K. The same area is scanned continuously from A) to F) with the exposure time of 0 min, 4 min, 6 min, 10 min, 12 min, and 16 min. All images are 35×35 nm^2. $I_t = 0.72 \sim 0.94$ nA; $V_t = 1.09$ V.*

The density of Cu in the three Cu-based structures decreases in a sequence of close packed Cu(111) > row structure Cu_2O/Cu(111) > Cu_2O-hex/5-7. Thus, a smaller occupied

surface area is expected after fully reduction of one layer $Cu_2O/Cu(111)$. The reasons for no area loss in Figure 4.2 are: 1) the expansion from row structure $Cu_2O/Cu(111)$ to Cu_2O-hex/5-7 compensates the contraction from $Cu_2O/Cu(111)$ to close packed $Cu(111)$. 2) Under ambient pressures of CO, Cu atoms from other areas rapidly diffuse and join the metallic fronts in Figure 4.2, resulting in an area loss outside Figure 4.2.

Defect sites on $Cu_2O/Cu(111)$ terraces can also be the initial reduction sites, as observed in another AP-STM experiment with a slightly higher pressure of 45 mTorr CO at 300 K. The ordered $Cu_2O/Cu(111)$ in Figure 4.3A starts to disappear from the right lower corner in Figure 4.3B. A clear transformation of six-membered Cu_2O ring structure in Figure 4.3C to pentagonal Cu_2O ring in Figure 4.3D is observed in the intermediate region. Cu_2O-hex/5-7 covers major surface and metallic Cu forms in the highlighted dotted green lines in Figure 4.3D. The Cu island forms on the defect sites on the as-prepared Cu_2O terrace in Figure 4.3A).

A new intermediate appear in Figure 4.3D, showing as protrusions in near-squared pattern. This feature is proposed to be the intermediate structure as $Cu_2O/Cu(111)$ transfers to Cu_2O-hex'5-7. Adsorbed CO molecule on $Cu_2O/Cu(111)$ is not proposed because 1) the short residence time of CO_{ad} on $Cu_2O/Cu(111)$ at 300 K making it highly unlikely to be imaged, and 2) CO_{ad} on $Cu_2O/Cu(111)$ is expected to adopt hexagonal pattern, the structure of the substrate. In order to monitor the structural change of the near squared feature, a schematic frame is superimposed on top of $Cu_2O/Cu(111)$ structure in the same position in Figure 4.3A) and D). Here, blue balls stand for oxygen atoms and yellow balls stand for copper atoms. The chemisorbed oxygen in each ring center is not drawn. It is obvious now that the near-squared feature in Figure 4.3D) corresponds to vertices of the $Cu_2O/Cu(111)$ ring structures, indicating the buckling of copper oxide.
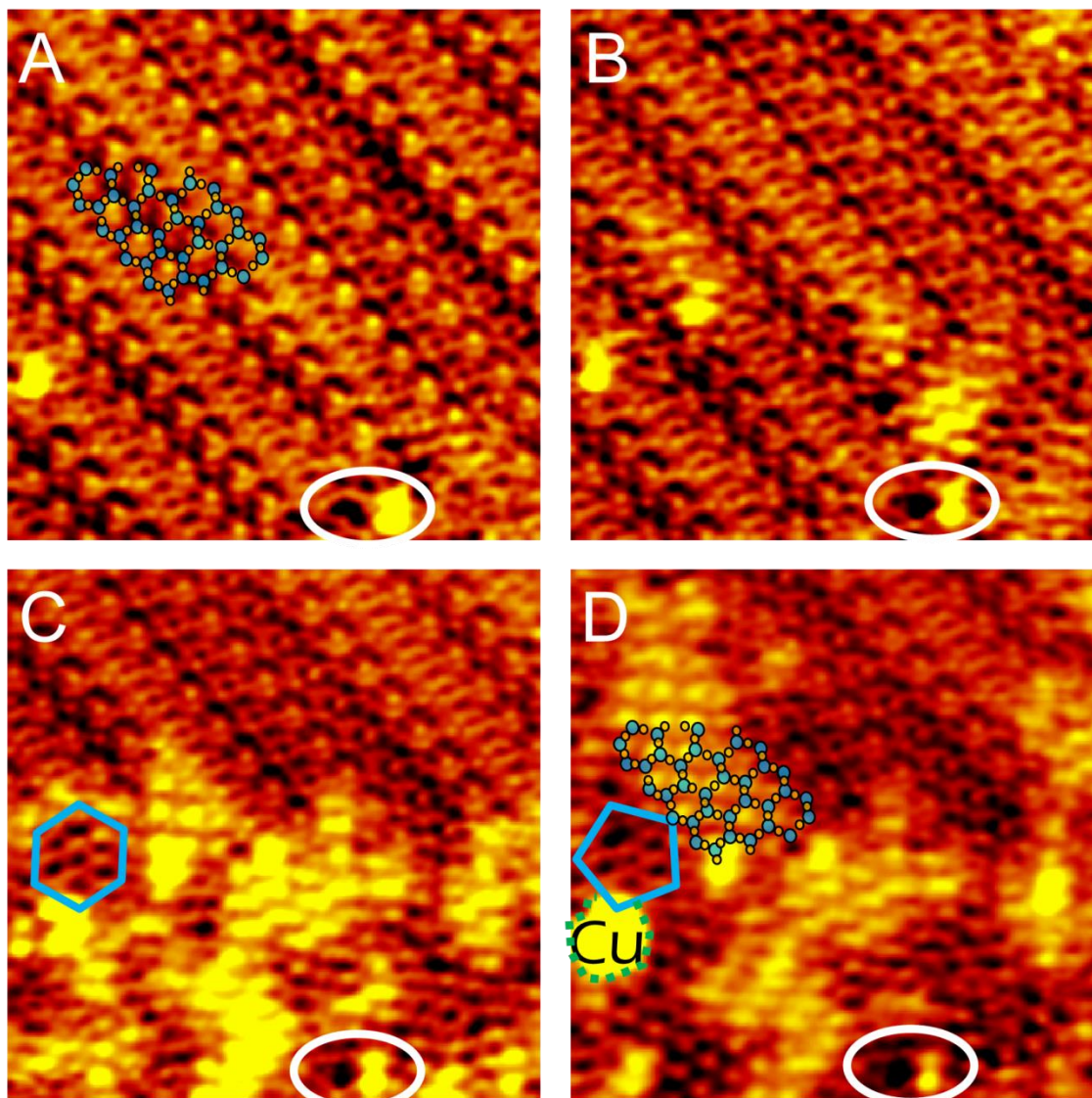
Figure 4.3 *Consecutive AP-STM images of $Cu_2O/Cu(111)$ under 45 mTorr CO at 300 K. The exposure time from A) to D) is 0 min, 1 min, 3 min, and 5 min. All images are 11×11 nm^2. $I_t =$ 0.81~0.83 nA; $V_t = 0.91$ V. White circle highlights a landmark. The center hexagonal and pentagonal Cu_2O ring structures are highlighted in blue. A metallic Cu island is circled in a green dotted line in D). A schematic arrangement of $Cu_2O/Cu(111)$ is shown in both A) and D) at the same position. Blue balls are oxygen atoms, and yellow balls are copper atoms.*

In a short summary, the reduction process of $Cu_2O/Cu(111)$ by a CO pressure larger than 10 mTorr is studied by AP-IRRAS and AP-STM. CO molecule adsorbs on and reduces $Cu_2O/Cu(111)$ to intermediates composed of Cu_2O-hex/5-7 and finally metallic Cu. During the reduction, the three phases segregate and co-exist on the surface. Both step edges and defects on

58

terraces are initial active sites. The terrace oxide buckles before transfers to the intermediate structure. The released Cu atoms diffuse rapidly and join nearby Cu region, resulting in a front growth by mass transfer. Topography changes before and after the reduction.

4.3.2 Cu₂O/Cu(111) reduction by ambient pressures of H₂
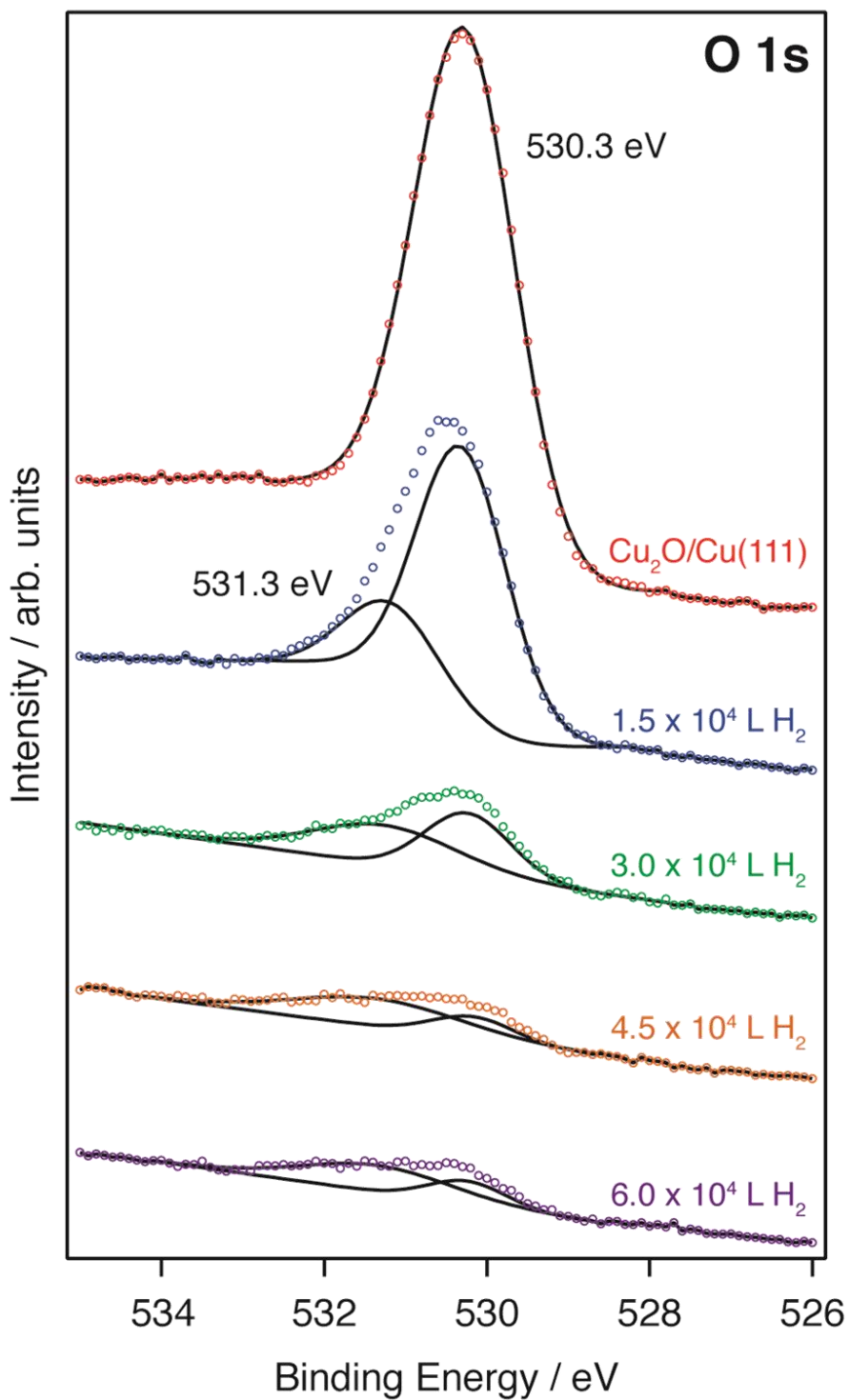
Figure 4.4 O 1s XPS spectra demonstrating the progressive reduction of Cu₂O/Cu(111) after exposure to 5 × 10⁻⁵ Torr H₂ at 700 K. Spectra acquired at 300 K in UHV. (hv = 615 eV)

The evolution of the O 1s XPS spectrum of the $Cu_2O/Cu(111)$ system during reduction by 5×10^{-5} Torr H_2 at 700 K is displayed in Figure 4.4. The spectra were obtained step-wise by exposing to sequential 1.5×10^4 L doses of H_2 at 700 K followed by cooling down to 300 K in UHV for data collection. The peak at 530.3 eV is assigned to the lattice oxygen of the Cu_2O layer (top spectrum in Figure 4.4).[50] As the H_2 exposure is increased (going from top to bottom spectra in Figure 4.4), the $Cu_2O/Cu(111)$ is progressively reduced, evidenced by the decreasing intensity of the Cu_2O peak at 530.3 eV. In addition to this, a shoulder at higher binding energy (531.3 eV) appears, which is attributed to the formation of hydroxyl groups (OH) at the surface.[43] The intensity of this shoulder decreases as the reduction reaction proceeds, indicating that hydroxyls are initially formed in large quantities and then are removed by further reaction with H_2, presumably via desorption from the surface as water. After a total exposure of 6×10^4 L of H_2 (purple spectrum in Figure 4.4) there remains only a small amount of oxygen at the surface, suggesting near complete reduction of the Cu_2O layer.

The low pressure high temperature XPS study convinces the formation of hydroxyl groups during $Cu_2O/Cu(111)$ reduction by H_2. The $Cu_2O/Cu(111)$ reduction by high pressure H_2 was further investigated at 300 K. A series of in situ STM images of the reduction under 1.64 Torr H_2 is shown in Figure 4.5. Four terraces of Cu_2O-'44' are visible in Figure 4.5A and colored yellow-red, aqua, blue and green-black respectively (see line profile in Figure 4.5J). After a relatively long induction period (~ 2 hours) of exposure to H_2 some small changes are observed on the surface occurring both at step edges and defects on the terraces (white arrows in Figure 4.5B). Upon further H_2 exposure, more significant reduction appears to initiate preferentially at the step edges as shown by the growth of the blue and green-black Cu terraces in Figure 4.5C. Metallic Cu forms first along the step edges, similar to what is observed in $Cu_2O/Cu(111)$

reduction by 10 mTorr CO in Figure 4.2B. The retreat of the Cu_2O and movement of metallic Cu

fronts towards the descending step edges indicate that the highly mobile Cu atoms released from

the reduction of the Cu_2O diffuse across the terrace and join nearby Cu step edges. Faceted step

edges are not observed due to the rapid reaction rate. The reduction continues from Figure 4.5D

to 4.5G. At each stage a clear intermediate band presents. A 'fuzzy' Cu step edge with streaking

along the fast scan direction (horizontal) is observed in Figure 4.5D which is consistent with the

high mobility of metallic copper at 300 K. By the latter stages of the reduction process (Figure

4.5H) there is only a small region of intermediate CuO_x remaining, which is rapidly reduced to

metallic Cu until the surface is completely Cu(111). (Figure 4.5I) The line profile obtained from

Figure 4.5I (shown in Figure 4.5K) shows that there is a double step between the red and blue

terraces, as at the start of the reduction reaction (shown in Figure 4.5J). The release of Cu

resulting in an increase of the width of the blue terrace has moved the green-black terrace out of

the STM images by the end of the reaction.
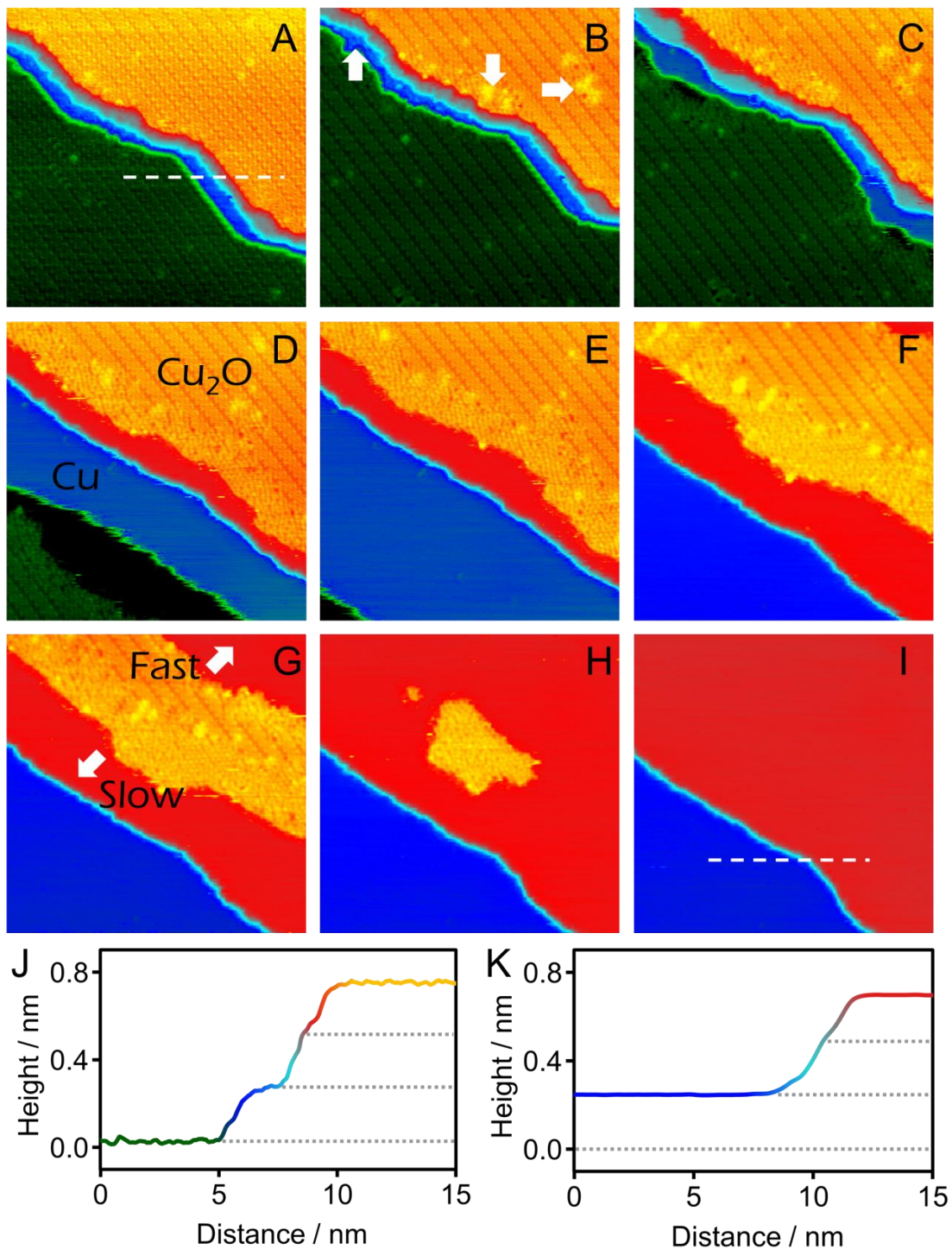
Figure 4.5 *In situ STM images of the Cu₂O/Cu(111) reduction under 1.64 Torr H₂ at 300 K. White arrows in B) highlight some initial reactive sites. The relative reaction speeds in opposite directions are indicated in G). The exposure times are: A) 0.16 h; B) 2.33 h; C) 3.04 h; D) 3.64 h; E) 4.49 h; F) 8.23 h; G) 8.68 h; H) 9.21 h; and I) 9.66 h. The line scans in (J) and (K) correspond to the white dashed lines in (A) and (I) respectively. All images are 32×32 nm². $I_t = 0.50{\sim}0.64$ nA; $V_t = 0.65$ V.*

63

Comparing the images in Figure 4.5F and 4.5G, two distinct speeds of reduction in opposing directions are observed. In both the fast and slow reduction directions, there is an interface between the $Cu_2O/Cu(111)$ row structure and the metallic Cu consisting of a band of partially oxidized CuO_x, however this band is much larger in the slow direction. The main difference between the fast and slow directions is the presence of a descending Cu step edge on the slow reaction side and an ascending Cu step edge on the fast reaction side. Taking into account the high mobility of metallic copper and its ability to dissociate molecular hydrogen,[83,100] we therefore propose that ascending step edges serve as a source of mobile, under-coordinated Cu atoms which are able to rapidly dissociate molecular hydrogen. The dissociated atomic hydrogen then reacts with hydroxyl species present in the intermediate CuO_x band to form water, which desorbs easily at 300 K.[83] The lower concentration of free under-coordinated Cu atoms in the region near descending step edges results in poorer dissociation of H_2 and therefore an overall slower reaction rate in this direction.

An atomically resolved STM image clearly shows the structure of the intermediate band during $Cu_2O/Cu(111)$ reduction by 1.54 Torr H_2, Figure 4.6. Between the Cu_2O row structure and the reduced Cu area, an intermediate band of hexagonal patterns and defects is observed. The spacing in the close packed hexagonal patterns is 6 ± 0.1 Å, which is the same spacing of relaxed Cu_2O hexagonal ring structures. The Cu_2O-'5-7' structure also exists in the intermediate area. Both structures are highlighted in white.
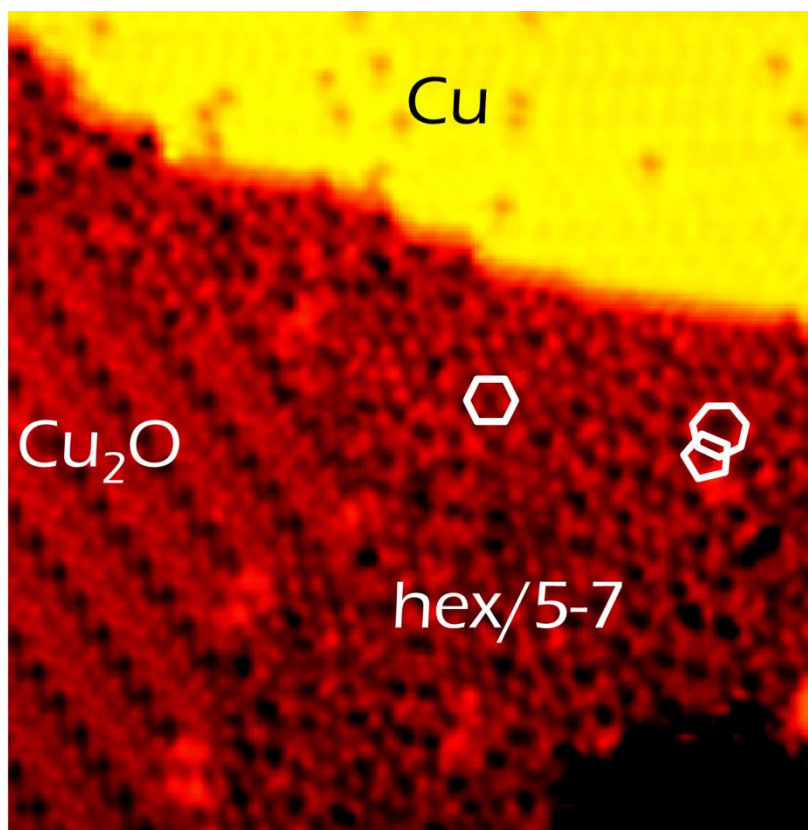
Figure 4.6 *In situ STM image of $Cu_2O/Cu(111)$ surface after exposure to 1.54 Torr H_2 for 23.4 h at 300 K. Cu_2O-'5-7' and hexagonal rings are highlighted in white. The image is 20×20 nm^2. I_t = 0.52 nA; V_t = 0.63 V.*

Another $Cu_2O/Cu(111)$ reduction experiment was carried out with a lightly lower H_2 pressure at 1.54 Torr. Figure 4.7A shows the well-ordered row structure of a Cu_2O monolayer film supported on Cu(111) with one step edge. After exposure to 1.54 Torr H_2 for 5.1 h, a few minor changes induced by the tip interacting with adsorbates on the surface are observed but there is no evidence of any Cu formation, indicating a long induction period for the reduction process, Figure 4.7B. The surface demonstrates some degree of mobility with the appearance of new defects (blue arrows) and disappearance of others (green arrows). White circles around a pair of fixed defects in Figure 4.7B and 4.7C serve as landmarks, confirming that these two images are of the same area. The reduction begins at around an exposure of 21.0 h, Figure 4.7C, when some of the Cu_2O is observed to have been partially reduced to Cu (a smooth bright yellow

terrace). The Cu terrace forms along the <110> close packed direction, shown as a green line in Figure 4.7C. Once a Cu region is formed, the reaction moves into a fast speed region, Figure 4.7D to 4.7G (images at ~1h intervals). Similar to what is observed in Figure 4.5, an intermediate band is observed. The fronts of the Cu area move in a mass transfer manner. Under H_2, copper atoms diffuse rapidly on surface, Figure 4.7H and 4.7I. By the end of the reduction process, Cu_2O terraces were reduced to metallic Cu with no noticeable Cu island formation.

An immobile bright feature is observed in the intermediate band, Figure 4.7C to 4.7F. It may be related to 1) Cu_2O-hex/5-7 structure, 2) hydroxyl species on Cu_2O-hex/5-7, and 3) water on Cu_2O-hex/5-7. According to Figure 4.6, the intermediate band is composed of Cu_2O-hex/5-7. Depending on tip conditions, Cu_2O-hex/5-7 structure can be imaged as protrusions with an apparent height higher than metallic Cu in the vicinity, Figure 4.8. The apparent height difference between the two is 0.4±0.1 Å, similar to 0.5±0.1 Å, which is the observed height difference between the bright feature and nearby Cu in the intermediate band. On the other hand, hydroxyls are also reported to be imaged by empty states STM as protrusions on a variety of metal oxides.[122,126] The high desorption temperature for OH from Cu_2O[119] also makes the observation in Figure 4 reasonable. Finally, water desorption from copper oxide is reported in the range from 200 K to 500 K.[132,133] It is therefore possible that some residual water is on the surface under the reaction conditions. At this moment, no specific conclusions can be reached on the identification of the bright feature.
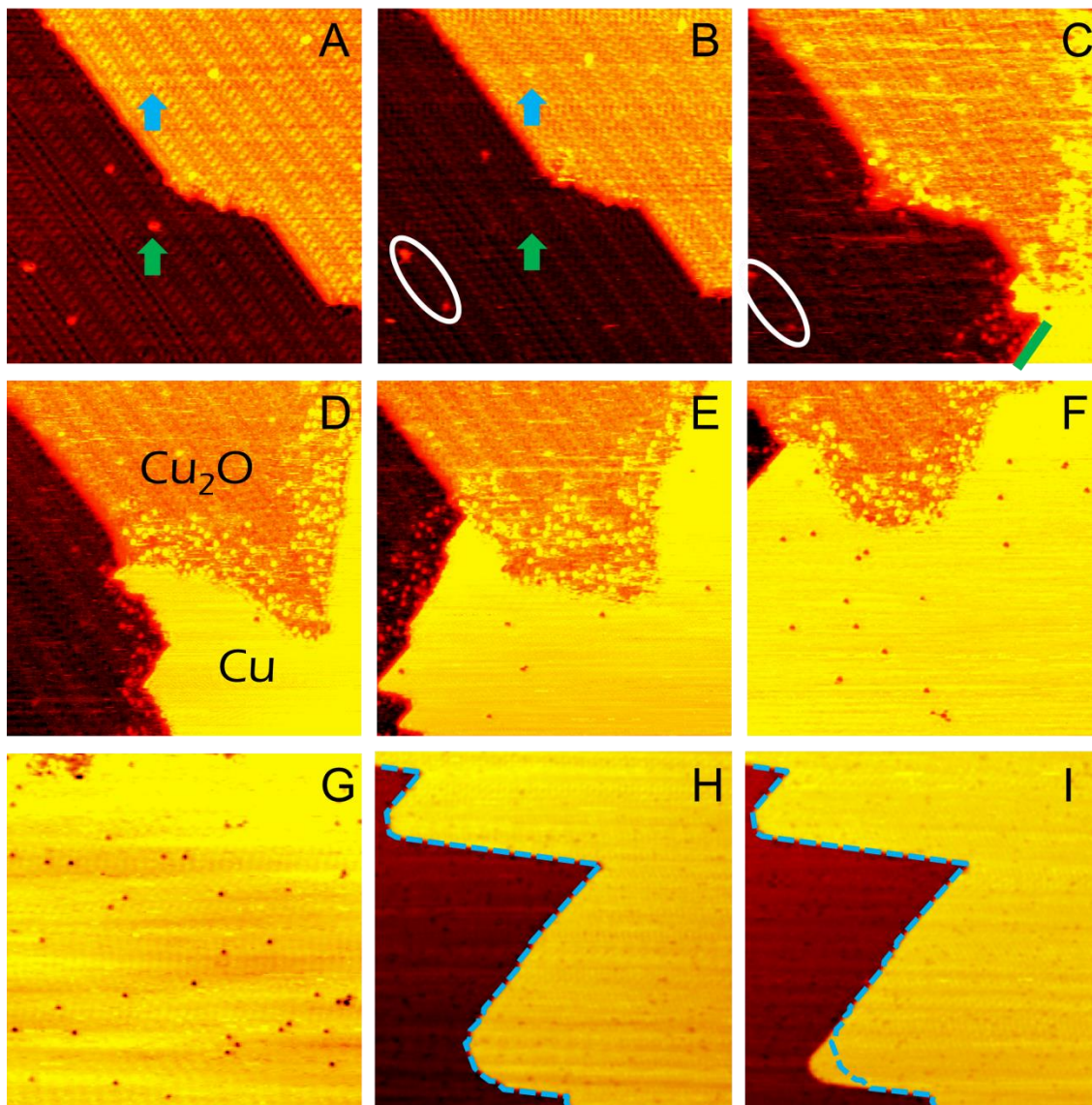
Figure 4.7 *In situ AP-STM images (A to G: 32 × 32 nm², H and I: 65 × 65 nm²) of the reduction of $Cu_2O/Cu(111)$ by 1.54 Torr H_2 at room temperature. H_2 exposure times are: A) 0.0 h; B) 5.1 h; C) 21.0 h; D) 22.0 h; E) 23.0 h; F) 24.0 h; G) 24.8 h; H) 28.29 h, and I) 28.34 h. Images from A) to G) are of the same area. A landmark is circled in white in B) and C). <110> direction is shown by a green line in C). H) and I) are of the same area. Blue dashed lines show the position of the step edge in H). I_t = 0.45~0.70 nA; V_t = 0.86~1.06 V.*
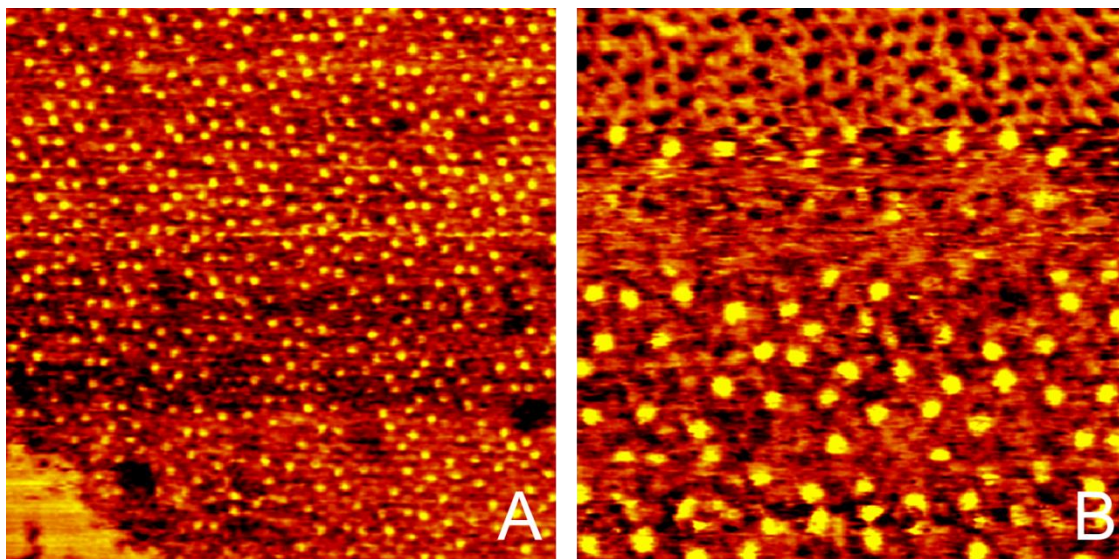
Figure 4.8 *STM image of Cu$_2$O-hex/5-7 structure under UHV at 300 K. A) is 25×25 nm^2; B) is 12×12 nm^2. I$_t$ = 0.39~0.42 nA; V$_t$ = 0.67~0.71 V. Image A) shows the bright feature is imaged higher than metallic Cu in the vicinity. B) shows Cu$_2$O-hex/5-7 can be imaged either as bright feature or dark feature.*

As the region of metallic Cu expands (Figure 4.7D to 4.7G), an increasing number of point depressions are observed on the metallic Cu terrace. These depressions are highly mobile at room temperature under an ambient pressure of hydrogen as well as UHV conditions. They are unlikely to be atomic hydrogen, molecular hydrogen or copper hydride, since atomic/molecular hydrogen diffuses too fast on Cu terraces at room temperature to be captured in STM.[101] Although chemisorbed oxygen atoms have a similar dark appearance on the Cu(111) surface, they are immobile at room temperature, Figure 3.10. An in situ STM study of reducing a Rh(111) surface oxide by 10^{-7} mbar H$_2$ shows point depressions on the metallic Rh surface. The depressions are assigned as Rh vacancies due to the different Rh density between oxide and metal.[123] However, the high mobility of copper atoms at room temperature makes the missing atom theory unconvincing. Hydroxyl groups can be imaged as depressions on metallic copper,[134,135] and they're also confirmed as intermediates by XPS (Figure 4.4). At 300 K under

UHV conditions, water is not observed on the Cu(111) surface and hydroxyl species desorb from Cu(111) between 250 to 300 K.[83] Thus, we propose that the mobile dark point defects observed on the Cu terraces in Figure 4.7 are most likely remaining hydroxyl species.

In Figure 4.9, a schematic is drawn to illustrate $Cu_2O/Cu(111)$ reduction process by H_2 at 300 K. After reaction is initiated on step edges, an intermediate band of Cu_2O-hex/5-7 forms between $Cu_2O/Cu(111)$ and Cu regions, and hydroxyl species also forms on the surface, Figure 4.9A. In Figure 4.9B, a very small portion of high mobile under-coordinated copper atoms diffuse back and forth on copper terrace from and to step edges. H_2 dissociates on the rapidly diffusing under-coordinated copper atoms, and the dissociated hydrogen reacts with oxide to form hydroxyl species or react with surface hydroxyl species to form water. The released copper atoms join the nearby Cu region. As reduction proceeds, metallic copper grows in the descending step edge direction and copper oxide on the descending terrace is consumed, Figure 4.9C.
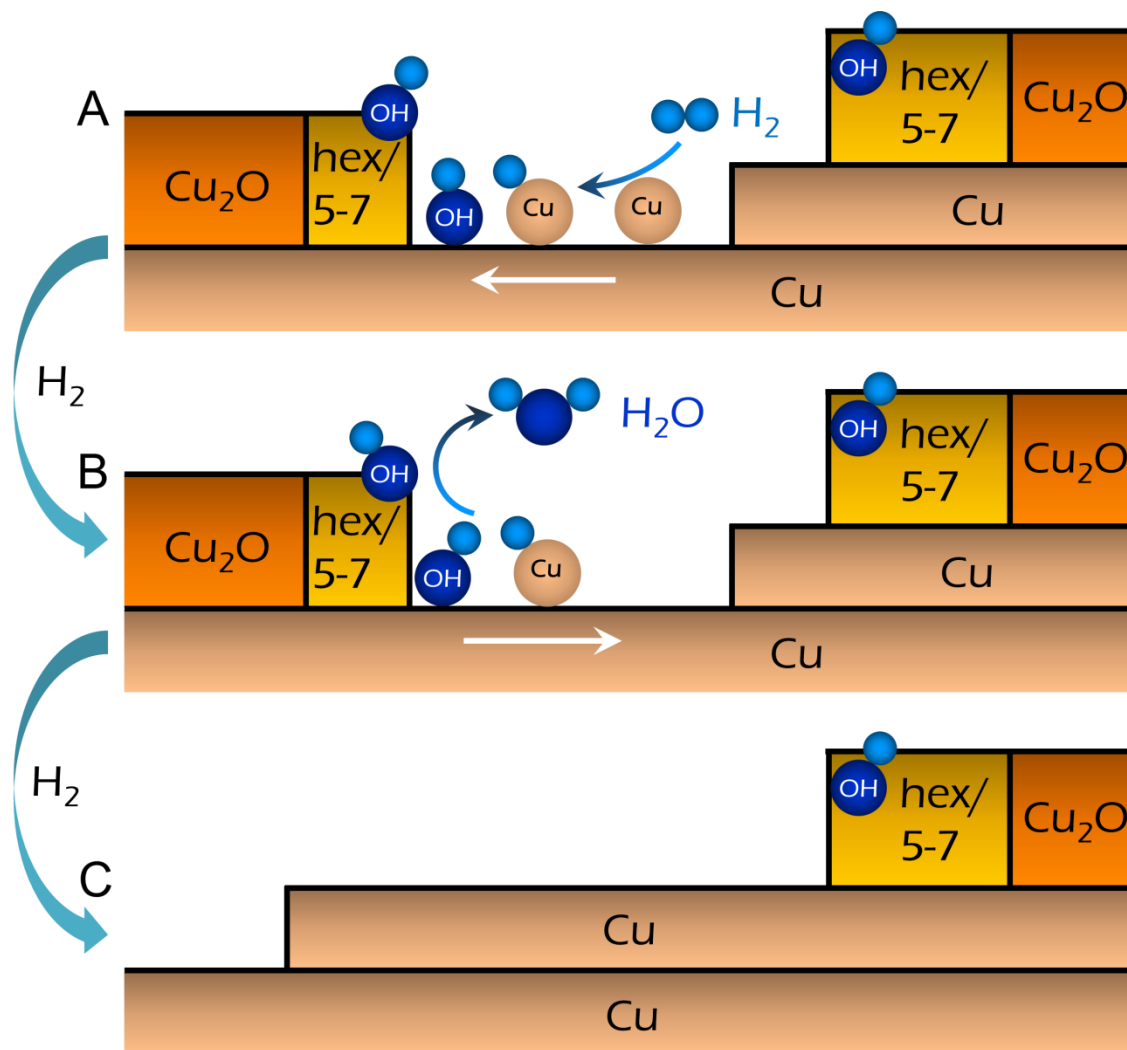
Figure 4.9 *A schematic of $Cu_2O/Cu(111)$ and Cu_2O-hex/5-7 reduction by ambient pressure of H_2 at 300 K.*

4.3.3 A comparison of CO and H_2 reducing $Cu_2O/Cu(111)$

The ambient pressure STM results for reduction of $Cu_2O/Cu(111)$ in H_2 and CO[60] progress through similar intermediate stages as shown in Figures 4.10A and 4.10B. In both cases, regions of $Cu_2O/Cu(111)$ row structure, intermediate band of Cu_2O-hex/5-7, and metallic Cu are observed. Figures 4.10C and 4.10D show the coverage of these three phases as the function of time during the reductions in Figure 4.7 and 4.2 respectively. In Figure 4.10C, the induction period is not included to make the fast reaction regions comparable between the two reductions.

70

Assume that a chemisorbed oxygen occupies each hexagonal ring center in $Cu_2O/Cu(111)$ and is removed completely in Cu_2O-hex/5-7. In other words, with same area occupied, 0.67 times of the oxygen from Cu_2O-hex/5-7 is equal to the oxygen from $Cu_2O/Cu(111)$. So, before the reduction, we have

$$O\% = Coverage_{[Cu2O/Cu(111)]} = 1 \tag{4.1}$$

and during reduction we have

$$O\% = Coverage_{[Cu2O/Cu(111)]}\% + 0.67 \times Coverage_{[Cu2O\text{-}hex/5\text{-}7]}\% \tag{4.2}$$

Based on equation (4.2), the reaction rate indicated by total oxygen consumption rate is calculated. The oxygen depletion rate in the fast reaction region for Cu_2O reduction by H_2 is $(6.4 \pm 0.1) \times 10^{-5}$ s^{-1}, two orders of magnitude lower than the rate by CO, $(2.1 \pm 0.1) \times 10^{-3}$ s^{-1}. Comparing these results, it is important to note that there is also a two orders of magnitude difference in the gas pressures used: 1.54 Torr H_2 and 0.01 Torr CO, which further emphasizes the massive difference in reducing ability between the two gases at 300 K. The mechanisms are of course rather different as CO is able to react with the oxygen in the CuO_x regions, whereas for reduction by H_2, there is a multistep process requiring H_2 dissociation as well. The smaller area coverage of the intermediate phase under H_2 reduction indicates a larger autocatalytic effect than observed under CO.
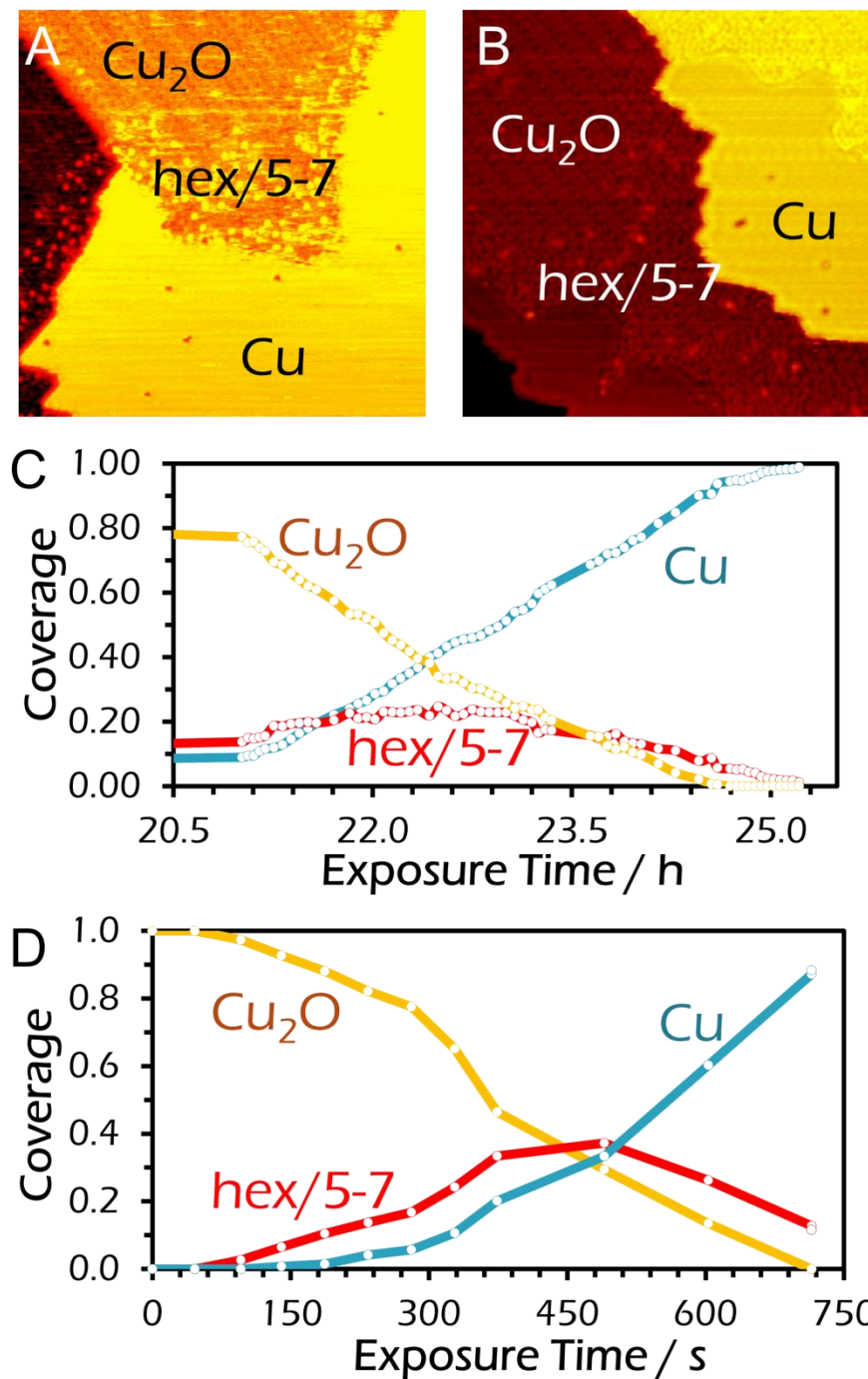
Figure 4.10 *AP-STM images of the reduction of Cu₂O/Cu(111) at single step edge under A) 1.54 Torr H₂ for 23.0 h; B) 10 mTorr CO for 10 min. Both images are is 32×32 nm². I_t = 0.48~0.90 nA; V_t = 0.86~1.09 V. (C, D) Plots showing the area percentage of different CuO$_x$ phases as a function of H₂ and CO exposure time respectively.*

A further comparison between the activation energies of the two systems is shown in Figure 4.11, obtained from IRRAS data. To calculate the rate of the reduction process at varying temperatures, CO was used as a probe molecule to monitor the surface area of the Cu(111) covered by Cu_2O as the reaction occurred. Apparent activation energies for the two reduction reactions are indicated on the graph: E_a (CO) = 0.22 eV and E_a (H_2) = 0.75 eV. Again, it confirms our kinetic measurements based on AP-STM data, reflecting the significantly faster rate of Cu_2O/Cu(111) reduction by CO compared to H_2, and significantly different mechanisms for the two reactions.
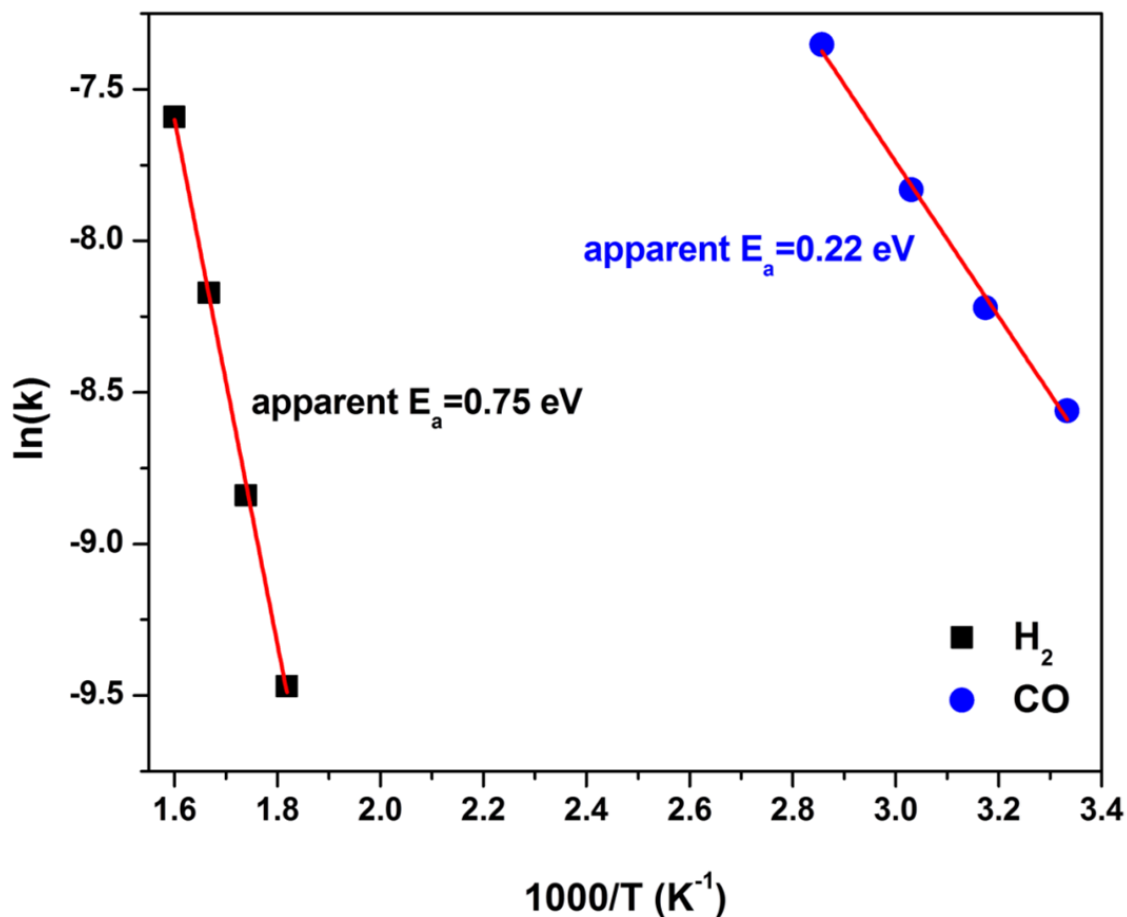
Figure 4.11 *Arrhenius plot comparing the reduction of Cu_2O/Cu(111) by H_2 (black squares) and CO (blue circles) as measured using IRRAS.*

73

4.4 Summary

The reduction of $Cu_2O/Cu(111)$ by CO or H_2 has been studied by in situ AP-STM and AP-IRRAS at 300 K, and ex situ XPS. During both reductions, the intermediate band of Cu_2O-hex/5-7 is in between of $Cu_2O/Cu(111)$ and Cu regions, and reduced Cu atoms diffuse rapidly on surface to join nearby Cu region resulting in metallic front growth by mass transfer. Step edge is the initial active sites for both reduction, however, only CO is able to reduce $Cu_2O/Cu(111)$ to metallic Cu at defects on terraces, starting with buckling of the row structure. Both reductions cause surface topographical changes.

The mechanisms of the two reductions are totally different under ambient pressure gasses at 300 K. CO adsorbs and then reacts with $Cu_2O/Cu(111)$ following Mars-van Krevelen mechanism. The apparent activation energy is 0.22 eV. Under 10 mTorr CO, the full reduction completes within 16 min. However, the apparent activation energy for $Cu_2O/Cu(111)$ reduction by H_2 is 0.75 eV. Thus, reduction by H_2 is orders of magnitude slower than that by CO. Multi-steps are involved. Reduction is barely noticeable until metallic copper is formed. We propose that Cu step edge is a source of under-coordinated copper atoms that can diffuse towards the descending surface. The copper atoms can enhance H_2 dissociation and the water formation. Additionally, the Cu terrace favors water desorption. Both factors contribute to accelerate the reduction, resulting in an obvious autocatalytic effect.

Chapter 5. In situ Imaging of Modified Cu_2O/Cu(111) under Reducing Conditions

5.1 Introduction

As discussed in chapter 4.1, it is known that copper-based heterogeneous catalysts are widely used in various industrial reactions under CO or H_2 environments. The performance of Cu-based catalysts can be greatly improved by addition of modifiers such as alkali metals or other metal/metal oxides.

Alkali metals are widely used as promoter in heterogeneous catalytic processes. Selectivity[136,137] and stability[138] of the original catalysts are improved. Several explanations have been proposed: 1) alkali metals change electronic properties of both surface and adsorbates, such as work function and polarity;[139,140] 2) alkali metals change chemical properties of surfaces and adsorbates, such as weakening the binding between adsorbate and substrate,[141] facilitating dissociation of reactants,[142] and reducing surface upon deposition;[143] 3) alkali metals influence

75

the stability of intermediates[137] and substrates.[143] However, only a few atomically resolved images have been reported of alkali promoters deposited on surfaces under UHV conditions, and to the best of our knowledge, no atomic structures of alkali promoters has been resolved under reaction conditions. In well-defined model systems, alkali metals were reported to be deposited on metals such as Cu(111),[144,145] Ni(111),[142] and Pb thin films;[146] metal oxides such as TiO$_2$(110)[143,147] CaO(001),[139] Fe$_3$O$_4$(001),[140] Fe$_3$O$_4$(111),[148] Cr$_2$O$_3$(0001)/Cr(110),[149] and thin silica film.[150] The main focus has been the static topographic and theoretic studies. The dynamic picture on the performance of alkali metals is still completely unknown.

Ceria is famous in heterogeneous catalysis for the oxygen storage ability or reducibility. It can easily convert between Ce^{3+} and Ce^{4+} during reaction, depending on oxidizing or reducing conditions. Ceria or copper itself are not highly active catalysts, however, when they are combined, the system becomes very efficient for redox reactions,[151] preferential oxidation of CO,[44,152] water-gas shift reaction,[10,153] and methanol synthesis from CO$_2$.[17] Ceria-copper systems are highly active because: 1) when low coverage of ceria is deposited on copper substrates, the formed metal-oxide interface is the active site for the mentioned reaction;[17] 2) Ce^{3+} is present with oxygen vacancies, which are also highly active sites.[154] Some pioneer studies have been done on defining CeO$_2$/Cu$_2$O/Cu(111) system. When thick film is grown, only CeO$_2$(111) is observed,[155] however, when ceria is grown at less than a monolayer coverage, both CeO$_2$(111) and CeO$_2$(100) islands can form on Cu(111) depending on deposition flux, temperature, and O$_2$ pressure.[156] Similar with the situation with alkali promoter, there is a need to know the dynamic information of ceria islands under reaction conditions.

This chapter is focused on in situ surface dynamic transformations of potassium modified $Cu_2O/Cu(111)$ surface and $CeO_2(111)/Cu_2O/Cu(111)$ under ambient pressures CO or H_2 by AP-STM, and AP-XPS. The role of potassium and ceria sites will also be discussed.

5.2 Experimental Methods

A Cu(111) single crystal (Princeton Scientific Corp) was cleaned by sputtering (Ar^+, 5 µA, 2 keV, 20 min) and annealing (700 K, 10 min) cycles in a chamber with a background pressure of 5×10^{-10} Torr. The clean Cu(111) was annealed in 5.0×10^{-7} Torr O_2 for 20 min at 550 – 650 K, in order to form $Cu_2O/Cu(111)$.

A home-made doser with feedthrough and a potassium getter was mounted normally to $Cu_2O/Cu(111)$ surface for deposition purpose. All of the depositions were made at room temperature and the surfaces were post annealed under 6×10^{-7} mbar O_2 at 500 K for 10 min to form flat terraces.

Cerium vapor from a Triple Evaporator EFM 3T (Focus, Omicron Nano Technology) was deposited on $Cu_2O/Cu(111)$ or the clean Cu(111) or for 15 min in 4.5×10^{-7} Torr O_2 (GTS-WELCO, 99.9999% pure) at 350 ℃ with a flux of 20~80 nA. In order to maintain high Ce oxidation states, the sample was oxidized for another 10 min and cooled down in an O_2 background. The as-prepared sample was transferred to an STM stage combined high pressure cell which locates inside of a SPECS™ Aarhus 150 HT STM. The STM cell was then sealed and filled with 1.5 Torr H_2 (GTS-WELCO, 99.9999% pure) using a hydrogen purifier of liquid nitrogen trap in the gas line. STM images were obtained at 300 K. A baratron gauge (MKS 626B) was used to monitor gas pressure in avoid of potential impurities emitted by a filament

gauge. A commercialized etched tungsten tip is used for all of the scanning under constant current mode.

AP-XPS spectra were collected at beamline X1A1 (National Synchrotron Light Source-I) and beamline CSX-2 (National Synchrotron Light Source-II), Brookhaven National Laboratory. Instruments are equipped with analyzer which is differentially pumped to maintain under UHV and electrostatic focusing lenses.

5.3 Results and Discussion

5.3.1 Potassium modified Cu_2O/Cu(111)

The STM images of as-prepared potassium modified Cu_2O/Cu(111) is shown in Figure 5.1. The potassium related species are imaged as bright features. As evaporating flux increasing from Figure 5.1A to 5.1C with a similar deposition time, Cu_2O/Cu(111) gradually decomposes. According to XPS which is not shown here, potassium is immediately oxidized upon being deposited on Cu_2O/Cu(111). The fact that metallic potassium reduces metal oxide surface upon deposition is not unique: Fe_3O_4(111) surface is also reduce by metallic potassium deposition.[148] Thus, with a larger amount of potassium, Cu_2O/Cu(111) is reduced more. In Figure 5.1C, row structure of Cu_2O/Cu(111) is fully decomposed to hexagonal ring structure with domains at different orientations, indicating a delocalized feature. Interestingly, the spacing of the hexagonal pattern is ~8.5 Å, 42% larger than 6 Å, the spacing of Cu_2O hexagonal structure. The short periodicity indicates the structure is not most thermo-stable. The highly resolved STM image in Figure 5.1C shows that the potassium related species also adopt the spacing of the hexagonal patterned ring structure, highlighted in two sets of blue points that are of the same spacing. It has

been reported that alkali metals adsorb on anion sites[147] and cation sites[157] on metal oxide. Since potassium is oxidized, it more likely to adopt oxygen sites upon deposition. When deposited on silica monolayer film, Li lands in between the film and substrate.[150] However, with STM alone, it's hard to determine whether potassium penetrates the hexagonal structure.
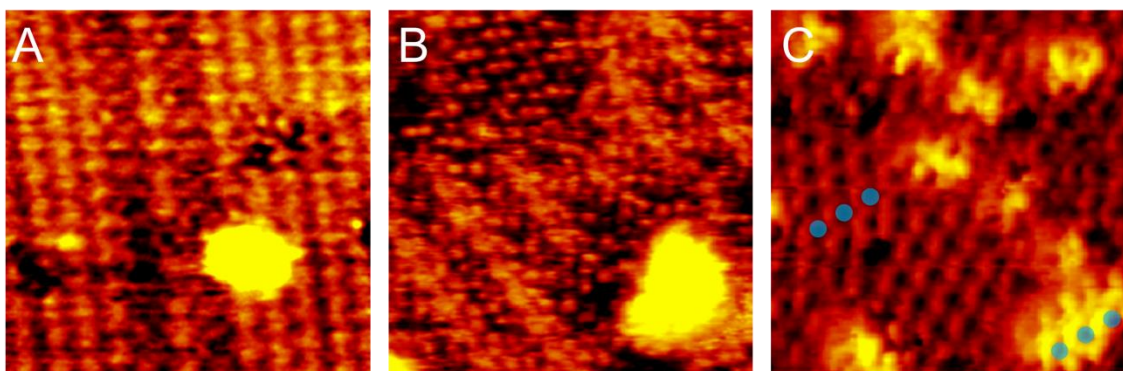
Figure 5.1 *STM images of as-deposited potassium on Cu$_2$O/Cu(111) with flux increase from A) to C). All of the images were obtained under UHV at 300 K with a shared size of 10×10 nm^2. I$_t$ = 0.33~0.52 nA; V$_t$ = 0.34~0.48 V.*

With the same flux used in Figure 5.1C and different depositing time, coverage from small to large is obtained. The as-deposited surface is further oxidized under 6×10^{-7} mbar O$_2$ at 500 K for 10 min to obtain a reoxidized flat surface. After annealing, surfaces regain long range order as shown in Figure 5.2. The potassium coverage increases from 5.2A to 5.2C. At the lowest potassium coverage, surface reforms row structure with hexagonal ring structure as a dominant, Figure 5.2A. The spacing of the ring structure is ~8.8 Å. Both two to four lines of the ring structure are observed. In Figure 5.2B at middle potassium coverage, square-like pattern with a smaller spacing of 6.1×6.9 Å^2 is observed. The surface is divided by dark lines, which will be discussed later. In Figure 5.2C with high potassium coverage, surface transforms back to hexagonal patterns with a spacing of ~9 Å. In this case, no row structures are observed. All of

the patterns are due to potassium modification and are not observed with only Cu_2O monolayer film. However, potassium sites cannot be identified based on STM images.
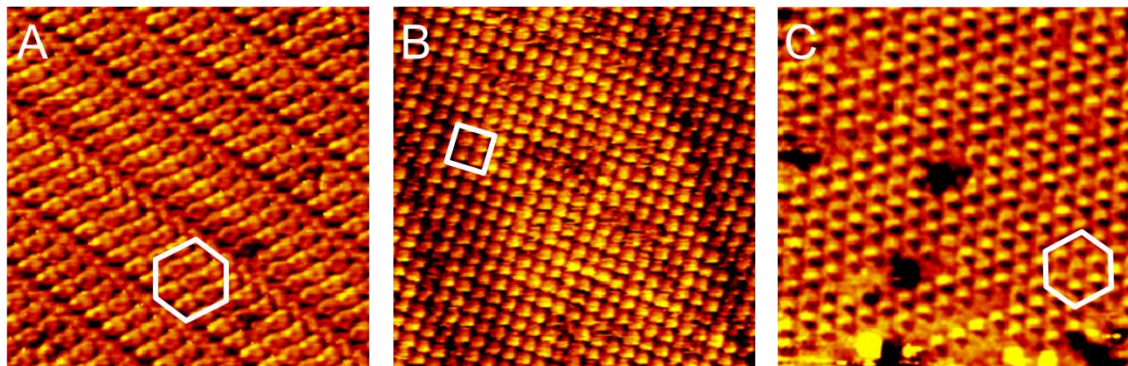
Figure 5.2 *STM images of reoxidized potassium modified $Cu_2O/Cu(111)$ surface. Potassium coverage increases from A) to C). All of the images were obtained under UHV at 300 K with a shared size of 15×15 nm². I_t = -2.67~0.85 nA; V_t = -0.65~1.68 V. Hexagon and rectangle are drawn to guide eyes.*

Atomically resolved STM images of the pattern in Figure 5.2B were obtained. In Figure 5.3A, due to the tip change during scanning, the surface is resolved better in the top part. It is obvious that the near-square pattern is actually composed of heavily distorted hexagonal rings. Considering the spacing, the distorted structure may be adapted from Cu_2O hexagonal ring structures. In Figure 5.3B and 5.3C, it is found that the dark line in Figure 5.2B is the domain boundary with a lattice mismatch from both sides. The domain boundary of six-membered ring structure in Polycrystalline Graphene is studied by Loh's group. They found that the boundary created by lattice mismatch is made up of periodic five membered, seven membered and eight membered rings.[158] Based on their theory and STM images, atomic schematic overlayers are drawn in Figure 5.2B and 5.2C. The domain boundary is also made up of periodic five-by seven membered ring structures.
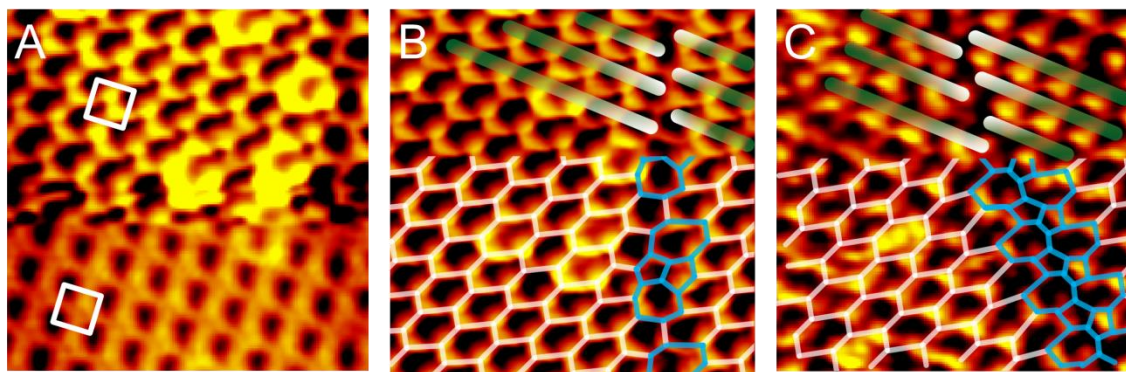
Figure 5.3 *Atomically resolved STM images of the pattern in Figure 5.2B. All of the images were obtained under UHV at 300 K with a shared size of 6×6 nm². I_t = -0.64~0.85 nA; V_t = -1.32~0.76 V. Near square pattern is highlighted in white in A). In B) and C), atomic schematic arrangement of ring structure is shown. Five membered by seven membered rings are highlighted in blue. Straight lines of the hexagonal rings are also drawn.*

5.3.2 Reduction of potassium modified Cu₂O/Cu(111) by ambient pressures of CO

The reduction of as-deposited potassium modified Cu₂O/Cu(111) by ambient pressure CO is shown in Figure 5.4. The bottom part of Figure 5.4A is the as-prepared surface with potassium related sites marked by blue balls. 1.5 mTorr CO was introduced on the surface during the middle of the image, indicated by an increased noise level. Within 1 min, reduction occurs on top of Figure 5.4A. In the next image scanned from bottom to top in Figure 5.4B, surface is completely reduced. The reduced Cu is isolated as small irregular shaped islands on the surface, which is different from the post reduction surface of pure Cu₂O/Cu(111) where big terraces of metallic copper is observed. According to the blue markers, reduction initiates on the potassium related sites. Figure 5.4C is the IRRAS pre- and post- reduction of the corresponding potassium modified surface under 2.0×10^{-4} Torr CO at 300 K. CO is used as a probe molecule, and all the spectra were measured below 200 K for CO to adsorb on the surface. Before reduction, only one adsorption peak appears at 2088 cm^{-1}, which is red shifted from CO adsorption peak on Cu₂O/Cu(111) at 2097 cm^{-1}.[81] The red shift is potassium coverage dependent. After reduction, at

200 K where CO cannot absorb on Cu(111), a peak at 1520 cm^{-1} is observed. This peak is assigned to surface carbonate,[159] which has a different peak position from bulk carbonate salt. After the temperature is cooled to 120 K, a CO adsorption peak on Cu(111) is observed at 2071 cm^{-1}.[81] It agrees with STM data that after reduction metallic copper is formed.
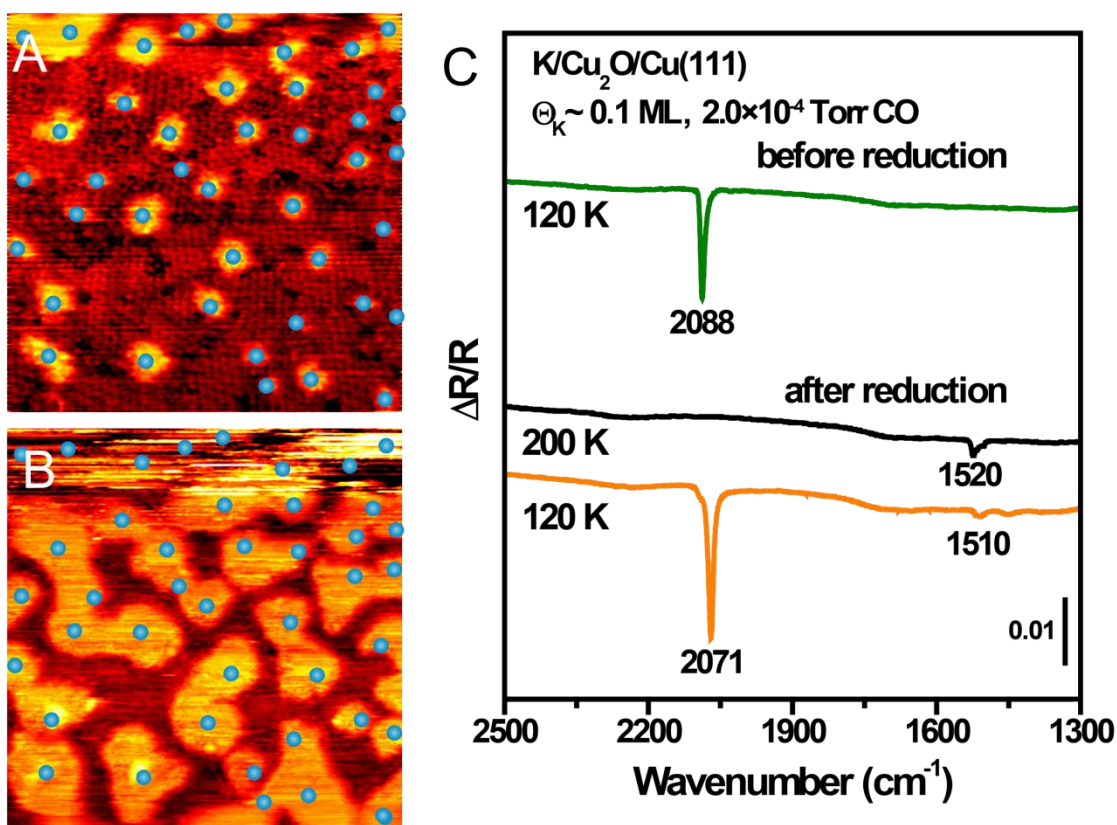
Figure 5.4 As prepared potassium modified $Cu_2O/Cu(111)$ reduction by ambient pressure CO. 1.5 mTorr CO was dosed on the surface in the middle of A) and the surface was continuously scanned from bottom to top for 2 min in B). Blue balls are markers indicating the as-prepared potassium related sites. Both images are 35×35 nm^2. $I_t = 0.48 \sim 0.49$ nA; $V_t = 0.97$ V. IRRAS spectra are shown in C) of the potassium modified $Cu_2O/Cu(111)$ before and after reduction by 2.0×10^{-4} Torr CO. Reduction was at 300 K, and spectra were collected at low temperatures indicated in C).

Since potassium is oxidized and $Cu_2O/Cu(111)$ is reduced upon potassium deposition, the surface needs to be reoxidized in order to compare reduction speed fairly with $Cu_2O/Cu(111)$. According to XPS O 1s spectra of both surfaces reduction by 10 mTorr CO at 300 K,

Cu$_2$O/Cu(111) is fully reduced within 28 min, while reoxidized potassium modified Cu$_2$O/Cu(111) surface is fully reduced much more rapidly within 1 min. Thus, potassium related species promote CuO$_x$ reduction by CO. The system with K is further studied by ex situ IRRAS and XPS and in situ STM in order to explain the rate difference.

Figure 5.5 shows the ex situ IRRAS (Figure 5.5A) and XPS data (Figure 5.5B) of reoxidized K modified Cu$_2$O/Cu(111) surface reduction by ambient pressure CO. Before reduction, CO adsorbs on the reoxidized surface at 2110 cm^{-1} at low temperatures and desorbs at 130 K. This peak is assigned as CO adsorption on Cu$^+$ sites.[128] After reduction, surface is reduced to metallic Cu, as indicated by CO adsorption peak on Cu(111) at 2068 cm^{-1} at 140 K. The red shift from the adsorption peak in Figure 5.4 is due to the increase of potassium coverage. At 120 K, more CO adsorbs on Cu(111) and the peak intensity increases. Additionally, a surface carbonate peak at 1520 cm^{-1} is also observed independent of temperature. The formation of carbonate species is further confirmed with C 1s spectra in Figure 5.5B. Before reduction, no carbon related species is on the surface. After reduction, a carbonate peak appears at 288.9 eV, which disappears upon annealing to 500 K under UHV. Furthermore, according to K 2p spectra, potassium is maintained as K$^+$ (296 and 293 eV) before and after reduction. When carbonate is decomposed at elevated temperature, K$^+$ is reduced to K (297 and 294 eV). Thus, we conclude that carbonate species form on the reoxidized potassium modified Cu$_2$O/Cu(111) surface during reduction by CO.
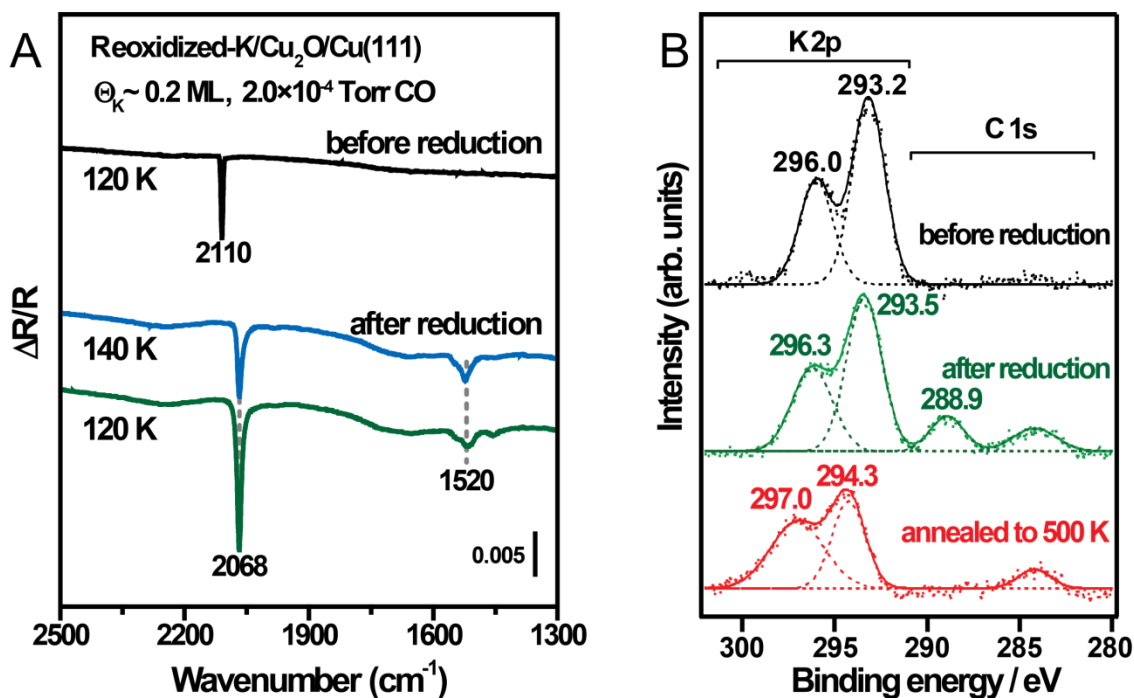
Figure 5.5 *Identifications of chemical species on reoxidized K modified $Cu_2O/Cu(111)$ surface before and after reduction by CO at 300 K. A) IRRAS data collected at low temperature indicated on the graph before and after exposing the surface to 0.2 mTorr CO. B) XPS data collected at 300 K before and after exposing the surface to 10 mTorr CO.*

A corresponding AP-STM experiment was conducted to investigate the topography of the reoxidized potassium modified $Cu_2O/Cu(111)$ surface. Figure 5.6A is the filled state image of the reoxidized surface, which is covered by the row structure in Figure 5.2A with some defects. An empty state image of the surface is shown in Figure 5.6B after 3.4×10^{-4} Torr CO is dosed to the system for 8 min. Surface is still covered by row structures with defects. Thus, an induction period exists. The row structures become locally disorder after 30 min exposure to CO, Figure 5.6C. Shortly after that, metallic copper forms at the step edge, Figure 5.6D. Then, metallic copper forms both from the step edge and on terrace, Figure 5.6E. Within 4 min, the surface is fully reduced to isolated copper islands. The post reaction surface in Figure 5.6F is very similar to that in Figure 5.4B. Thus, we propose that potassium species still behave as active sites during the reduction.
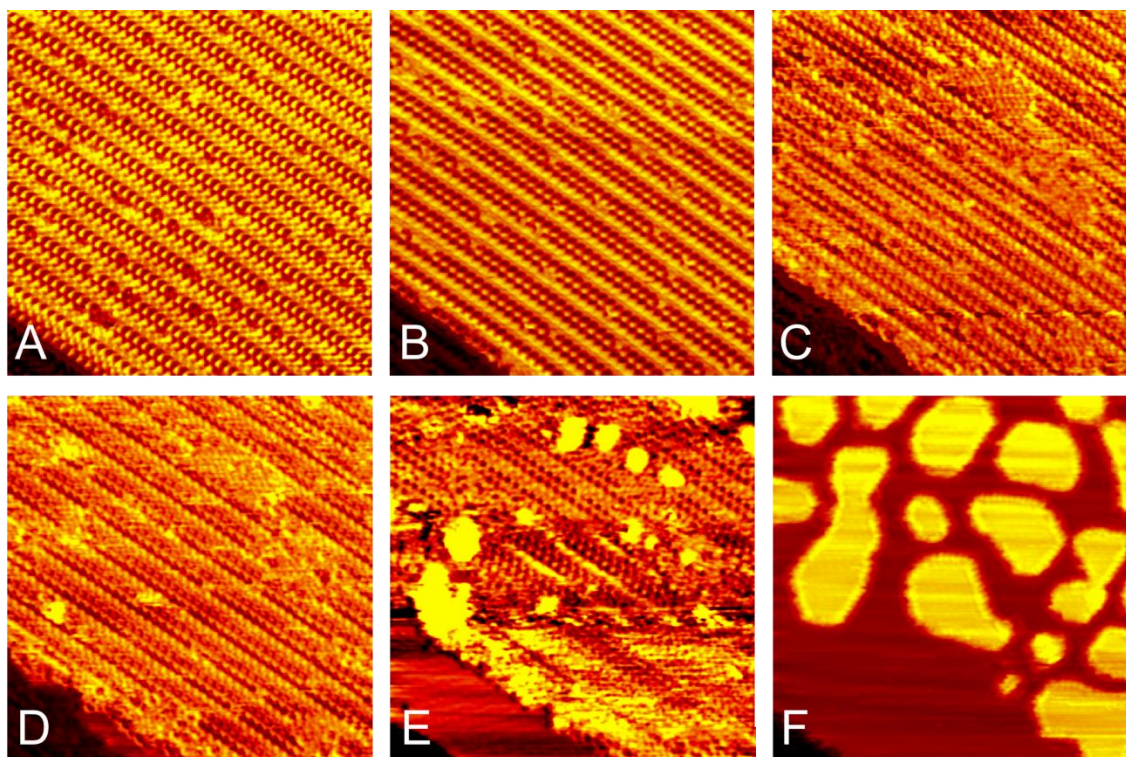
Figure 5.6 *In situ AP-STM images of reoxidized potassium modified $Cu_2O/Cu(111)$ surface reduction by 3.4×10^{-4} Torr CO at 300 K. The exposure time from A) to F) is 0 min, 8 min, 33 min, 36 min, 40 min, and 43 min, respectively. All of the images are 35×35 nm^2. I_t = -0.47~0.51 nA; V_t = -1.06~1.06 V.*

After reduction in Figure 5.6F, each copper island is surrounded by a second species, which is not observed with $Cu_2O/Cu(111)$ reduction by CO. Since the only difference by adding potassium to the system is: a) in terms of IRRA and XPS, the formation of carbonate; and b) in terms of STM, the formation of a second species around step edges of Cu islands, thus, the second species observed in STM is naturally assigned as potassium carbonate. Due to a change of scanning conditions, surface carbonate can be imaged as dark features (Figure 5.7A) or bright features (Figure 5.7B). A zoomed-in image clearly resolves the near-squared structural pattern of a carbonate island (the insertion in Figure 5.7B). The spacing of the periodic carbonate is ~4.1 Å. Within ~50 min under vacuum, Cu islands shrink and neighboring carbonate phase expands, indicating by white arrows in Figure 5.7A and 5.7B. The self-assembly carbonate is attached to

85

the step edge of Cu islands and terraces, indicated by yellow arrows in Figure 5.7C and 5.7D. Thus, both copper and potassium carbonate are mobile on the surface. The aggregation/phase separation is obvious on metallic Cu, where surface corrugation is small.
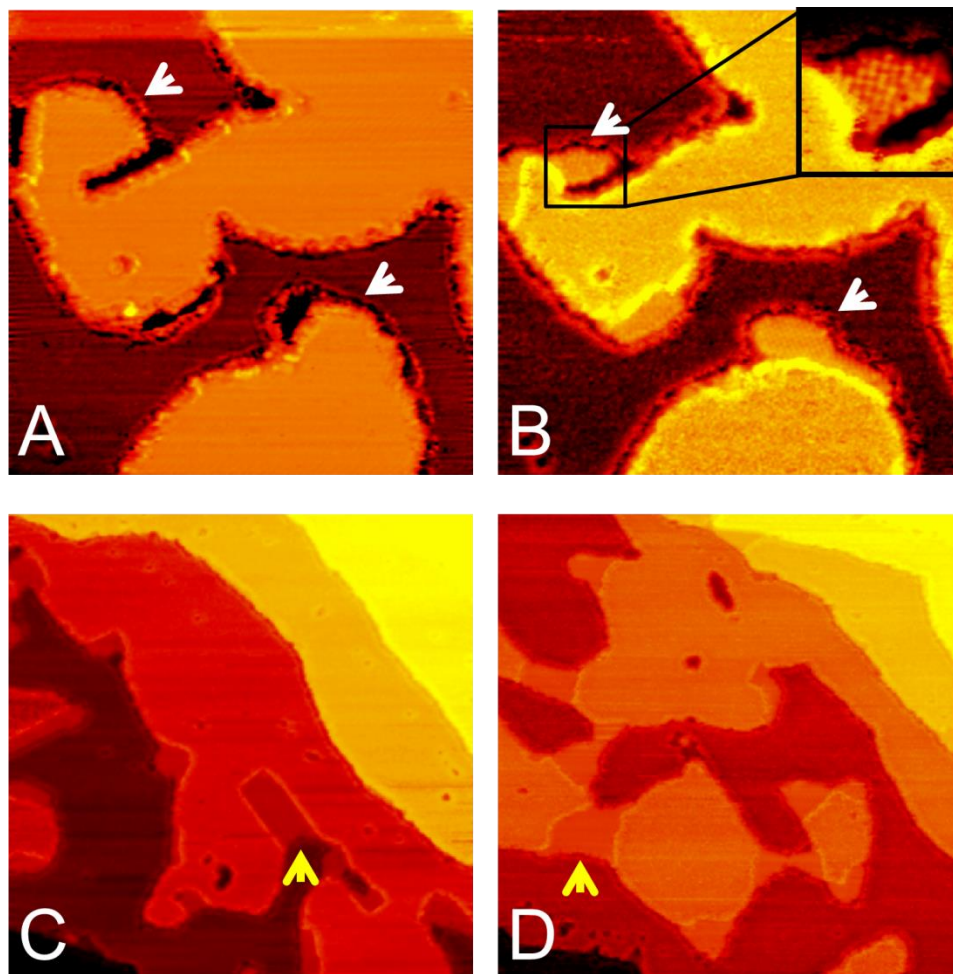
Figure 5.7 *Post-reaction topography of reduced reoxidized potassium modified $Cu_2O/Cu(111)$ surface at 300 K. The CO evacuation time from A) to D) is 7 min, 55 min, 76 min, and 98 min, respectively. A) and B) are of the same area. White arrows show the self-assembly of potassium carbonate phase. Yellow arrows indicate the location of carbonate. A) and B) are 35×35 nm^2, and C) and D) are 70×70 nm^2, $I_t = -0.63 \sim -0.77$ nA; $V_t = -1.06$ V.*

5.3.3 Reduction of potassium modified Cu₂O/Cu(111) by ambient pressures of H₂

Potassium related site greatly facilitates copper oxide reduction by CO, however, it does not exhibit an obvious effect on the reduction by H_2 at 300 K. Figure 5.8 shows the process of potassium modified CuO_x/Cu(111) reduction by 2.15 Torr H_2. In Figure 5.8A, an area against a step edge composed of potassium related sites (bright features) and oxide ring structures is highlighted in white dash lines. After being exposed by 2.15 Torr H_2 for 0.6 h, the highlighted area is reduced towards the step edge with few changes to potassium related sites. Thus, in terms of accelerating the copper oxide reduction by H_2, metallic copper overwhelms potassium related sites.
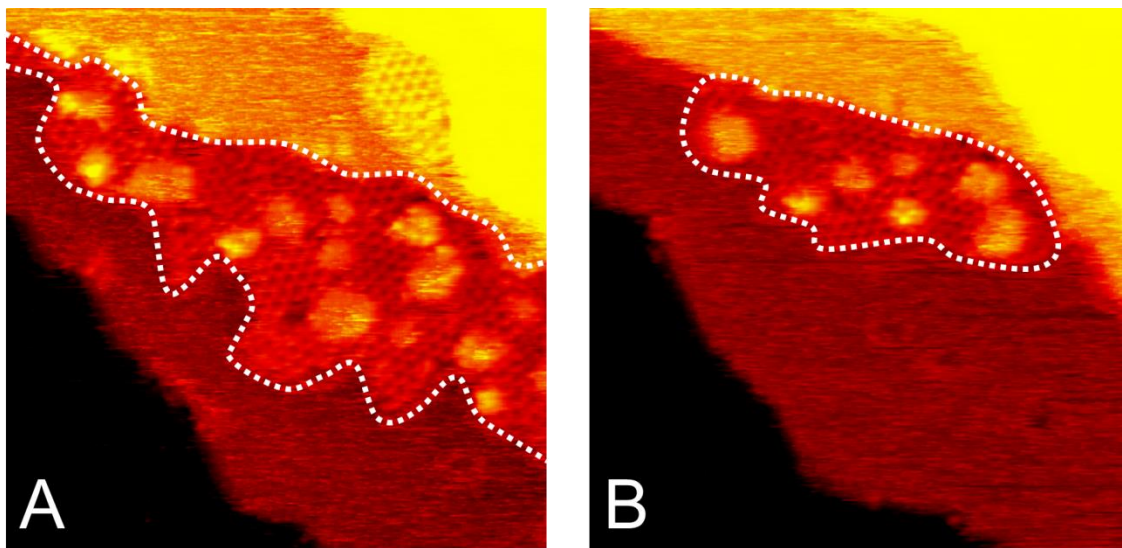
Figure 5.8 *In situ AP-STM images of potassium modified CuO_x/Cu(111) reduction by 2.15 Torr H_2 at 300 K. A) and B) are of the same area with H_2 exposure time of 0.8 h and 1.4 h respectively. The potassium modified CuO_x/Cu(111) region is circled by white dash lines. Both images are 32×32 nm^2, $I_t = -0.05 \sim -0.06$ nA; $V_t = -1.68$ V.*

A complete reoxidized potassium modified Cu_2O/Cu(111) reduction by 2.16 Torr H_2 is monitored by AP-STM at 300 K, Figure 5.9. Before reduction, the surface is covered by the row structure in Figure 5.2A. Similar to Cu_2O/Cu(111) reduction by ambient pressure H_2, a long

induction period exists for hours, Figure 5.9A and 5.9B. After ~7 h, metallic copper starts to form from step edges, Figure 5.9C. The black hole in Figure 5.9C was created by applying a high voltage pulse, and is a land mark. Unlike the system without potassium where step edge is the only observed initial active sites for metallic copper, in the system with potassium, metallic copper can also form on terraces, possibly on potassium related sites, Figure 5.9D. As the reduction proceeds, metallic copper area grows and reoxidized potassium modified $Cu_2O/Cu(111)$ row structure shrinks, Figure 5.9E to 5.9H. Faceted edges of metallic copper island along Cu(111) close packed <110> directions are observed during reduction, Figure 5.9F. Interestingly, despite the continuous growth of metallic copper area, potassium modified copper oxide regrows to form a perfect hexagonal pattern after ~14 h of reduction, bottom part of Figure 5.9H and 5.9I. The hexagonal pattern has a spacing of ~9.0 Å, and closed packed direction is ~15° off the <110> direction and ~17° off the direction of reoxidized potassium modified $Cu_2O/Cu(111)$ row structure. Noting that no oxygen exists in gas phase, the hexagonal pattern can be relaxation of reoxidized potassium modified $Cu_2O/Cu(111)$ row structure, which is highly mobile under ambient pressure H_2. With further exposure to ambient pressure H_2, metallic copper forms within the hexagonal structure, Figure 5.9J and 5.9K, until oxide is completely reduced, Figure 5.9L.
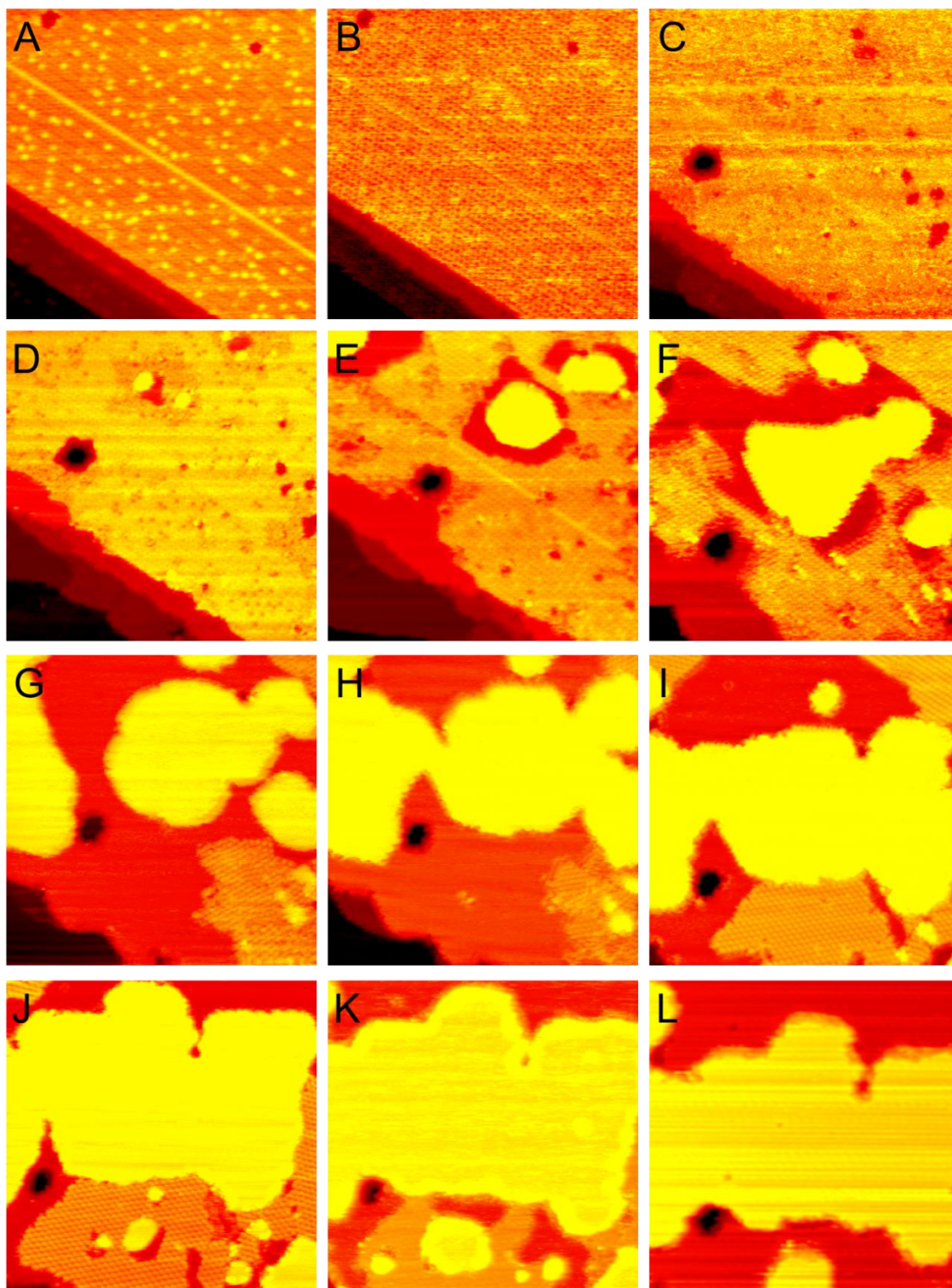
Figure 5.9 *In situ AP-STM images of re-oxidized potassium modified Cu₂O/Cu(111) reduction by 2.16 Torr H₂ at 300 K. Reduction time from A) to L) is 1.6 h, 5.8 h, 7.2 h, 7.7 h, 9.4 h, 12.1 h, 13.3 h, 13.9 h, 16.3 h, 21.3 h, 32.1 h, and 36.3 h. All the images are 45×45 nm², $I_t = -0.23 \sim 0.39$ nA; $V_t = -1.58 \sim 0.97$ V. A) and B) were imaged for empty states, and C) to L) were imaged for filled states.*

The total reduction takes 36.3 h, longer than the total reduction time of $Cu_2O/Cu(111)$ by the same pressure of H_2 at 300 K. The role of potassium towards hydrogenation is debatable. It is reported that potassium can decrease the sticking coefficient of hydrogen on metals such as Fe(111),[160] Pd(100),[161] Pd/SiO$_2$,[162] Ru/SiO$_2$,[163] Fe/SiO$_2$,[164] and is a poison for H_2 dissociation on metals such as Pt(111),[165] Ni(111).[166] However, potassium is also reported to enhance H_2 storage in K-doped carbon nanocone,[167] and be a good adsorption site for atomic hydrogen on MgO(100),[168] Pd(100),[161,169] K/Cu(110).[170] According to our results, comparing with $Cu_2O/Cu(111)$ reduction by H_2, a longer induction period and a slower reaction speed were observed in the reduction of reoxidized potassium modified $Cu_2O/Cu(111)$, which indicates the prohibit role of potassium related species during hydrogenation process. However, more initial copper formation on terraces with potassium modification indicates potassium related species are active sites for metallic copper formation. One explanation is potassium species create defects that are active sites for the reduction, but potassium related species are poisons to hydrogenation.

5.3.4 Hydrogenation of CeO$_2$(111)/Cu$_2$O/Cu(111)

A $CeO_2/Cu_2O/Cu(111)$ reduction by 1.5 Torr H_2 at 300 K is shown in Figure 5.10. The as-prepared CeO_2 island is formed along a step edge, with nearby terraces covered with $Cu_2O/Cu(111)$, Figure 5.10A. The one-layer thick island exhibits a rough surface with occasionally CeO_2(111) termination. After the surface is exposed to 1.5 Torr of H_2 at 300 K for 26 h, Figure 5.10B, Ce^{4+} is reduced to Ce^{3+} and Cu^+ is reduced to Cu. Furthermore, clusters of O vacancies in the Ce_2O_3 island are formed with the geometry of the island unchanged. Reduction in hydrogen expands ceria-copper interface and roughens the surface. The CeO_x-Cu(111) oxide-

metal interface and the phase $Ce_2O_3/Cu(111)$ is believed to be the active phase for methanol synthesis from CO_2.[17] Thus, the reduced surface is more active for the reaction.
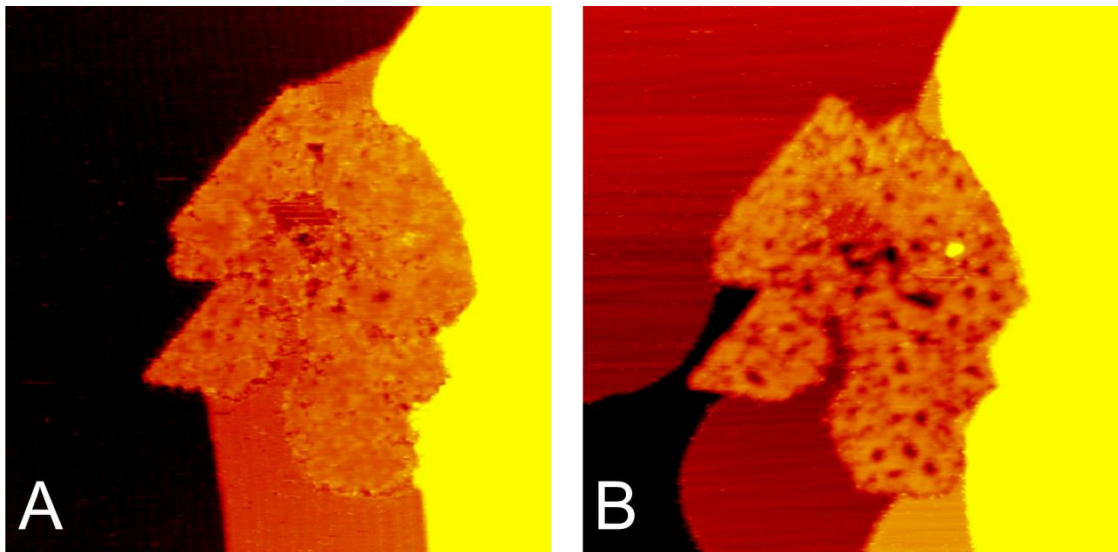
Figure 5.10 *In situ AP-STM of $CeO_2/Cu_2O/Cu(111)$ reduction by 1.5 Torr of H_2 at 300 K. The exposure time of A) and B) is 0 h and 26 h respectively. Both images are 100×100 nm^2, $I_t = 0.27\sim0.36$ nA; $V_t = 0.94\sim1.16$ V.*

A complete $CeO_2/Cu_2O/Cu(111)$ reduction process by a slightly higher pressure at 1.66 Torr of H_2 is imaged at 300 K by AP-STM. Figure 5.11A shows the as-prepared $CeO_2/Cu_2O/Cu(111)$, where the one layer thick island is also along a step edge with $CeO_2(111)$ termination. After being exposed under 1.66 Torr H_2 for 2.0 h, bright features appear on $Cu_2O/Cu(111)$ and CeO_x island, highlighted in Figure 5.10B. The bright features, which are not observed under $Cu_2O/Cu(111)$ reduction by ambient pressure of H_2 or on the as-prepared surface, indicate that reduction occurs at Ce^{4+} sites. Thus, Ce^{4+} is more active than Cu^+ sites towards hydrogenation. With reduction for another $\sim$2 h, metallic copper starts to form at step edges. The Cu-Cu fronts are highlighted as white dash lines in Figure 5.11C. The reduction of copper follows the phenomena observed with $Cu_2O/Cu(111)$ reduction by ambient pressure of H_2 in chapter 4 with one exceptional that CeO_x clusters on $Cu_2O/Cu(111)$ region can also be a

91

nucleate site for metallic copper, highlighted in blue dash lines in Figure 5.11D and 5.11E. If a small Cu island has a rich copper source, it expands and is stable by the end of reduction, such as the terrace in the top of Figure 5.11F. If a small Cu island has a poor copper source, it is not stable and will diffuse to join nearby terraces by the end of reduction, such as the smaller island in Figure 5.11E. The fully reduction completes within 11.2 h, and the metal-oxide interface on Ce_2O_3 island is expanded, Figure 5.11F. Additionally, the bright features of CeO_x sites disappear after reduction, very possibly due to instability and high mobility on metallic copper. Thus, ceria sites are more active than $Cu_2O/Cu(111)$ towards hydrogenation process at 300 K, and ceria sites on $Cu_2O/Cu(111)$ can be the nucleate site for metallic Cu region.
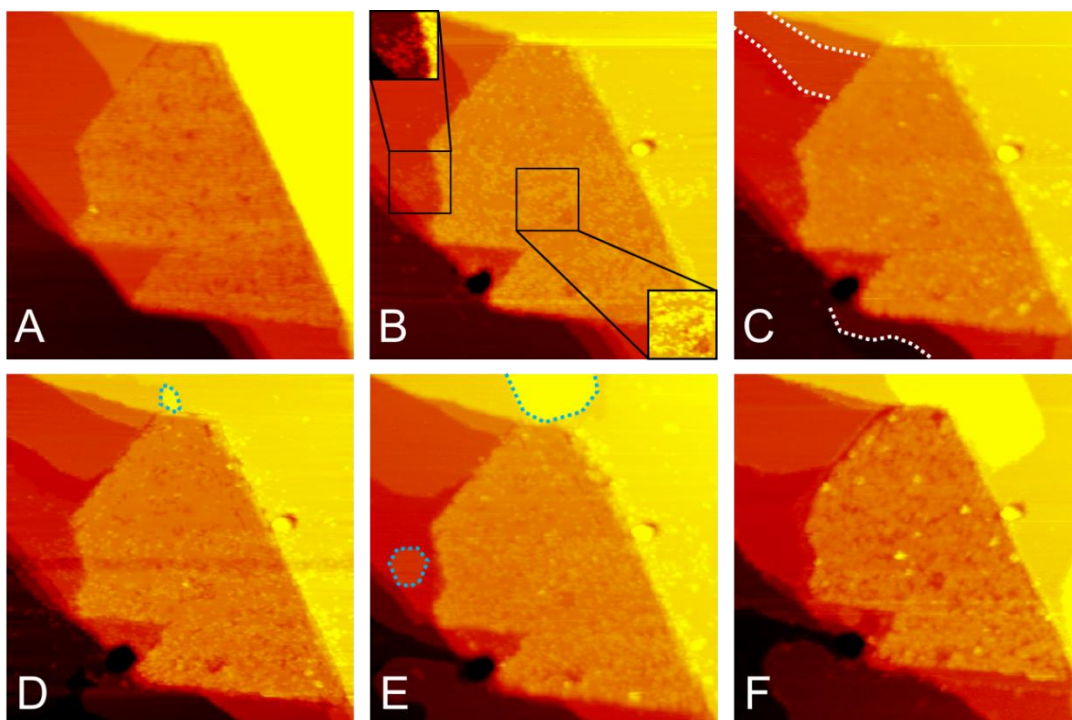
Figure 5.11 *In situ AP-STM images of $CeO_2/Cu_2O/Cu(111)$ reduction by 1.66 Torr of H_2. A) shows the as-prepared surface. The exposure time from B) to E) is 2.0 h, 4.3 h, 5.3 h, and 6.5 h, respectively. Details are highlighted in B) with a better contrast. White dash lines in C) are Cu-Cu step edges. Metallic Cu islands are highlighted in blue dashed circles in D) and E). The complete reduction costs 11.2 h, and E) shows the surface after fully reduction with H_2 evacuated. All of the images are 100×100 nm^2, $I_t = 0.33 \sim 0.42$ nA; $V_t = 1.03 \sim 2.02$ V.*

5.3.5 Potassium modified post hydrogenated surface of CeO$_2$(111)/Cu$_2$O/Cu(111)

Potassium disperses evenly on CeO$_2$/Cu$_2$O/Cu(111) surface by vapor deposition at 300 K. After exposure 2.6 Torr H$_2$ for 18.9 h at 300 K, surface is roughened but no obvious reduction is observed. It is in agreement with prohibiting effect of potassium related sites during hydrogenation process discussed in section 5.3.3. Instead of deposition potassium prior to high pressure of H$_2$, CeO$_2$/Cu$_2$O/Cu(111) surface is first reduced to Ce$_2$O$_3$/Cu(111) and then interaction between potassium and the reduced surface is studied.

Complete reduction of CeO$_2$/Cu$_2$O/Cu(111) surface is obtained by exposing the surface under 2.2×10^{-6} mbar of H$_2$ for 1 h at 573K, Figure 5.12A. The STM image is sharpened to make step edges obvious. The mixture of Ce$_2$O$_3$(111) and Ce$_2$O$_3$(100) terminations are formed depending on preparing conditions. Additionally, the Ce$_2$O$_3$ islands are two layers thick near edges and one layer thick in the center. Metallic potassium is then deposited on the Ce$_2$O$_3$/Cu(111) surface at 300 K, Figure 5.12B. Low coverages of potassium is invisible on Cu(111). Thus, in Figure 5.12B, potassium should well disperse on the surface but the majority of potassium on Cu(111) is not imaged. Ce$_2$O$_3$/Cu(111) island is roughened with potassium modification. Metallic potassium is very active, and can easily react with background gases. An amorphous feature, which is assigned as reacted potassium, appears at the descending step edge sites and metal-oxide interfaces. It is because 1) reacted potassium molecules have mobility on the surface and are stable at these sites; and/or 2) potassium atoms at these sites are more reactive than those on terraces. After leaving the surface under UHV for two days when potassium atoms are fully reacted with background gases, surface is covered by amorphous structures, Figure 5.12C. Topographies of surfaces with substrates of cerium oxide island (circled in a white dashed line) and Cu(111) are very similar.
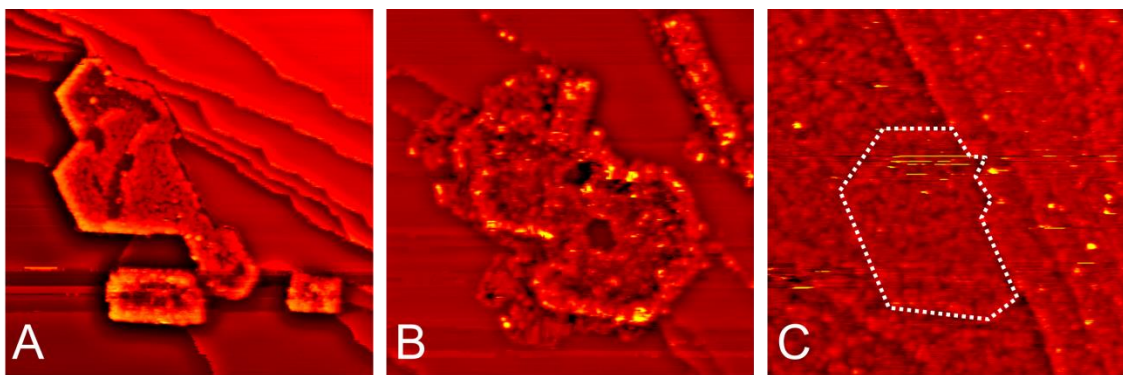
Figure 5.12 *Sharpened ex situ STM images at 300 K. A) $Ce_2O_3/Cu(111)$ surface prepared by reducing $CeO_2/Cu_2O/Cu(111)$ by 2.2×10^{-6} mbar of H_2 for 1 h at 573K. B) Potassium vapor deposited $Ce_2O_3/Cu(111)$ surface. C) Surface of potassium modified $Ce_2O_3/Cu(111)$ after being remained under UHV for two days. All of the images are 100×100 nm^2, $I_t = 0.08 \sim 0.10$ nA; $V_t = 2.02 \sim 2.15$ V.*

5.4 Summary

Upon being deposited on $Cu_2O/Cu(111)$, potassium is oxidized and the row structure of $Cu_2O/Cu(111)$ is destroyed. The structure of reoxidized potassium modified surface depends on the coverage of potassium. At medium potassium coverage, a quasi-square structure is formed due to distortion of hexagonal ring structure. The domain boundary is composed of five membered and seven membered rings.

Potassium modified $Cu_2O/Cu(111)$ model catalysts under ambient pressures of CO and H_2 at 300 K were studied by AP-STM, AP-IRRAS and AP-XPS. In terms of reduction by CO, potassium is a huge promoter, because potassium related sites are active sites for the reduction. After reduction, metallic copper islands are separated by domains of potassium carbonate. In terms of reduction by H_2, potassium is an inhibitor. Potassium oxide prolongs the time for a complete reduction. Reaction occurs on the step edge sites and on terrace. During the reduction, potassium modified copper oxide demonstrates high mobility under 2.16 Torr of H_2.

The reduction process of $CeO_2/Cu_2O/Cu(111)$ by ambient pressures of H_2 at 300 K was studied by AP-STM. Ce^{4+} is more reactive than Cu^+ towards hydrogenation. Metallic copper forms at step edges and CeO_x clusters, and propagates by mass transfer. After full reduction, ceria islands maintain the same geometry, but clusters of oxygen vacancies form within the islands resulting in a more roughened structure with a concomitant expanded metal-oxide interface, which favors methanol synthesis from CO_2. Adding potassium to $CeO_2/Cu_2O/Cu(111)$ also prolongs the reduction process by H_2 at 300 K. However, metallic potassium related species were firstly observed on step edges or metal-oxide interfaces on $Ce_2O_3/Cu(111)$. It indicates either potassium related molecules are highly mobile on the surface, or metallic potassium atoms on the mentioned sites are more active.

Chapter 6. Redox-mediated Reconstruction of Cu during CO Oxidation

6.1 Introduction

CO oxidation is famous as a prototypical reaction for fundamental research and critical reactions involved in practical applications such as the elimination of automotive exhaust pollution,[171,172] and the reactions discussed in section 1.2. Heterogeneous catalysts, such as noble metals (Pt, Pd, Rh, and Ru)[173] and oxide-supported catalytic materials[174] are conventionally used. In an effort to reduce the high expense of the noble metal catalysts, transition metal oxides[48,175,176] (cobalt oxides and copper oxides) and unsupported/supported transition metals[152,177] (Co, Cr, Cu, Ni, Zn) have been studied as alternatives. Extensive catalytic and kinetic studies have been conducted on the CO oxidation over Cu-based catalysts.[178-182] It was reported that for Cu thin films, the activity decreases as the degree of oxidation increases.[182] Based on research on powder catalysts, it has been suggested that Cu^+ is the most active sites,[48] which contradicts the Cu thin film results mentioned above. An even more extensive research exists on CO oxidation over Pt-group catalysts[183] (and references therein), where the oxidation state of the most active phase has similarly been widely debated.

Different mechanisms have been suggested for CO oxidation on metal and metal oxides. For CO oxidation on Cu(111), the Langmuir-Hinshelwood mechanism has been predicted theoretically.[184] The adsorbed CO and neighboring dissociated oxygen react to form CO_2. For CO oxidation on Cu_2O, based on theoretical studies on $Cu_2O(100)$,[185] Mars-van Krevelen mechanism is predicted. CO molecules react with oxygen from Cu_2O to form CO_2 which desorbs from the surface. The oxygen vacancies are refilled by the dissociation of oxygen from gas phase,[185] or by oxygen diffusion from subsurface layers.[186] However, DFT calculations of CO oxidation on $Cu_2O(111)$[187] suggest that Mars-van Krevelen mechanism is unlikely to occur due to a large barrier. Instead, Eley–Rideal mechanism is most favorable, that is, gas phase CO reacts with adsorbed O_2 to form CO_2. Langmuir–Hinshelwood mechanism is also possible, that is, both adsorbed CO and O_2 react to form CO_2 via an intermediate of $OOCO_{ad}$.

Additionally, the facile oxidation of copper limits the possibility of maintaining a single phase of copper or copper oxides during CO oxidation reaction. Thus, it is very important to study the reaction surfaces which convey direct information about mechanisms and active phases. Traditionally, either ex situ measurements post high pressure expriments,[182] or in situ measurements under vacuum conditions[177] are made. Morphological studies of the substrate and adsorbates have been conducted on oxygen pre-adsorbed Cu(110) using scanning tunneling microscopy (STM) during CO oxidation.[177,188,189] It shows that defects on the oxygen $p(2\times1)$ overlayer structure and step edges are active sites, and the reduction proceeds rapidly along oxygen rows. Oxygen defects are filled by gas phase oxygen, and reduced Cu atoms aggregate at step edges.[177] A STM study was conducted on oxygen pre-treated Pt(111). As 10^{-8} Torr CO was introduced, CO adsorption regions form, and the pre-adsorbed oxygen regions compress and disappear as CO oxidation occurs at the boundaries between the two regions.[190]

Furthermore, the topographies and catalytic activities of heterogeneous metal-based catalysts have been reported to behave differently under high vacuum as compared to high pressure.[28,34,35,37,54,60] Herein, we report an in situ ambient pressure study of CO oxidation over model catalyst Cu(111), the most common and thermally stable facet of Cu, by AP-STM, infrared reflection absorption spectroscopy (IRRAS), and X-ray photoelectron spectroscopy (XPS), to elucidate the activity for CO oxidation on metallic copper and Cu_2O films and reconcile previous conflicting reports in the literature.

6.2 Experimental Methods

A SPECS™ Aarhus 150 HT STM chamber with a high pressure cell was used for imaging experiments, with a base pressure of 5×10^{-10} Torr. A Cu(111) single crystal (Princeton Scientific Corp.) was prepared by consecutive Ar^+ sputtering (5 μA, 2 keV, 20 min) and annealing (800 K, 10 min) cleaning cycles. The high pressure cell is housed inside of a vacuum chamber, and was sealed during the experiments to protect the main chamber ultra-high vacuum (UHV) pressures. Images were recorded using an etched tungsten tip with a constant current imaging mode. High purity CO (GTS-WELCO, 99.999%) and O_2 (GTS-WELCO, 99.9999%) gases were further purified in liquid nitrogen traps prior to being dosed into the high pressure cell. *In situ* AP-IRRAS experiments were carried out in an elevated pressure reactor combined with an UHV surface analysis chamber.[80] Both the STM and IRRAS chambers are housed in the chemistry department at Brookhaven National Lab. *In situ* AP-XPS experiments were performed in a SPECS™ XPS with a PHOIBOS 150 AP analyzer[29] at beamline I511-1,[191] at the MAX II storage ring at MAX Lab in Lund University, Sweden.

6.3 Results and Discussion

6.3.1 In situ reaction of carbon monoxide and oxygen on Cu(111)

In situ AP-IRRAS and AP-XPS were used to study the surface of Cu(111) under CO oxidation reaction conditions at 300 K (Figure 6.1). CO is used as a probe molecule in IR experiments due to its high sensitivity to the oxidation state of adsorption sites, in particular on well-defined single crystals such as Cu(111).[81,192] Table 6.1 summarizes the IR assignments for CO adsorption on various Cu environments.

		Coordination Number	λ^{-1} (cm^{-1})	Ref.
Metal phase	Cu(111)	9	2071	81,82,193
	Cu(100)	8	2085	82,194
	Cu(110)	7	2091	82,194
	Cu(211)	6	2100	40
	Cu/SiO$_2$/Mo(110)	Nanoparticle	2106	195
Oxide phase	Cu$_2$O(111)	Well-ordered	2098	39
	Cu$_2$O	Disordered	2115	40,41 present work
	CuO	Disordered	2148	present work

Table 6.1 *CO stretch frequencies in infrared spectra on copper sites.*

At 300 K and 30 mTorr of CO, a gas phase CO peak is present in the IRRAS data (black spectrum at the top of Figure 6.1A). Upon the addition of 15 mTorr O$_2$, two CO adsorption peaks appear at 2103 and 2115 cm^{-1}, which are assigned to CO adsorption on under-coordinated Cu sties and on disordered Cu$_2$O,[196,197] respectively. The former assignment is based on the reported stretching frequency of CO adsorption on under-coordinated a-top Cu atoms of high index single crystals [2100 cm^{-1} for Cu(211) and 2102 cm^{-1} for Cu(311)[194]] and on small Cu nanoparticles 2106 cm^{-1}.[195] CO adsorption on a well-ordered Cu$_2$O/Cu(111) presents a feature at 2098 cm^{-1},[198] but this feature blue shifts on disordered Cu$_2$O structures above 2110 cm^{-1}.[41] The Cu$_2$O/Cu(111) well-ordered phase requires further annealing at elevated temperatures, and is not present in the

current experiments carried at 300 K. Another evidence pointing to the assignment of the 2103 cm^{-1} peak as CO adsorption on under-coordinated Cu sites is that it disappears in Figure 6.1 under longer exposure to O_2. With longer exposures to oxygen, the Cu is further oxidized, resulting in an increased intensity of the peak at 2115 cm^{-1}. The peak at 2148 cm^{-1} is assigned to CO adsorption on Cu^{2+} sites, where the CO stretching frequency is similar to the results reported on fully oxidized Ru(001)[199] and Pd(100).[183] The CuO film has not been reported to form under UHV conditions, but it can be stabilized under elevated pressure and temperature conditions.[50] The growth of the peak associated with the presence of CuO slows down after 8.0 min of the reaction, corresponding to a decrease in the reaction rate, i.e., the total pressure drop rate in the inset in Figure 6.1A. The results agree with literature that CuO is less active as compared to Cu_2O for the CO oxidation reaction.[200] Noting that the IRRAS peak intensities relate to the absorption cross section of the particular vibrational mode as well as the orientation and coverage of the species, the higher intensity of the peak at 2148 cm^{-1} as compared to the peak at 2115 cm^{-1} does not guarantee the presence of more CO adsorbed onto CuO than Cu_2O.

In the corresponding XPS data in Figure 6.1B, the O 1s peak at 537.5 eV is assigned to gas phase CO[201] and is the only observed peak under 22 mTorr CO. Upon the addition of 11 mTorr O_2, several new peaks are observed. Peaks at 538.3 and 539.3 eV correspond to gas phase O_2.[202] Under CO oxidation conditions on Cu(111) at 300 K, the oxidation of the surface was observed in the O 1s region, as peaks are observed for CuO (at 528.9 eV),[50] Cu_2O (at 529.9 eV)[50] and surface oxygen (at 530.9 eV),[202] which is in agreement with the formation of CuO and Cu_2O deduced from the IRRAS data. According to the XPS peak intensities, Cu_2O is the majority oxide species that forms. The broad feature at ~4 eV above the Cu_2O signal matches data collected upon adsorption of CO on Cu_2O(111) at low temperature (data not shown). Upon

evacuation of the cell, the sample was moved to UHV conditions and the three peaks (at 530.9, 529.9, and 528.9 eV) were still observed, showing that all the three oxide phases exist in UHV. By comparing the relative peak intensity in situ and under UHV conditions, it is observed that CuO partially decomposes under vacuum.
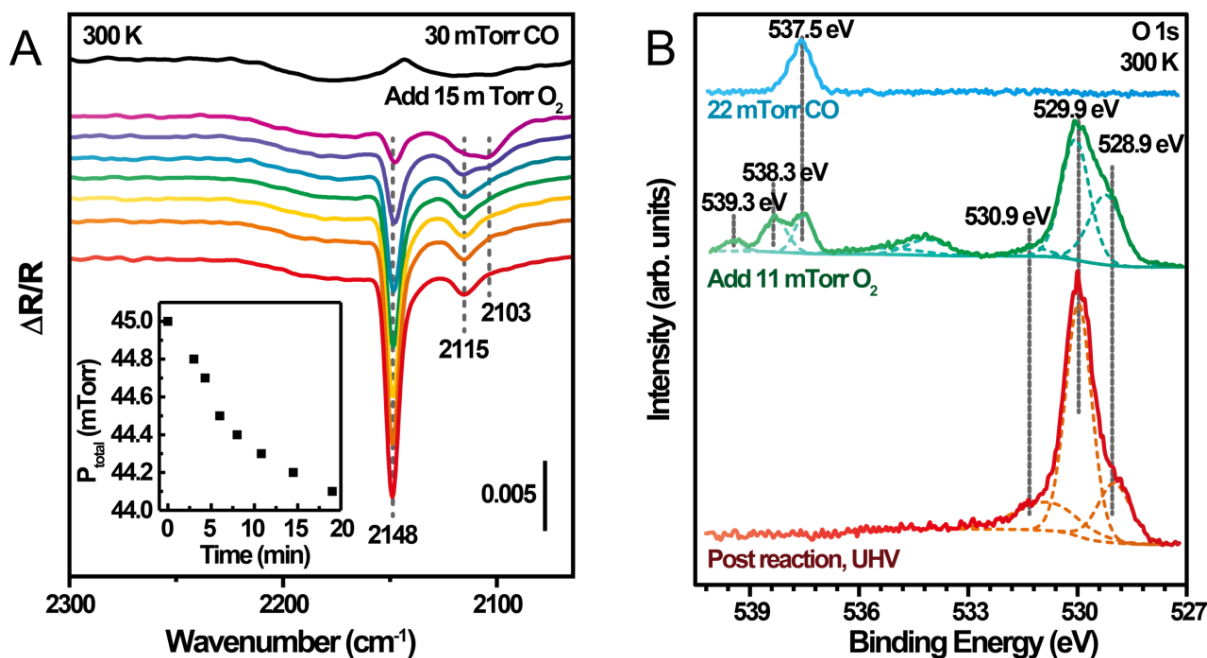
Figure 6.1 *In situ spectroscopic data for CO oxidation (CO:O_2 = 2:1) over Cu(111) at 300 K. A) AP-IRRAS results. The top spectrum shows Cu(111) exposure to 30 mTorr CO, and the following spectra correspond to reaction times of 3.0 min, 4.3 min, 6.0 min, 8.0 min, 10.8 min, 14.5 min and 19.0 min. The total pressure as a function of reaction time is plotted in the insert. B) AP-XPS results. O 1s spectra were obtained after exposure of Cu(111) to CO (top), CO + O_2 (middle), and after evacuation of the AP cell (bottom).*

The topographical changes of the Cu(111) model catalyst were captured via AP-STM in situ imaging, under a similar condition in Figure 6.1, Figure 6.2. All images were recorded with the scanning direction from the bottom to the top of the image. Figure 6.2A shows an as-prepared clean Cu(111) surface with one step edge. At the bottom of Figure 6.2B, a valve was opened to fill the high pressure cell with the 2:1 CO and O_2 gas mixture as horizontal noises appear from opening the gas valve. Upon exposure of the Cu surface to CO and O_2, structural

changes are observed at the step edge, as seen in the top of Figure 6.2B and more evidently in Figure 6.2C. The changes observed in Figures 6.2B and 6.2C correspond to the initial oxidation of the Cu surface, similar to the initial oxidation of Cu(111) under pure oxygen pressures.[52,76,203] Furthermore, the disordered oxide that forms on Cu(111) at 300 K is active for oxidation reactions, as shown by STM via the oxidation of methanol.[204] In figure 6.2C, the oxidation occurs at the step edges, forming a step oxide,[52] and the step edges begin to facet[76] as the oxide forms along the Cu(111) closed packed <110> direction. Less than 1 min after Figure 6.2C, the Cu(111) surface is covered by a disordered structure, as seen in Figures 6.2D and 6.2E. Afterwards, the morphology of the disordered oxide reaches an equilibrium configuration, where only small changes at a local level are observed. It is well known that oxidation of Cu(111) at 300 K leads to a disordered oxide structure[76,203,205], which becomes well-ordered at higher temperatures.[52,54] Figure 6.2 shows the appearance of oxidized Cu in a disordered structure under CO oxidation conditions at 300 K. The oxide structure is stable during the reaction (Figure 6.2D and 6.2E) and post the reaction under vacuum (Figure 6.2F).
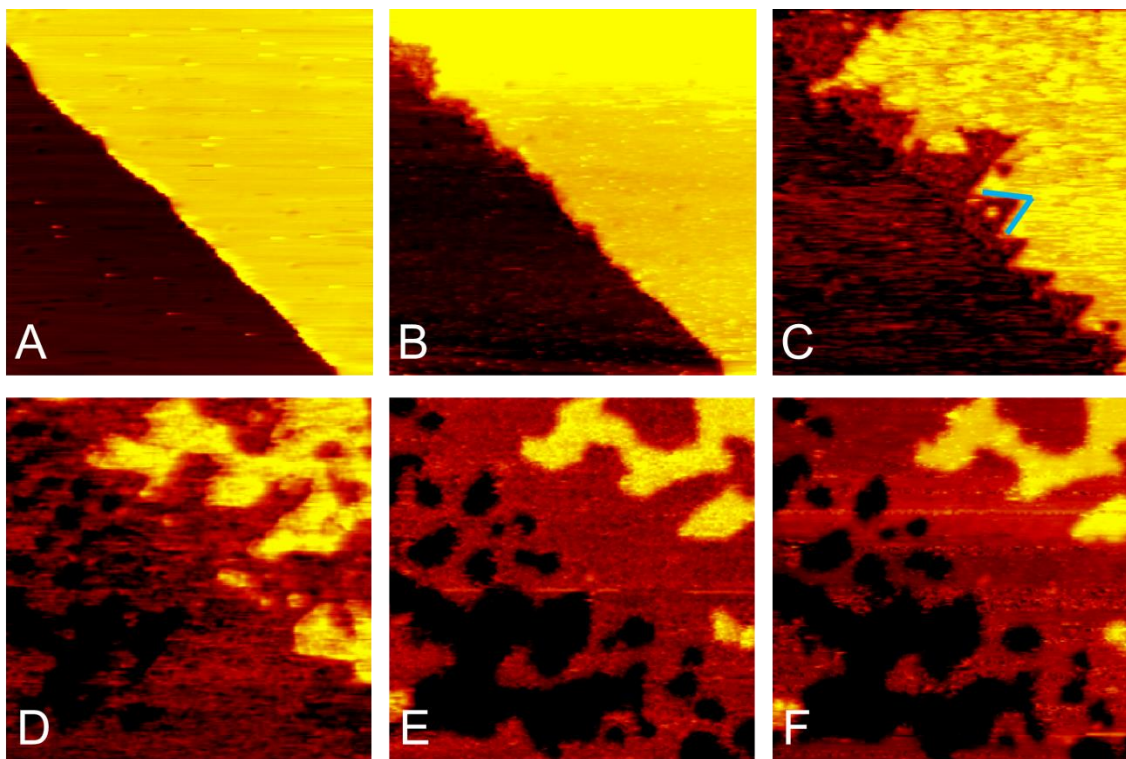
Figure 6.2 *In situ AP-STM images of Cu(111) during 2:1 ratio of CO oxidation (CO:O₂ = 30 mTorr:15 mTorr). Reaction time from A) to E) is 0 min, 0.7 min, 1.5 min, 2.2 min and 20.4 min. Blue lines in C) indicate the close-packed <110> direction. F) shows the surface topography after evacuating the gases for ~1 min. All the images are 45×45 nm². I_t = 0.33~0.37 nA; V_t = 1.36~1.40 V.*

The in situ AP-IRRAS data shown in Figure 6.1 indicate that the reaction rate, or rate of total pressure drop, decreases as the reaction progresses as copper is further oxidized. Even at highly reducing conditions, with a CO:O₂ ratio of ~8:1 and a total pressure of ~34 mTorr, rapid formation of Cu^+ and Cu^{2+} is inevitable at 300 K, as shown in Figure 6.3. At higher temperatures the fast oxidation of Cu dominates the process and translates into larger copper oxide domains on the surface of the catalyst. In the CO oxidation experiments on thin Cu films reported in the literature,[182] a very high reducing CO:O₂ ratio of 97:3 was used to calculate the apparent activation energy for CO oxidation on metallic Cu at temperatures ~550 K. The amorphous thin Cu films likely consist of several facets and domains. Polycrystalline Cu films and open facets

are more reactive and undergo oxidation more rapidly than Cu(111) single crystals. We conducted AP-IRRAS experiments at temperatures and pressures where the adsorption of CO on metallic Cu(111) can be spectroscopically detected. At a $CO:O_2$ ratio of 97:3 and 300 K with a total pressure of 100 mTorr, rapid formation of Cu_2O regions is still detected. Figure 6.3B shows that even under highly reducing conditions with a $CO:O_2$ ratio of 99:1 at 300 K, the introduction of O_2 induces a reconstruction of the surface by successive oxidation-reduction cycles. A background spectrum was taken after exposing the Cu(111) sample to 99 mTorr of CO, which did not change over time. After the addition of 1 mTorr of O_2, a positive feature appeared at 2068 cm^{-1}, indicating the disappearance of CO adsorbed onto Cu^0 due to the adsorption of oxygen on the surface, and a new peak develops over time at 2100 cm^{-1} indicating the formation of under-coordinated Cu sites on the surface.
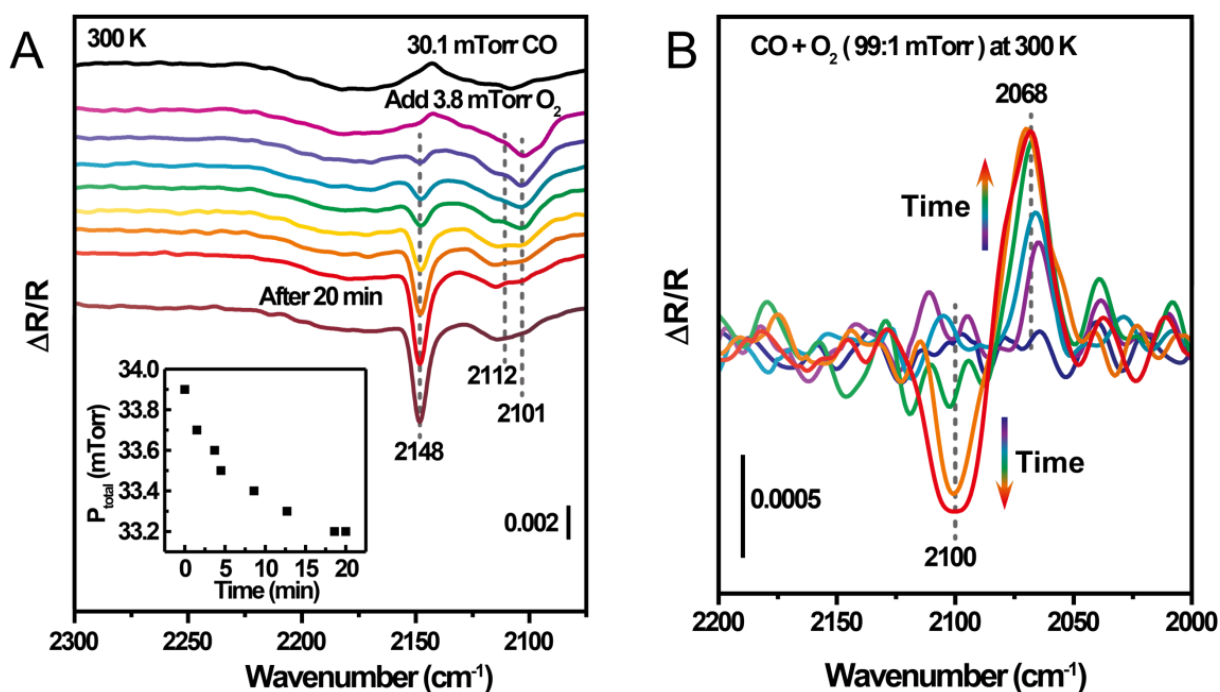
Figure 6.3 In situ IRRAS for CO oxidation over Cu(111) at 300 K. A) $CO:O_2$ = 8:1 (30.1 mTorr:3.8 mTorr); the top spectrum shows exposure to pure CO, and the following spectra were collected in a sequence of time within 20 min. The bottom spectrum was taken after 20 min of reaction. The total pressure change as a function of the reaction time is shown in the insert. B)

104

CO:O$_2$ = 99 mTorr:1 mTorr. Two peaks increase in intensity as a function of time after exposure to CO + O$_2$. Spectra in B) were obtained after subtracting the CO gas phase adsorption peak.

In situ AP-STM figure sets for CO:O$_2$ ratios greater than 2:1 are shown below. In Figure 6.4, changes in the surface morphology are monitored during CO oxidation over Cu(111) at a 3:1 ratio (30 mTorr CO:10 mTorr O$_2$) at 300 K. Figure 6.4A shows an as-prepared clean Cu(111) surface with two step edges highlighted by white dashed lines. CO and O$_2$ were mixed prior to be dosed on the surface. After 3.0 min of reaction, the step edges have retreated as seen in Figure 6.4B and faceted along the close-packed <110> direction, as shown with blue lines in Figure 6.4B and 6.4C. The roughened surface in the vicinity of the original step edge indicates the formation of a disordered oxide, in agreement with Cu(111) oxidation experiments[52] and Figure 6.2. However, in Figures 6.4D and 6.4E, after ~10 min of the reaction, the growth of the roughened oxide regions has slowed down and the appearance of small islands was observed. Similar island growth was observed due to O$_2$ exposure (6×10^{-5} Torr) on a Cu(100) surface at 373 K, and the islands were assigned as Cu$_2$O, which facilitate oxygen penetrating to the subsurface.[206]
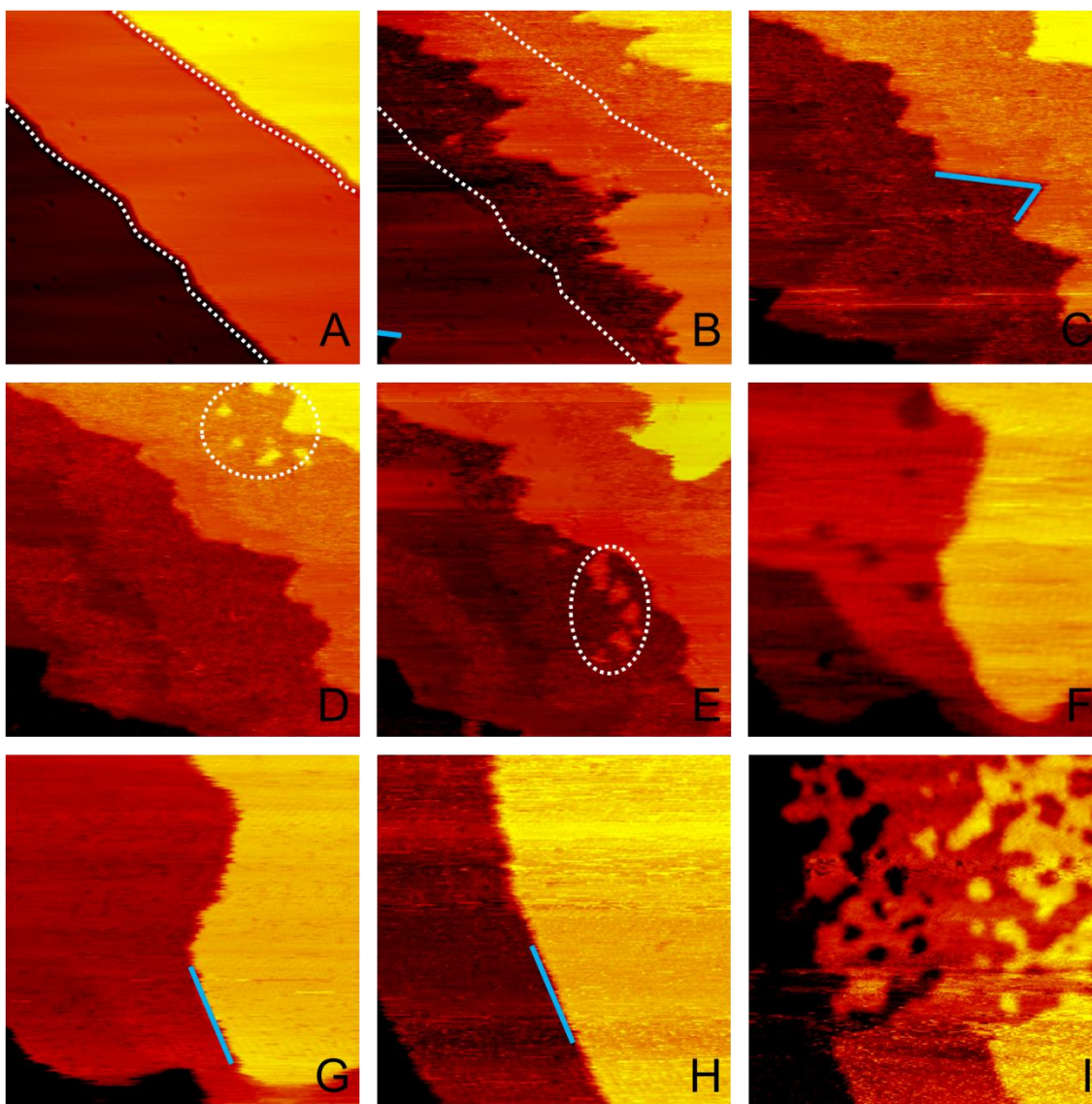
Figure 6.4 *In situ AP-STM images during CO oxidation (CO:O_2 = 30 mTorr:10 mTorr) on Cu(111) at 300 K. Blue lines indicate the close-packed <110> direction. Reaction time from A) to H) is: 0 min, 3.0 min, 6.0 min, 9.0 min, 12.1 min, 24.5 min, 26.6 min and 50.1 min, respectively. White dashed lines in A) and B) indicate the original step edge. White circles in D) and E) highlight newly formed islands. The gases were evacuated in the middle of I). All the images are 45×45 nm^2. I_t = 0.37~0.46 nA; V_t = 1.32~1.44 V.*

In Figure 6.4D, the height difference between the small islands and adjacent terraces is 2.1 ± 0.1 Å, corresponding to the height of a single metallic Cu layer. Similar Cu islands were observed during the in situ Cu_2O/Cu(111) reduction by CO due to the aggregation of reduced Cu atoms.[60] The formation of Cu islands (indicated by white circles) in Figure 6.4D and the

subsequent disappearance in Figure 6.4E indicates a cycle between oxidized and reduced domains. It is important to mention that during CO oxidation over Pt and Pd single crystals, nonlinear chemical oscillation has long been reported in open systems, where a constant flow is applied and thermodynamic equilibrium is not reached.[207,208] In Figures 6.4G and 6.4H, the terraces continue to grow, without the appearance of islands, and the step edges are faceted along the Cu <110> direction (blue lines). STM images show that pure CO at this pressure does not facilitate the faceting of Cu step edges along the <110> direction at 300 K (section 3.3.1), whereas O_2 alone oxidizes the Cu and forms stable but amorphous structures (section 3.3.2). Previous AP-STM experiments show the highly mobility of released Cu atoms during Cu_2O/Cu(111) reduction by CO.[60] Thus, we propose that, during CO oxidation on Cu(111) with $CO:O_2$ = 30 mTorr:10 mTorr at 300 K, Cu is oxidized locally on Cu terraces in the early stages of the reaction,[200,206] and is then reduced to Cu. During the redox cycle, the released highly mobile Cu atoms diffuse on the surface, resulting in the movement of step. Upon evacuating the gases in the bottom of Figure 6.4I, the surface immediately appears pitted (at the top of Figure 6.4I), which is similar to the copper oxide structure observed in Figure 6.2F. Since CO has a smaller sticking coefficient than O_2, any oxygen remaining in the system readily oxidizes the Cu surface. The pitted structure is stable under UHV conditions at 300 K.

Figure 6.5 shows AP-STM results from CO oxidation over Cu(111) at 300 K with an increased $CO:O_2$ ratio to 4:1 (32 mTorr:8 mTorr). After 8.2 min of exposure, all of the step edges appear etched in Figure 6.5B compared with the as-prepared surface in Figure 6.5A, as was observed under the 3:1 ratio in Figure 6.4B. With another 4 min of reaction, a highly resolved image shows the Cu terraces with low mobility point defects (depressions) and ring structures, Figure 6.5C and its insert. The point defects can be chemisorbed oxygens on Cu. The ring

structures, with a height of 0.6 ± 0.1 Å, are most likely added oxide in section 3.3.2 composed of Cu_2O-hex/5-7 rings,[56,60] and surface oxygens.[52] Blue lines indicate the <110> direction which the faceted of step edges adopt. As the reaction progresses from Figure 6.5C to Figure 6.5G, the step edges of terraces translate to a faceted direction along <110> (Figure 6.5G), and the copper oxide ring structure gradually disappears and islands appear with random (Figure 6.5C) and hexagonal (Figure 6.5F) shapes. The height of the islands matches that of a single Cu layer, 2.1 ± 0.1 Å, similar to the islands in Figure 6.4D. From Figure 6.5F to 6.5G, the terrace structure remains the same as the step edge changes, similar to what is observed in Figure 4. Upon the evacuation of the gas mixture in Figure 6.5H, a pitted oxide surface forms, which then decomposes within 4 min of evacuation (Figure 6.5I) unlike the stable copper oxide formed in Figure 4I. It shows that the oxide domains formed under the 4:1 ratio are not as stable under vacuum conditions as those formed under more oxidizing conditions (2:1 and 3:1 ratios).
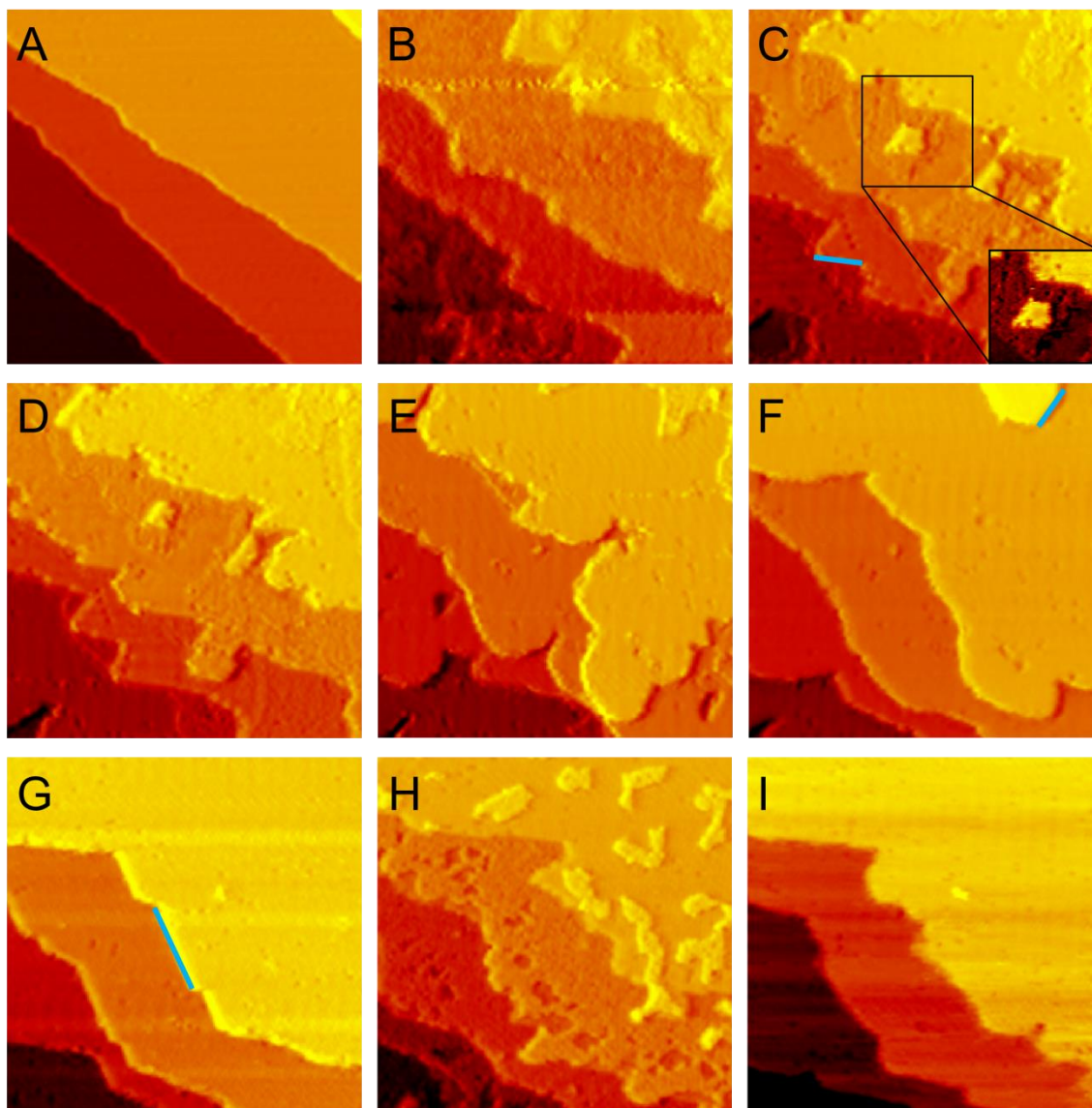
Figure 6.5 *In situ AP-STM images during CO oxidation (4:1, 32 mTorr CO:8 mTorr O₂) on Cu(111) at 300 K. Blue lines indicate the Cu(111) close-packed <110> directions. Reaction time from A) to G) is: 0 min, 8.2 min, 12.3 min, 14.4 min, 18.6 min, 27.0 min and 77.2 min, respectively. The inset of C) shows the ring structure of highlighted on the terrace with a better color contrast. H) Upon evacuating the gas mixture. I) 4.2 min after the evacuation. All the images are 45×45 nm². $I_t = 0.36\sim0.45$ nA; $V_t = 1.27\sim1.48$ V.*

The combined spectroscopic and microscopic in situ studies of the CO oxidation on a copper surface at 300 K clearly establish the difficulty of preparing homogeneous phases of a given oxide domain to establish the most active phases in a system. This may be the source of the controversy in the literatures with respect to the relative activity among Cu^0, Cu^+ and

Cu^{2+}.[48,171,182] Metallic copper, due to its easy oxidation, is the most difficult phase to isolate for determining catalytic activity. It has been predicted theoretically that the rate limiting step in the oxidation of CO on Cu(111) is not the dissociation of molecular oxygen, like in Pt-group metals, but instead the last step of the reaction *e.g.* $CO_{ad} + O_{ad} \rightarrow CO_2$.[209] To study this last step we carried out similar experiments to the ones reported on the oxidation of CO on Pt(111) by Ertl, *et. al.*[190] CO desorbs from Cu(111) at 160 K, a lower temperature than on Pt(111).[81] However, when the sample is pressurized with 1.0 mTorr, CO adsorption on clean metallic Cu(111) can be detected in equilibrium with the gas phase up to 250 K. A chemisorbed oxygen saturated surface was prepared by exposing Cu(111) to 150 Langmuirs of O_2 at 300 K, where the initial formation of under-coordinated Cu sites is observed by the adsorption of a small amount of CO with a peak at 2089 cm^{-1} (Figure 6.6). This oxygen-saturated surface was then exposed to 1.0 mTorr of CO at 200 K and the adsorption of CO on metallic Cu sites (peak at 2069 cm^{-1}) was followed as a function of time as pre-adsorbed oxygen reacting with CO to form CO_2 (Figure 6.6). By carrying out similar experiments to the one shown in Figure 6.6 at various temperatures below 200 K, where the initial rate of CO oxidation was measured, we are able to determine an apparent activation energy for the oxidation of CO on an oxygen-saturated copper surface, E_a(O-Cu) = 0.10 $\pm$ 0.03 eV. We also prepared well-defined Cu_2O/Cu(111) films, and measured their initial rate of reduction at temperatures ~300 K and CO pressures of 1 mTorr. After an initial induction period required for the formation of vacancies, the apparent activation energy for CO oxidation on Cu_2O was measured to be $E_a(Cu_2O)$ = 0.22 $\pm$ 0.01 eV. A previous result on the reduction of oxygen-saturated Cu(111) by CO at ~300 K, which lacked spectroscopic characterization, but based on our current studies may have involved a mixture of Cu^0 and Cu^+ sites, reported an apparent activation energy E_a = 0.15 $\pm$ 0.01 eV, in agreement with an average

value of the two activation energies discussed above.[210] We are not able to prepare homogeneous phases of Cu^{2+} on Cu(111) to test their catalytic activity, but the AP-IRRAS data discussed above shows that the reaction rate is significantly lowered with the formation of large Cu^{2+} domains.
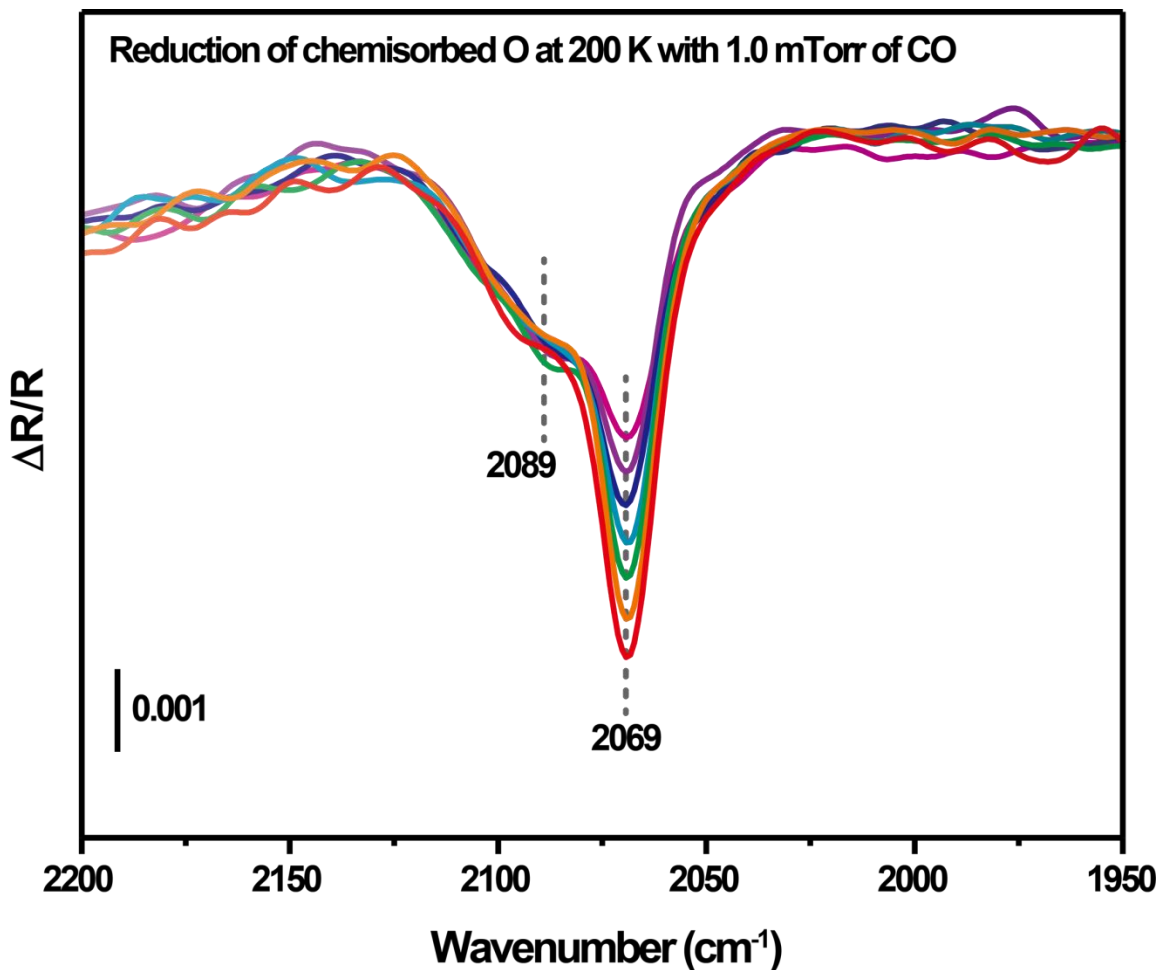
Figure 6.6 *In situ AP-IRRAS of an oxygen-saturated Cu(111) surface reduction by 1.0 mTorr CO at 200 K. The peak at 2089 cm⁻¹ corresponds to a small amount of CO adsorbed on under-coordinated Cu sites, and the increasing in intensity of the peak at 2069 cm⁻¹ over time corresponds to adsorption of CO on Cu(111) sites upon removal of chemisorbed oxygen by formation of CO_2.*

6.3.2 Active phase of copper during carbon monoxide oxidation

According to the in situ data discussed above, the surface of copper catalysts under CO oxidation conditions is heterogeneous and in general consists of all possible Cu oxidation states.

111

In the stoichiometric case of the 2:1 ($CO:O_2$) ratio, the Cu(111) surface was oxidized to a relatively static structure, on which CO oxidation may partially proceed through a Mars-van Krevelen mechanism,[187] where CO reacts with lattice oxygen and then O_2 fills in O vacancies instantly to protect the surface from reduction. Under more reducing conditions the surface structure is very dynamic and undergoes reconstructions related to the oxidation/reduction of copper metal/oxide domains. The increase of surface mobility is due to released Cu atoms from the redox cycle, to which CO can bind at room temperature and aid Cu diffusion.[60] The released Cu atoms form faceted step edges to minimize surface energy. Metallic copper is the most efficient phase for the oxidation of CO via a Langmuir-Hinshelwood pathway. Although the reported overall CO oxidation activity of noble-based catalysts is better than that of copper-based catalysts, the apparent activation energy for the process on metallic copper is the lowest reported in the literature, compared with values of 0.5 eV on Pt(111)[190] and Ru(001).[199] The previously reported higher value for Cu films of 0.4 eV[182] was most likely due to the presence of less efficient Cu^+ and Cu^{2+} regions. The trend in the efficiency for the oxidation of CO is $Cu^0 > Cu^+ > Cu^{2+}$, which agrees with the trend observed on Pt-group materials.[183]

6.4 Summary

By using a complementary set of in situ microscopic and spectroscopic techniques, a clear picture of the dynamic nature of the surface of copper catalysts during the oxidation of CO at 300 K has been obtained. Copper oxide domains form even under heavily reducing conditions, and the surface reconstructs constantly through a redox cycle between CuO, Cu_2O and Cu. The Cu atoms released during the redox cycle diffuse to the step edges leading to a flat surface with highly mobile step edges that are faceted along the <110> directions. Metallic copper is the most

active phase, but it cannot be stabilized under reaction conditions. Cu^+ is also very active, more active than Pt-group metals at 300 K, and the formation of Cu^{2+} deactivates the catalysts. Strategies to stabilize structures with Cu^+ cations, such as the formation of mixed-oxides,[198] could lead to very efficient and stable oxidation catalysts.

Chapter 7. Summary

Copper-based materials are widely used heterogeneous catalysts in various important catalytic reactions that are related to fuels and energy. For industrial production processes, powder catalysts are typically used at pressures above one atmosphere and temperatures of several hundred degrees. Although it's easy to measure activity under these conditions, it's very difficult to investigate dynamic transformations and reaction mechanism that occur mostly on the solid-gas interface. Additionally, powder catalysts are challenging for well-defined studies due to their complexity of multi components and structures. Thus, Cu-base model catalysts can be synthesized for advancing our understanding of reaction mechanisms down to the atomic level. Typical model catalysts are made of a single surface from many in a powder, such as Cu(111), Cu(110) and Cu(100), etc. The Cu-based model catalysts are prepared and stored under ultra-high vacuum (UHV, pressure less than 10^{-9} Torr) conditions in order to have a clean and well-defined environment. Conventionally, reactions on model catalysts are conducted at pressures less than 10^{-5} Torr, which leads to an obvious pressure gap compared to commercial production conditions. Thus, this dissertation is focused on in situ studies on Cu-based model catalysts to investigate surface dynamic transformations under ambient pressures (AP), typically 10^{-3}-10^{2} Torr, using STM, IRRAS and XPS, which more closely resemble the high pressure conditions of real catalytic processes.

It is known that CO desorbs from Cu(111) below 200 K. However, when the pressure is increased above 64 mTorr, CO adsorption on Cu(111) can be detected. Due to the easy formation of carbonyl as an impurity within a high pressure CO tank, hexagonal patterns with different spacing are observed on Cu(111) that are derived from these carbonyl species. High pressures also facilitate O_2 adsorption on Cu(111) with a formation of amorphous copper oxides. For both gases, adsorption at ambient pressures at 300 K leads to a roughened surface, which is irreversible after evacuating the gases. The topography of pitted Cu(111) surfaces with exposed under‑coordinated sites can also be changed under ambient pressure of CO, H_2 or low pressure atomic H. The trend in the ability to modify a pitted Cu(111) surface by interaction with reducing species is H > CO > H_2. Atomic H forms a sub-surface copper hydride, which is not stable at 300 K. Copper atoms fully relax to give a smooth surface during the H recombination and desorption process. Ambient pressure CO can weakly bind to Cu atoms and facilitate their diffusion. Dissociate of H_2 can also occur on Cu(111), but the lifetime of dissociated H is short before it recombines and desorbs as H_2. Thus, ambient pressures of H_2 barely affect the topography of Cu(111).

Well defined Cu_2O/Cu(111) thin films are model catalysts for cuprous oxide. The reduction processes induced by ambient pressures of CO and H_2, two important gases for copper-based catalysts, are studied at 300 K. Both CO and H_2 can reduce Cu_2O/Cu(111) to the intermediate Cu_2O-hex/5-7 ring structure and metallic copper. The released copper atoms diffuse on the terrace and join nearby Cu step edges by mass transfer. CO reduces Cu_2O/Cu(111) following Mars-van Krevelen mechanism, where CO directly reacts with lattice oxygen to form CO_2. The reduction initiates at defects on terraces or step edges. On the other hand, reduction by H_2 is orders of magnitudes slower than that by CO. Mechanisms for Cu_2O/Cu(111) reduction by

H$_2$ is complex and multiple steps are involved including H$_2$ dissociation, hydroxyl formation, water formation. The reduction is only observed to initiate on step edges, after a long induction period. Metallic copper grows towards a descending step edge direction, since the copper step edge is a source of rapidly diffused under-coordinated atoms which greatly facilitates hydrogen dissociation. Based on reduction experiments at various temperatures, the apparent activation energies for Cu$_2$O/Cu(111) reduction by CO and H$_2$ are 0.22 eV and 0.75 eV, respectively.

Potassium and cerium can be added to the Cu$_2$O/Cu(111) as catalytic modifiers. Upon being deposited on Cu$_2$O/Cu(111), metallic potassium is oxidized while Cu$_2$O/Cu(111) is slightly reduced. Potassium related sites are clearly identified and well dispersed across the surface. The surface regained flatness after reoxidation with potassium sites invisible by STM. Potassium related species are active sites for Cu$_2$O/Cu(111) reduction by ambient pressures CO at 300 K by forming potassium carbonate, thus greatly facilitating the reduction. However, the potassium related species prohibit Cu$_2$O/Cu(111) reduction by ambient pressures of H$_2$ at 300 K. Ceria islands were prepared on Cu$_2$O/Cu(111), and its reduction process was followed by ambient pressure H$_2$. The hydrogenation occurs on ceria islands first, then on Cu$_2$O/Cu(111) thin films, as indicated by STM. The metal-oxide interface is not the initial reactive site for forming Cu. After reduction, the metal-oxide interface is expanded. Adding potassium to CeO$_2$/Cu$_2$O/Cu(111) does not facilitate the hydrogenation process. When potassium is deposited on the reduced metal-oxide interface, the reacted potassium firstly appears around metal-oxide interfaces.

Finally, ambient pressure CO oxidation was studied on Cu(111) at 300 K. Cu(111) is easily oxidized to Cu$^+$ and Cu^{2+} during the reaction, even with a high CO to O$_2$ ratio. The reduction follows redox cycles and the released Cu atoms form faceted step edges along the <110> directions. The co-existence of multiple Cu-phases complicates the calculation of

activation energies for each phase, i.e., Cu/metallic, Cu_2O, CuO. After calculating the corresponding apparent activation energies of the rate determine step of CO oxidation on Cu^0 and Cu^+, and combining activity results, the activity for CO oxidation is found to be $Cu^0 > Cu^+ > Cu^{2+}$. Though being most active, metallic copper is readily oxidized during CO oxidation. One possible strategy to obtain desirable stability and activity for CO oxidation is to stabilize the active Cu^+ phase, such as embedding Cu^+ in a mixed oxide.

In summary, this dissertation has demonstrated that ambient pressure techniques, especially AP-STM, are very powerful in identifying atomic/near atomic surface dynamic transformations on model copper-based catalysts in order to bridge the pressure gap with real catalysts. Such ambient pressure STM studies are relatively rare, due to the instrumental challenges, thus work in this dissertation is pioneering. Future topics for ambient pressure studies on copper-based model systems may include more complex materials and harsher conditions with high temperature. For example, mixed oxide or two or more supported metal particles can be built as the model catalysts; two or more reactant gasses may be introduced on model surfaces to investigate surface properties under catalytic reactions, such as water-gas shift reaction and methanol synthesis from CO_2.

References

(1)   Berzelius, J. J. *Annal Chim Phys* **1836**, *61*, 146.

(2)   Stiles, A. B.; Chen, F.; Harrison, J. B.; Hu, X. D.; Storm, D. A.; Yang, H. X. *Industrial & Engineering Chemistry Research* **1991**, *30*, 811.

(3)   Clark, J. 2002.

(4)   Apodaca, L. E.; Jan, 2016 ed.; U.S. Geological Survey: 2016.

(5)   NGI's shale Daily: 2013.

(6)   Perez-Ramirez, J.; Mondelli, C.; Schmidt, T.; Schluter, O. F. K.; Wolf, A.; Mleczko, L.; Dreier, T. *Energy Environ. Sci.* **2011**, *4*, 4786.

(7)   Bell, A. T. *Science* **2003**, *299*, 1688.

(8)   Behrens, M.; Studt, F.; Kasatkin, I.; Kuhl, S.; Havecker, M.; Abild-Pedersen, F.; Zander, S.; Girgsdies, F.; Kurr, P.; Kniep, B. L.; Tovar, M.; Fischer, R. W.; Norskov, J. K.; Schlogl, R. *Science* **2012**, *336*, 893.

(9)   Gupta, M.; Smith, M. L.; Spivey, J. J. *ACS Catal.* **2011**, *1*, 641.

(10)   Rodriguez, J. A.; Graciani, J.; Evans, J.; Park, J. B.; Yang, F.; Stacchiola, D.; Senanayake, S. D.; Ma, S. G.; Perez, M.; Liu, P.; Sanz, J. F.; Hrbek, J. *Angew. Chem. Int. Ed.* **2009**, *48*, 8047.

(11)   Rodriguez, J. A.; Ma, S.; Liu, P.; Hrbek, J.; Evans, J.; Perez, M. *Science* **2007**, *318*, 1757.

(12)   Wainwright, M. S.; Trimm, D. L. *Catal. Today* **1995**, *23*, 29.

(13)   Kyriakou, G.; Boucher, M. B.; Jewell, A. D.; Lewis, E. A.; Lawton, T. J.; Baber, A. E.; Tierney, H. L.; Flytzani-Stephanopoulos, M.; Sykes, E. C. H. *Science* **2012**, *335*, 1209.

(14)   Mond, L.; Langer, C.; Quincke, F. *Journal of the Chemical Society, Transactions* **1890**, *57*, 749.

(15)   Poutsma, M. L.; Elek, L. F.; Ibarbia, P. A.; Risch, A. P.; Rabo, J. A. *J. Catal.* **1978**, *52*, 157.

(16)   Iwasa, N.; Kudo, S.; Takahashi, H.; Masuda, S.; Takezawa, N. *Catal. Lett.* **1993**, *19*, 211.

(17)   Graciani, J.; Mudiyanselage, K.; Xu, F.; Baber, A. E.; Evans, J.; Senanayake, S. D.; Stacchiola, D. J.; Liu, P.; Hrbek, J.; Sanz, J. F.; Rodriguez, J. A. *Science* **2014**, *345*, 546.

(18)   Hagen, J. *Industrial Catalysis: A Practical Approach*; Wiley: New York, 2006.

(19)   Bartholomew, C. H.; Farrauto, R. J. *Fundamentals of Industrial Catalytic Processes*; second ed. ed.; AICHE-Wiley: New York, 2005.

(20)   Liu, Y. Y.; Hayakawa, T.; Tsunoda, T.; Suzuki, K.; Hamakawa, S.; Murata, K.; Shiozaki, R.; Ishii, T.; Kumagai, M. *Top. Catal.* **2003**, *22*, 205.

(21)   Thomas, J. M. T. W. J. *Principles and Practice of Heterogeneous Catalysis*; VCH: Weinheim, 1997.

(22)   Hautier, G.; Miglio, A.; Ceder, G.; Rignanese, G. M.; Gonze, X. *Nature Communications* **2013**, *4*, 7.

(23)   Millot, N.; Aymes, D.; Bernard, F.; Niepce, J. C.; Traverse, A.; Bouree, F.; Cheng, B. L.; Perriat, P. *J. Phys. Chem. B* **2003**, *107*, 5740.

(24)   Schoiswohl, J.; Kresse, G.; Surnev, S.; Sock, M.; Ramsey, M. G.; Netzer, F. P. *Phys. Rev. Lett.* **2004**, *92*, 4.

(25)   Yoffe, A. D. *Advances in Physics* **1993**, *42*, 173.

(26)   Rodriguez, J. A.; Hrbek, J. *Surf. Sci.* **2010**, *604*, 241.

(27)   Fernández-García, M.; Martínez-Arias, A.; Hanson, J. C.; Rodriguez, J. A. *Chem. Rev.* **2004**, *104*, 4063.

(28)   Tao, F.; Zhang, S. R.; Nguyen, L.; Zhang, X. Q. *Chem. Soc. Rev.* **2012**, *41*, 7980.

(29)   Schnadt, J.; Knudsen, J.; Andersen, J. N.; Siegbahn, H.; Pietzsch, A.; Hennies, F.; Johansson, N.; Martensson, N.; Ohrwall, G.; Bahr, S.; Mahl, S.; Schaff, O. *J. Synchrotron Radiat.* **2012**, *19*, 701.

(30)   Salmeron, M.; Schlogl, R. *Surf. Sci. Rep.* **2008**, *63*, 169.

(31)   Ozensoy, E.; Meier, D. C.; Goodman, D. W. *The Journal of Physical Chemistry B* **2002**, *106*, 9367.

(32)   Rasmussen, P. B.; Hendriksen, B. L. M.; Zeijlemaker, H.; Ficke, H. G.; Frenken, J. W. M. *Rev. Sci. Instrum.* **1998**, *69*, 3879.

(33)   Jinschek, J. R. *Chem. Commun.* **2014**, *50*, 2696.

(34)   Zhu, Z. W.; Butcher, D. R.; Mao, B. H.; Liu, Z.; Salmeron, M.; Somorjai, G. A. *J. Phys. Chem. C* **2013**, *117*, 2799.

(35)   Nguyen, L.; Cheng, F.; Zhang, S. R.; Tao, F. *J. Phys. Chem. C* **2013**, *117*, 971.

(36)   Vestergaard, E. K.; Vang, R. T.; Knudsen, J.; Pedersen, T. M.; An, T.; Lægsgaard, E.; Stensgaard, I.; Hammer, B.; Besenbacher, F. *Phys. Rev. Lett.* **2005**, *95*, 126101.

(37)   Zafeiratos, S.; Piccinin, S.; Teschner, D. *Catal. Sci. Tech.* **2012**, *2*, 1787.

(38)   Helveg, S.; Lopez-Cartes, C.; Sehested, J.; Hansen, P. L.; Clausen, B. S.; Rostrup-Nielsen, J. R.; Abild-Pedersen, F.; Norskov, J. K. *Nature* **2004**, *427*, 426.

(39)   Hansen, P. L.; Wagner, J. B.; Helveg, S.; Rostrup-Nielsen, J. R.; Clausen, B. S.; Topsoe, H. *Science* **2002**, *295*, 2053.

(40)   Kuwauchi, Y.; Takeda, S.; Yoshida, H.; Sun, K.; Haruta, M.; Kohno, H. *Nano Lett.* **2013**, *13*, 3073.

(41)   Montano, M.; Tang, D. C.; Somorjai, G. A. *Catal. Lett.* **2006**, *107*, 131.

(42)   Rodriguez, J. A.; Liu, P.; Wang, X.; Wen, W.; Hanson, J.; Hrbek, J.; Perez, M.; Evans, J. *Catal. Today* **2009**, *143*, 45.

(43)   Mudiyanselage, K.; Senanayake, S. D.; Feria, L.; Kundu, S.; Baber, A. E.; Graciani, J.; Vidal, A. B.; Agnoli, S.; Evans, J.; Chang, R.; Axnanda, S.; Liu, Z.; Sanz, J. F.; Liu, P.; Rodriguez, J. A.; Stacchiola, D. J. *Angew. Chem. Int. Ed.* **2013**, *52*, 5101.

(44)   Liu, Y.; Fu, Q.; Flytzani-Stephanopoulos, M. *Catal. Today* **2004**, *93-5*, 241.

(45)   Kugai, J.; Moriya, T.; Seino, S.; Nakagawa, T.; Ohkubo, Y.; Nitani, H.; Mizukoshi, Y.; Yamamoto, T. A. *Appl. Catal., B* **2012**, *126*, 306.

(46)   Han, J.; Kim, H. J.; Yoon, S.; Lee, H. *J. Mol. Catal. A: Chem.* **2011**, *335*, 82.

(47)   Eren, B.; Lichtenstein, L.; Wu, C. H.; Bluhm, H.; Somorjai, G. A.; Salmeron, M. *The Journal of Physical Chemistry C* **2015**, *119*, 14669.

(48)   Huang, T. J.; Tsai, D. H. *Catal. Lett.* **2003**, *87*, 173.

(49)   Simson, G.; Prasetyo, E.; Reiner, S.; Hinrichsen, O. *Appl. Catal., A* **2013**, *450*, 1.

(50)   Jiang, P.; Prendergast, D.; Borondics, F.; Porsgaard, S.; Giovanetti, L.; Pach, E.; Newberg, J.; Bluhm, H.; Besenbacher, F.; Salmeron, M. *J. Chem. Phys.* **2013**, *138*.

(51)   Jensen, F.; Besenbacher, F.; Laegsgaard, E.; Stensgaard, I. *Surf. Sci.* **1991**, *259*, L774.

(52)   Matsumoto, T.; Bennett, R. A.; Stone, P.; Yamada, T.; Domen, K.; Bowker, M. *Surf. Sci.* **2001**, *471*, 225.

(53)   An, W.; Baber, A. E.; Xu, F.; Soldemo, M.; Weissenrieder, J.; Stacchiola, D.; Liu, P. *ChemCatChem* **2014**, *6*, 2364.

(54)   Yang, F.; Choi, Y. M.; Liu, P.; Hrbek, J.; Rodriguez, J. A. *J. Phys. Chem. C* **2010**, *114*, 17042.

(55)   An, W.; Xu, F.; Stacchiola, D.; Liu, P. *ChemCatChem* **2015**, *7*, 3865.

(56)   Yang, F.; Choi, Y.; Liu, P.; Stacchiola, D.; Hrbek, J.; Rodriguez, J. A. *J. Am. Chem. Soc.* **2011**, *133*, 11474.

(57)   Breddy, N. C.; Smith, H. J. *Vacuum* **1963**, *13*, 449.

(58)   Binnig, G.; Rohrer, H. *Helvetica Physica Acta* **1982**, *55*, 726.

(59)   Mudiyanselage, K.; Xu, F.; Hoffmann, F. M.; Hrbek, J.; Waluyo, I.; Boscoboinik, J. A.; Stacchiola, D. *J. Phys. Chem. Chem. Phys.* **2015**, *17*, 3032.

(60)   Baber, A. E.; Xu, F.; Dvorak, F.; Mudiyanselage, K.; Soldemo, M.; Weissenrieder, J.; Senanayake, S. D.; Sadowski, J. T.; Rodriguez, J. A.; Matolin, V.; White, M. G.; Stacchiola, D. J. *J. Am. Chem. Soc.* **2013**, *135*, 16781.

(61)   Schuurmans, N.; Uji-i, H.; Mamdouh, W.; De Schryver, F. C.; Feringa, B. L.; van Esch, J.; De Feyter, S. *J. Am. Chem. Soc.* **2004**, *126*, 13884.

(62)   Lu, Y. H.; Quardokus, R.; Lent, C. S.; Justaud, F.; Lapinte, C.; Kandel, S. A. *J. Am. Chem. Soc.* **2010**, *132*, 13519.

(63)   Gong, J. R.; Yan, H. J.; Yuan, Q. H.; Xu, L. P.; Bo, Z. S.; Wan, L. J. *J. Am. Chem. Soc.* **2006**, *128*, 12384.

(64)   Shapir, E.; Yi, J. Y.; Cohen, H.; Kotlyar, A. B.; Cuniberti, G.; Porath, D. *J. Phys. Chem. B* **2005**, *109*, 14270.

(65)   Binnig, G.; Rohrer, H. *Surf. Sci.* **1983**, *126*, 236.

(66)   Zandvliet, H. J. W.; van Houselt, A. In *Annual Review of Analytical Chemistry*; Annual Reviews: Palo Alto, 2009; Vol. 2, p 37.

(67)   Hollande.Jm; Jolly, W. L. *Acc. Chem. Res.* **1970**, *3*, 193.

(68)   Seah, M. P.; Dench, W. A. *Surf. Interface Anal.* **1979**, *1*, 2.

(69)   Pradier, C.-M.; Chabal, Y. J. *Biointerface characterization by advanced IR spectroscopy*; Elsevier, 2011.

(70)   Strauman.Me; Yu, L. S. *Acta Crystallographica Section a-Crystal Physics Diffraction Theoretical and General Crystallography* **1969**, *A 25*, 676.

(71)   Fu, T. Y.; Tzeng, Y. R.; Tsong, T. T. *Surf. Sci.* **1996**, *366*, L691.

(72)   Marinica, M. C.; Barreteau, C.; Desjonqueres, M. C.; Spanjaard, D. *Physical Review B* **2004**, *70*, 14.

(73)   Repp, J.; Meyer, G.; Rieder, K. H.; Hyldgaard, P. *Phys. Rev. Lett.* **2003**, *91*, 4.

(74)   Chinchen, G. C.; Spencer, M. S.; Waugh, K. C.; Whan, D. A. *Journal of the Chemical Society-Faraday Transactions I* **1987**, *83*, 2193.

(75)   Denise, B.; Sneeden, R. P. A. *Applied Catalysis* **1986**, *28*, 235.

(76)   Wiame, F.; Maurice, V.; Marcus, P. *Surf. Sci.* **2007**, *601*, 1193.

(77)   Bartels, L.; Meyer, G.; Rieder, K. H. *Surf. Sci.* **1999**, *432*, L621.

(78)   Anger, G.; Winkler, A.; Rendulic, K. D. *Surf. Sci.* **1989**, *220*, 1.

(79)   Panczyk, T. *Phys. Chem. Chem. Phys.* **2006**, *8*, 3782.

(80)   Hrbek, J.; Hoffmann, F. M.; Park, J. B.; Liu, P.; Stacchiola, D.; Hoo, Y. S.; Ma, S.; Nambu, A.; Rodriguez, J. A.; White, M. G. *J. Am. Chem. Soc.* **2008**, *130*, 17272.

(81)   Mudiyanselage, K.; An, W.; Yang, F.; Liu, P.; Stacchiola, D. J. *Phys. Chem. Chem. Phys.* **2013**, *15*, 10726.

(82)   Wadayama, T.; Kubo, K.; Yamashita, T.; Tanabe, T.; Hatta, A. *J. Phys. Chem. B* **2003**, *107*, 3768.

(83)   Mudiyanselage, K.; Senanayake, S. D.; Ramirez, P. J.; Kundu, S.; Baber, A.; Yang, F.; Agnoli, S.; Axnanda, S.; Liu, Z.; Hrbek, J.; Evans, J.; Rodriguez, J. A.; Stacchiola, D. *Top. Catal.* **2015**, *58*, 271.

(84)   Piccolo, L.; Loffreda, D.; Aires, F.; Deranlot, C.; Jugnet, Y.; Sautet, P.; Bertolini, J. C. *Surf. Sci.* **2004**, *566*, 995.

(85)   Raval, R.; Parker, S. F.; Pemble, M. E.; Hollins, P.; Pritchard, J.; Chesters, M. A. *Surf. Sci.* **1988**, *203*, 353.

(86)   Tiwari, R. K.; Otalvaro, D. M.; Joachim, C.; Saeys, M. *Surf. Sci.* **2009**, *603*, 3286.

(87)   Mesters, C.; Wermer, G.; Gijzeman, O. L. J.; Geus, J. W. *Surf. Sci.* **1983**, *135*, 396.

(88)   Lee, H. J.; Ho, W. *Physical Review B* **2000**, *61*, R16347.

(89)   Rose, M. K.; Mitsui, T.; Dunphy, J.; Borg, A.; Ogletree, D. F.; Salmeron, M.; Sautet, P. *Surf. Sci.* **2002**, *512*, 48.

(90)   Drakova, D.; Nedjalkova, M.; Doyen, G. *Int. J. Quantum Chem* **2006**, *106*, 1419.

(91)   Thamankar, R.; Meyerheim, H. L.; Ernst, A.; Ostanin, S.; Maznichenko, I. V.; Soyka, E.; Mertig, I.; Kirschner, J. *Phys. Rev. Lett.* **2011**, *106*.

(92)   Habraken, F.; Kieffer, E. P.; Bootsma, G. A. *Surf. Sci.* **1979**, *83*, 45.

(93)   Michely, T.; Comsa, G. *Surf. Sci.* **1991**, *256*, 217.

(94)   Michely, T.; Besocke, K. H.; Comsa, G. *Surf. Sci.* **1990**, *230*, L135.

(95)   Morgenstern, K.; Rosenfeld, G.; Poelsema, B.; Comsa, G. *Phys. Rev. Lett.* **1995**, *74*, 2058.

(96)   Morgenstern, K.; Rosenfeld, G.; Laegsgaard, E.; Besenbacher, F.; Comsa, G. *Phys. Rev. Lett.* **1998**, *80*, 556.

(97)   Paszti, Z.; Hakkel, O.; Keszthelyi, T.; Berko, A.; Balazs, N.; Bako, I.; Guczi, L. *Langmuir* **2010**, *26*, 16312.

(98)   Kammler, T.; Kuppers, J. *J. Chem. Phys.* **1999**, *111*, 8115.

(99)   Hammer, B.; Scheffler, M.; Jacobsen, K. W.; Norskov, J. K. *Phys. Rev. Lett.* **1994**, *73*, 1400.

(100)   Abbott, H. L.; Harrison, I. *J. Phys. Chem. A* **2007**, *111*, 9871.

(101)   Wang, X.; Fei, Y. Y.; Zhu, X. D. *Chem. Phys. Lett.* **2009**, *481*, 58.

(102)   Jewell, A. D.; Peng, G. W.; Mattera, M. F. G.; Lewis, E. A.; Murphy, C. J.; Kyriakou, G.; Mavrikakis, M.; Sykes, E. C. H. *ACS Nano* **2012**, *6*, 10115.

(103)   Hellman, A.; Svensson, K.; Andersson, S. *J. Phys. Chem. C* **2014**, *118*, 15773.

(104)   Lin, S. D.; Hsiao, T. C.; Chen, L. C. *Appl. Catal. A-Gen.* **2009**, *360*, 226.

(105)   Chaudhari, R. V.; Jaganathan, R.; Kolhe, D. S.; Emig, G.; Hofmann, H. *Industrial & Engineering Chemistry Product Research and Development* **1986**, *25*, 375.

(106)   Ueda, A.; Haruta, M. *Gold Bulletin* **1999**, *32*, 3.

(107)   Szanyi, J.; Goodman, D. W. *Catal. Lett.* **1993**, *21*, 165.

(108)   Klier, K. *Advances in Catalysis* **1982**, *31*, 243.

(109)   Newsome, D. S. *Catalysis Reviews-Science and Engineering* **1980**, *21*, 275.

(110)   Togari, O.; Matsuda, M.; Shimokawa, K.; Makabe, T.; Office, U. S. P. a. T., Ed. 1984.

(111)   Peppley, B. A.; Amphlett, J. C.; Kearns, L. M.; Mann, R. F. *Appl. Catal. A-Gen.* **1999**, *179*, 21.

(112)   Rodriguez, J. A.; Liu, P.; Hrbek, J.; Evans, J.; Perez, M. *Angew. Chem. Int. Ed.* **2007**, *46*, 1329.

(113)   Bion, N.; Epron, F.; Moreno, M.; Marino, F.; Duprez, D. *Top. Catal.* **2008**, *51*, 76.

(114)   Mars, P.; van Krevelen, D. W. *Special Supplement to Chemical Engineering Science* **1954**, *3*, 41.

(115)   Lundgren, E.; Gustafson, J.; Resta, A.; Weissenrieder, J.; Mikkelsen, A.; Andersen, J. N.; Kohler, L.; Kresse, G.; Klikovits, J.; Biederman, A.; Schmid, M.; Varga, P. *J. Electron. Spectrosc. Relat. Phenom.* **2005**, *144*, 367.

(116)   Maimaiti, Y.; Nolan, M.; Elliott, S. D. *Phys. Chem. Chem. Phys.* **2014**, *16*, 3036.

(117)   Dow, W. P.; Wang, Y. P.; Huang, T. J. *J. Catal.* **1996**, *160*, 155.

(118)   Hamada, S.; Kudo, Y.; Tojo, T. *Colloids and Surfaces* **1992**, *67*, 45.

(119)   Poulston, S.; Parlett, P. M.; Stone, P.; Bowker, M. *Surf. Interface Anal.* **1996**, *24*, 811.

(120)   Rodriguez, J. A.; Hanson, J. C.; Frenkel, A. I.; Kim, J. Y.; Perez, M. *J. Am. Chem. Soc.* **2002**, *124*, 346.

(121)   Zhang, R. G.; Wang, B. J.; Ling, L. X.; Liu, H. Y.; Huang, W. *Appl. Surf. Sci.* **2010**, *257*, 1175.

(122)   Wei, Y. Y.; Martinez, U.; Lammich, L.; Besenbacher, F.; Wendt, S. *Surf. Sci.* **2014**, *619*, L1.

(123)   Klikovits, J.; Schmid, M.; Gustafson, J.; Mikkelsen, A.; Resta, A.; Lundgren, E.; Andersen, J. N.; Varga, P. *J. Phys. Chem. B* **2006**, *110*, 9966.

(124)   Dang, J.; Chou, K. C.; Hu, X. J.; Zhang, G. H. *Steel Res. Int.* **2013**, *84*, 526.

(125)   Schulz, K. H.; Cox, D. F. *Surf. Sci.* **1992**, *278*, 9.

(126)   Knudsen, J.; Merte, L. R.; Grabow, L. C.; Eichhorn, F. M.; Porsgaard, S.; Zeuthen, H.; Vang, R. T.; Laegsgaard, E.; Mavrikakis, M.; Besenbacher, F. *Surf. Sci.* **2010**, *604*, 11.

(127)   Mudiyanselage, K.; An, W.; Yang, F.; Liu, P.; Stacchiola, D. *J. Phys. Chem. Chem. Phys.* **2013**, doi: 10.1039/C3CP50522G.

(128)   Mudiyanselage, K.; Kim, H. Y.; Senanayake, S. D.; Baber, A. E.; Liu, P.; Stacchiola, D. *Phys. Chem. Chem. Phys.* **2013**, *15*, 15856.

(129)   Lu, J. L.; Kaya, S.; Weissenrieder, J.; Gao, H. J.; Shaikhutdinov, S.; Freund, H. J. *Surf. Sci.* **2006**, *600*, L153.

(130)   Yang, F.; Chen, M. S.; Goodman, D. W. *The Journal of Physical Chemistry C* **2008**, *113*, 254.

(131)   Starr, D. E.; Shaikhutdinov, S. K.; Freund, H. J. *Top. Catal.* **2005**, *36*, 33.

(132)   Cox, D. F.; Schulz, K. H. *Surf. Sci.* **1991**, *256*, 67.

(133)   Kirsch, P. D.; Ekerdt, J. G. *J. Appl. Phys.* **2001**, *90*, 4256.

(134)   Kumagai, T.; Kaizu, M.; Okuyama, H.; Hatta, S.; Aruga, T.; Hamada, I.; Morikawa, Y. *Physical Review B* **2009**, *79*.

(135)   Guillemot, L.; Bobrov, K. *J. Phys. Chem. C* **2011**, *115*, 22387.

(136)   Morrill, M. R.; Thao, N. T.; Agrawal, P. K.; Jones, C. W.; Davis, R. J.; Shou, H.; Barton, D. G.; Ferrari, D. *Catal. Lett.* **2012**, *142*, 875.

(137)   Clarke, D. B.; Bell, A. T. *J. Catal.* **1995**, *154*, 314.

(138)   Huo, C.-F.; Wu, B.-S.; Gao, P.; Yang, Y.; Li, Y.-W.; Jiao, H. *Angew. Chem. Int. Ed.* **2011**, *50*, 7403.

(139)   Shao, X.; Cui, Y.; Schneider, W. D.; Nilius, N.; Freund, H. J. *J. Phys. Chem. C* **2012**, *116*, 17980.

(140)   Mariotto, G.; Murphy, S.; Berdunov, N.; Ceballos, S. F.; Shvets, I. V. *Surf. Sci.* **2004**, *564*, 79.

(141)   Politano, A.; Formoso, V.; Agostino, R. G.; Colavita, E.; Chiarello, G. *J. Chem. Phys.* **2008**, *128*, 5.

(142)   Politano, A.; Formoso, V.; Chiarello, G. *J. Chem. Phys.* **2008**, *129*, 5.

(143)   Kiss, A. M.; Svec, M.; Berko, A. *Surf. Sci.* **2006**, *600*, 3352.

(144)   von Hofe, T.; Kröger, J.; Berndt, R. *Physical Review B* **2006**, *73*, 245434.

(145)   Fan, W. C.; Ignatiev, A. *Physical Review B* **1988**, *37*, 5274.

(146)   Kim, J.; Khajetoorians, A. A.; Zhu, W.; Zhang, Z.; Shih, C.-K. *Surf. Sci.* **2012**, *606*, 450.

(147)   Yurtsever, A.; Sugimoto, Y.; Abe, M.; Matsunaga, K.; Tanaka, I.; Morita, S. *Physical Review B* **2011**, *84*, 7.

(148)   Shaikhutdinov, S. K.; Weiss, W.; Schlogl, R. *Appl. Surf. Sci.* **2000**, *161*, 497.

(149)   Zhao, W.; Kerner, G.; Asscher, M.; Wilde, X. M.; Al-Shamery, K.; Freund, H. J.; Staemmler, V.; Wieszbowska, M. *Physical Review B* **2000**, *62*, 7527.

(150)   Jerratsch, J. F.; Nilius, N.; Freund, H. J.; Martinez, U.; Giordano, L.; Pacchioni, G. *Physical Review B* **2009**, *80*, 8.

(151)   Yang, F.; Graciani, J.; Evans, J.; Liu, P.; Hrbek, J.; Sanz, J. F.; Rodriguez, J. A. *J. Am. Chem. Soc.* **2011**, *133*, 3444.

(152)   Marino, F.; Descorme, C.; Duprez, D. *Appl. Catal., B* **2005**, *58*, 175.

(153)   Barrio, L.; Estrella, M.; Zhou, G.; Wen, W.; Hanson, J. C.; Hungria, A. B.; Hornes, A.; Fernandez-Garcia, M.; Martinez-Arias, A.; Rodriguez, J. A. *J. Phys. Chem. C* **2010**, *114*, 3580.

(154)   Mullins, D. R.; Albrecht, P. M.; Chen, T.-L.; Calaza, F. C.; Biegalski, M. D.; Christen, H. M.; Overbury, S. H. *The Journal of Physical Chemistry C* **2012**, *116*, 19419.

(155)   Dvořák, F.; Stetsovych, O.; Steger, M.; Cherradi, E.; Matolínová, I.; Tsud, N.; Škoda, M.; Skála, T.; Mysliveček, J.; Matolín, V. *The Journal of Physical Chemistry C* **2011**, *115*, 7496.

(156)   Yang, F.; Choi, Y.; Agnoli, S.; Liu, P.; Stacchiola, D.; Hrbek, J.; Rodriguez, J. A. *The Journal of Physical Chemistry C* **2011**, *115*, 23062.

(157)   Tatsumi, H.; Sasahara, A.; Tomitori, M. *J. Phys. Chem. C* **2012**, *116*, 13688.

(158)   Yang, B.; Xu, H.; Lu, J.; Loh, K. P. *J. Am. Chem. Soc.* **2014**, *136*, 12041.

(159)   Rendek, L. J.; Chottiner, G. S.; Scherson, D. A. *Langmuir* **2001**, *17*, 849.

(160)   Ertl, G.; Lee, S. B.; Weiss, M. *Surf. Sci.* **1981**, *111*, L711.

(161)   Solymosi, F.; Kovács, I. *Surf. Sci.* **1992**, *260*, 139.

(162) Gravelle-Rumeau-Maillot, M.; Pitchon, V.; Martin, G. A.; Praliaud, H. *Applied Catalysis A: General* **1993**, *98*, 45.

(163) Uner, D. O.; Pruski, M.; Gerstein, B. C.; King, T. S. *J. Catal.* **1994**, *146*, 530.

(164) Zhang, C.; Zhao, G.; Liu, K.; Yang, Y.; Xiang, H.; Li, Y. *J. Mol. Catal. A: Chem.* **2010**, *328*, 35.

(165) Brown, J. K.; Luntz, A. C.; Schultz, P. A. *The Journal of Chemical Physics* **1991**, *95*, 3767.

(166) Resch, C.; Zhukov, V.; Lugstein, A.; Berger, H. F.; Winkler, A.; Rendulic, K. D. *Chem. Phys.* **1993**, *177*, 421.

(167) Yu, X.; Raaen, S. *Appl. Surf. Sci.* **2013**, *270*, 364.

(168) Huang, H. H.; Jiang, X.; Zou, Z.; Xu, G. Q. *Surf. Sci.* **1997**, *376*, 245.

(169) Wilke, S.; Cohen, M. H. *Surf. Sci.* **1997**, *380*, L446.

(170) Onsgaard, J.; Godowski, P. J.; Nerlov, J.; Quist, S.; Hoffmann, S. V. *Surf. Sci.* **1998**, *398*, 318.

(171) Royer, S.; Duprez, D. *Chemcatchem* **2011**, *3*, 24.

(172) Prasad, R.; Singh, P. *Cat. Rev. - Sci. Eng.* **2012**, *54*, 224.

(173) Oh, S. H.; Sinkevitch, R. M. *J. Catal.* **1993**, *142*, 254.

(174) Marino, F.; Descorme, C.; Duprez, D. *Appl. Catal., B* **2004**, *54*, 59.

(175) Saalfrank, J. W.; Maier, W. F. *Angew. Chem. Int. Ed.* **2004**, *43*, 2028.

(176) Xie, X. W.; Li, Y.; Liu, Z. Q.; Haruta, M.; Shen, W. J. *Nature* **2009**, *458*, 746.

(177) Crew, W. W.; Madix, R. J. *Surf. Sci.* **1996**, *349*, 275.

(178) Ono, Y.; Shibata, M.; Inui, T. *J. Mol. Catal. A: Chem.* **2000**, *153*, 53.

(179) Liu, X. Y.; Wang, A. Q.; Zhang, T.; Su, D. S.; Mou, C. Y. *Catal. Today* **2011**, *160*, 103.

(180) Mrabet, D.; Abassi, A.; Cherizol, R.; Do, T. O. *Appl. Catal., A* **2012**, *447*, 60.

(181) Domagala, M. E.; Campbell, C. T. *Catal. Lett.* **1991**, *9*, 65.

(182) Jernigan, G. G.; Somorjai, G. A. *J. Catal.* **1994**, *147*, 567.

(183) Gao, F.; Goodman, D. W. *Langmuir* **2010**, *26*, 16540.

(184) Wei, Z. Z.; Li, D. C.; Pang, X. Y.; Lv, C. Q.; Wang, G. C. *Chemcatchem* **2012**, *4*, 100.

(185) Le, D.; Stolbov, S.; Rahman, T. S. *Surf. Sci.* **2009**, *603*, 1637.

(186) Sadykov, V. A.; Tikhov, S. F.; Bulgakov, N. N.; Gerasev, A. P. *Catal. Today* **2009**, *144*, 324.

(187) Sun, B. Z.; Chen, W. K.; Xu, Y. J. *J. Chem. Phys.* **2010**, *133*.

(188) Crew, W. W.; Madix, R. J. *Surf. Sci.* **1996**, *356*, 1.

(189) Hartmann, N.; Madix, R. J. *Surf. Sci.* **2002**, *516*, 230.

(190) Wintterlin, J.; Volkening, S.; Janssens, T. V. W.; Zambelli, T.; Ertl, G. *Science* **1997**, *278*, 1931.

(191) Denecke, R.; Vaterlein, P.; Bassler, M.; Wassdahl, N.; Butorin, S.; Nilsson, A.; Rubensson, J. E.; Nordgren, J.; Martensson, N.; Nyholm, R. *J. Electron. Spectrosc. Relat. Phenom.* **1999**, *101*, 971.

(192) Borguet, E.; Dai, H. L. *J. Phys. Chem. B* **2005**, *109*, 8509.

(193) Hollins, P.; Pritchard, J. *Surf. Sci.* **1979**, *89*, 486.

(194) Pritchard, J.; Catterick, T.; Gupta, R. K. *Surf. Sci.* **1975**, *53*, 1.

(195) Xu, X. P.; Vesecky, S. M.; He, J. W.; Goodman, D. W. *J. Vac. Sci. Technol., A* **1993**, *11*, 1930.

(196)   Hollins, P.; Pritchard, J. *Surf. Sci.* **1983**, *134*, 91.

(197)   Mudiyanselage, K.; Kim, H. Y.; Senanayake, S. D.; Baber, A. E.; Liu, P.; Stacchiola, D. *Phys. Chem. Chem. Phys.* **2013**, *15*, 15856.

(198)   Baber, A. E.; Yang, X. F.; Kim, H. Y.; Mudiyanselage, K.; Soldemo, M.; Weissenrieder, J.; Senanayake, S. D.; Al-Mahboob, A.; Sadowski, J. T.; Evans, J.; Rodriguez, J. A.; Liu, P.; Hoffmann, F. M.; Chen, J. G. G.; Stacchiola, D. J. *Angew. Chem. Int. Ed.* **2014**, *53*, 5336.

(199)   Peden, C. H. F.; Goodman, D. W.; Weisel, M. D.; Hoffmann, F. M. *Surf. Sci.* **1991**, *253*, 44.

(200)   Garner, W. E.; Stone, F. S.; Tiley, P. F. *Proc. R. Soc. London, Ser. A* **1952**, *211*, 472.

(201)   Qadir, K.; Kim, S. M.; Seo, H.; Mun, B. S.; Akgul, F. A.; Liu, Z.; Park, J. Y. *J. Phys. Chem. C* **2013**, *117*, 13108.

(202)   Bluhm, H.; Havecker, M.; Knop-Gericke, A.; Kleimenov, E.; Schlogl, R.; Teschner, D.; Bukhtiyarov, V. I.; Ogletree, D. F.; Salmeron, M. *J. Phys. Chem. B* **2004**, *108*, 14340.

(203)   Lawton, T. J.; Pushkarev, V.; Broitman, E.; Reinicker, A.; Sykes, E. C. H.; Gellman, A. J. *J. Phys. Chem. C* **2012**, *116*, 16054.

(204)   Lawton, T.; Kyriakou, G.; Baber, A.; Sykes, E. *Chemcatchem* **2013**, *5*, 2684.

(205)   Niehus, H. *Surf. Sci.* **1983**, *130*, 41.

(206)   Lahtonen, K.; Hirsimaki, M.; Lampimaki, M.; Valden, M. *J. Chem. Phys.* **2008**, *129*, 124703.

(207)   Imbihl, R.; Ertl, G. *Chem. Rev.* **1995**, *95*, 697.

(208)   Krischer, K.; Eiswirth, M.; Ertl, G. *J. Chem. Phys.* **1992**, *96*, 9161.

(209)   Kandoi, S.; Gokhale, A. A.; Grabow, L. C.; Dumesic, J. A.; Mavrikakis, M. *Catal Lett* **2004**, *93*, 93.

(210)   Vankooten, W. E. J.; Vannispen, J. P. C.; Gijzeman, O. L. J.; Geus, J. W. *Surf. Sci.* **1994**, *315*, 219.